FAST CARBON-ION AND PROTON INDUCED ELECTRON EMISSION FROM CONDENSED-PHASE BIOLOGICAL TARGETS

by

Eric Maertz

July 2018

Director of Dissertation: Dr. Jefferson L. Shinpaugh

Major Department: Physics

Fast charged particles interact with matter through various ionization and excitation pathways that aren't fully understood. Predicting the effects of these interactions is vital in many fields such as radiation therapy, space exploration, and materials processing. Monte Carlo models of the spatial distribution of dose deposited in tissue require cross section data of the incident charged particles and the secondary electrons they produce in biological media. Because the interaction cross sections cannot be directly measured in condensed-phase materials, precise measurements of electron emission from solids can test and improve track-structure simulations of charged-particle transport in solids. In this thesis, doubly differential electron emission yields $\gamma(\varepsilon, \theta)$, as a function of electron energy ε and emission angle θ, were measured for proton and carbon-ion beams in the energy range of 0.2-4.0 MeV/u with gold and amorphous solid water targets. Energy analysis was conducted using the electron time of flight, thus focusing on low-energy electrons that dominate the emission spectrum. The experimental data are presented for various projectile and target combinations, and are compared to results from the track-structure simulations.

FAST CARBON-ION AND PROTON INDUCED ELECTRON EMISSION FROM CONDENSED-PHASE BIOLOGICAL TARGETS

A Dissertation

Presented to the Faculty of the Department of Physics

East Carolina University

In Partial Fulfillment of the Requirements for the Degree

Doctor of Philosophy in Biomedical Physics

by

Eric Maertz

July 2018

FAST CARBON-ION AND PROTON INDUCED ELECTRON EMISSION FROM CONDENSED-PHASE BIOLOGICAL TARGETS

by

Eric Maertz

APPROVED BY:

DIRECTOR OF
DISSERTATION: _____
Jefferson Shinpaugh, PhD

COMMITTEE MEMBER: _____
Michael Dingfelder, PhD

COMMITTEE MEMBER: _____
Zi-Wei Lin, PhD

COMMITTEE MEMBER: _____
Robert A. McLawhorn, PhD

COMMITTEE MEMBER: _____
Zhibin Huang, PhD

CHAIR OF THE
DEPARTMENT OF PHYSICS: _____
Jefferson Shinpaugh, PhD

DEAN OF THE
GRADUATE SCHOOL: _____
Paul J. Gemperline, PhD

ACKNOWLEDGEMENTS

I would like to thank my advisor, Dr. Jefferson Shinpaugh, who can always be counted on for the best advice. His expertise and wisdom were invaluable in navigating the challenges, complications, and frustrations that could arise on any given day working in the lab. The guidance he has given me over the years has always steered me back on course, not just in the lab but also in everyday life. I cannot understate his contribution to my research and the knowledge and insight I've gained while working toward my degree. He is a brilliant, genuine, and considerate person, and I will always look forward to grabbing a beer with him and catching up on life.

Next, I would like to thank the very knowledgeable and expert staff at ECU: Chris Bonnerup, Gene Oakley, and William Holland. These men were available at a moment's notice to fix faulty equipment, troubleshoot and brainstorm ideas, or create (then modify and upgrade) any components I could possibly need. They always came through, and I've been lucky to get to know them over the years.

Saving the best for last, I want to thank my beautiful, loving, and talented fiancé Katie. Through the ups and downs, she has always been there for me with a warm smile and supportive words. I couldn't have finished this work without her in my life. I'm so excited and happy that she will be by my side as we start the next chapter of our lives. I can only hope to be as wonderful a partner and companion to her as she is to me.

TABLE OF CONTENTS

LIST OF TABLES

LIST OF FIGURES

LIST OF ABBREVIATIONS

ASW	amorphous solid water
BE	binary encounter
CEM	channel electron multiplier
CSDA	continuously slowing down approximation
DI	de-ionized
ECU	East Carolina University
GSI	Gesellschaft für Schwerionenforschung
HIMAC	Heavy Ion Medical Accelerator in Chiba
HV	high voltage
LBNL	Lawrence Berkeley National Laboratory
LET	linear energy transfer
MC	Monte Carlo
MCPs	microchannel plates
ML	monolayer
MOSFETs	metal-oxide-semiconductor field-effect transistors
NEC	National Electrostatics Corporation®
NFE	nearly free electron
NI	National Instruments®
NIM	Nuclear Instrument Module
OER	oxygen enhancement ratio
PHA	pulse-height analysis
RBE	relative biological effectiveness
RGA	residual gas analyzer
RMS	root mean squared
SOBP	spread-out Bragg peak
SRIM	Stopping and Range of Ions in Matter
TOF	time of flight
UHV	ultra-high vacuum

Chapter 1: Introduction

Characterizing damage in materials from charged-particle radiation has a wide range of applications including processing of industrial materials and microelectronic devices, shielding from cosmic rays, and radiation therapy (radiotherapy) in the treatment of cancer and other malignancies. Particularly, the medical physics field relies on accurate modeling of the spatial distribution of dose administered during radiotherapy. It is well known that a significant amount of biological damage to tissue occurs not only from the primary ionizing radiation, either photons or ions, but also from the secondary electrons that subsequently traverse the tissue and cause additional ionizations. Monte Carlo (MC) track-structure simulations are the most precise computational technique to model the production and transport of secondary electrons, and thus spatial dose distribution, but lack accurate experimental data for input. This is especially true for increasingly prominent radiation therapies employing protons, carbon ions, and metallic nanoparticles.

Experiments have been developed in the East Carolina University Accelerator Laboratory in the Department of Physics to provide direct tests of the MC electron transport models of energy deposition (leading to damage) from charged-particle radiation in biological systems. In our experiments, proton and C-ion beams from the 2 MV Pelletron particle accelerator were used to irradiate condensed-phase targets of Au and amorphous solid water (ASW). A new beam-pulsing system was developed to produce nanosecond ion-beam pulses to enable time-of-flight (TOF) energy analysis of the secondary electrons emitted from the targets. Doubly differential electron emission yields $\gamma(\varepsilon, \theta)$, as a function of electron energy ε and emission angle θ relative to the projectile's velocity, were measured for several proton and C-ion projectile energies in the

range 0.2-4.0 MeV/u (u is an atomic mass unit, sometimes expressed as amu). The experimental data were directly compared to results from MC electron transport simulations, generated by faculty in the Department of Physics at East Carolina University.

The interactions of ionizing radiation with atoms and molecules of a gas or solid medium are complex in nature. Fast charged particles in a material produce secondary electrons and a variety of atomic or molecular ions, as well as other excited states. The probability and rate for the variety of ionization processes depend on the type and energy of the ionizing radiation. Because different pathways of ionization lead to different yields of bioactive species (and ultimately varying degrees of biological damage), detailed information regarding the production of these species is required to predict the biological outcome of radiation exposure. This information would allow for more accurate computational modelling of the spatial distribution of dose caused by ionizations and excitations produced by charged particles as they lose energy in tissue. Many studies have been conducted to gather this information, in the form of interaction cross sections, from various gaseous targets impacted by protons [2, 44, 87, 93-95] or other heavy-ion projectiles [2, 95]. However, gas-phase data requires assumptions and extrapolations when applied to condensed-phase materials, where cross sections cannot be directly measured.

With charged-particle interaction cross section data, more accurate descriptions of biological damage could be predicted, particularly for cellular and subcellular target volumes [35, 104]. Particularly, single- and double-strand breaks in DNA molecules are responsible for a significant amount of cellular damage, and the manner in which charged particles can produce clustered damage is not fully understood [36, 105, 106]. MC track-structure models can follow the incident charged particles and predict each energy-transferring interaction they might have with target atoms or molecules as they slow to sub-excitation velocities. Likewise, the secondary

electrons' paths of energy deposition can be modelled, and a complete description of dose deposition can be formed. These models have been generated and altered over the years for simulated water targets, to mimic the cellular environment which is ~80% water, for electrons [17, 19, 55, 57, 66, 68, 69, 73, 74, 76, 97-99] and atomic ions [1, 12, 13, 37, 52, 56, 85, 91, 109]. More recently, they have extended the complexity of the simulated target material to mimic subcellular components such as DNA [1, 14, 30-33, 67-69, 91, 103, 109].

Generalizations of the complex charged-particle interactions are often used to describe the rate of energy loss, i.e. linear energy transfer (LET) or stopping power, by a charged particle in a condensed-phase material. They do not provide information on the energy and angular components of the secondary electrons that continue to cause ionizations and deposit energy away from the primary charged particles' tracks. However, since secondary electrons will undergo multiple interactions with the atoms or molecules of a condensed-phase material, the cross sections cannot be directly measured (as with gasses) and the input used for MC models may not reflect the actual production of secondary electrons. To advance the theoretical description of charged-particle dose deposition in tissue, beyond the conventional LET or stopping power models, MC track-structure codes mimicking experimental configurations and geometries need to be tested and validated by comparison to measured doubly differential secondary electron yields.

Specifically, experiments were designed to compare measurements of the energies and emission angles of secondary electrons from both (forward and backward) sides of thin solid targets to simulated emission yields. The secondary electrons were produced by nanosecond pulses of fast proton and C-ion impact. The emitted electrons were temporally measured with microchannel plates and correlated to the time of projectile impact to determine electron time of

flight, and thus energy. This TOF energy analysis method is ideal for accurate measurement of low-energy electrons, which were the focus of these experiments. The TOF detector was positioned at emission angles varying from 10-160° to study the angular dependence of secondary electron emission from condensed-phase targets. The secondary electron yields were measured relative to scattered projectile counts, and normalized to absolute yields recorded in the literature [8, 51]. They provide accurate tests for the low-energy portion of the electron emission spectra, where MC simulations are most severely lacking in ionization cross section data. This energy region is the least understood, as assumptions and estimates of charged-particle interactions are generally formulated for projectiles and secondary electrons that exceed the velocities of valence electrons in the target.

This dissertation is composed of four more chapters, each providing the background knowledge and information that may be needed for the subsequent chapter. Chapter 2 has several purposes and covers many informative topics. First, general background information on the physics of ionizing radiation is presented in the context of a biological environment where chemistry plays the role of an intermediary. Then, an overview of the current status of ion therapy and its clinical application is given. Next, some theoretical descriptions of charged-particle interactions and ionizing events are explained. This is followed by details of the particular circumstance where secondary electrons are produced, transported, and emitted from condensed-phase materials. Finally, the specifics involved with doubly differential electron emission yields from ASW and Au are elucidated.

Chapter 3 is dedicated to the detailed description of the materials involved and the methods employed for this research project. This entails an explanation of the various equipment involved in the production and acceleration of tightly focused and collimated atomic

ion beams. Then, the specific application of beam pulsing for ~2-5 ns timing will be explained. This is followed by a detailed description of the ultra-high vacuum target chamber and all of its ancillary components needed for maintaining clean metal surfaces, depositing thin films of ultra-pure amorphous solid water at temperatures <50 K, and simultaneously measuring low-energy electrons and scattered projectiles in a field-free region. A step-by-step explanation of the acquisition, handling, and processing of data follows, along with specifics of target preparation.

Chapter 4 is devoted to the presentation of experimental results and a discussion of the energy and angular electron emission dependencies that are revealed by the doubly differential electron spectra. First, results from system tests of target purity, electronics calibration, and data reproducibility are shown. Then, electron emission spectra from proton impact on Au and ASW are presented, along with comparisons to previous results and MC simulations. This section also analyzes singly differential and total electron yields from proton impact, and compares these to relevant published results. Next, the electron emission spectra from C-ion impact on Au and ASW are given. Comparisons between electron emission induced by doubly and triply charged states of C are made.

Lastly, chapter 5 summarizes the results and overall conclusions of this research. Critique is given for the strengths and weaknesses of the experimental process. Suggestions for improvements and the future direction of this particular field of study are made.

Chapter 2: Charged-Particle Interactions with Solids

2.1: Introduction

The main goal of the work to be presented in the following chapters is the measurement of doubly differential electron emission yields $\gamma(\varepsilon, \theta)$, as a function of electron energy ε and emission angle θ relative to the projectile's velocity, for the comparison to and improvement of Monte Carlo track-structure simulations. These measurements focused on charged-particle interactions with Au and amorphous solid water, often used in computational modelling as a substitute for tissue which is composed of ~80% water by mass. Significant differences exist in the nature of charged-particle interactions with matter as compared to electromagnetic radiation. How these differences can be exploited to improve radiation therapy is an area of great interest. A large amount of recent literature dealing with this topic is available [49, 53, 64, 83, 86, 103, 111]. There are complex connections between the physical, chemical, and biological processes that dictate how ionizing radiation produces a biological effect. Therefore, the incorporation of DNA damage into MC models is also of great interest [1, 30-33, 69, 91, 103].

Probing the structure of atoms in gaseous or condensed phases by subjecting materials to ionizing radiation is a prolific technique to further our understanding of the fundamental nature of matter. This has been studied extensively for proton impact on gas targets [2, 93-95], metal targets [5-9, 15, 18, 38, 39, 41, 45, 51, 59, 82, 84, 88, 92] and other solid targets [4, 15, 16, 23, 24, 41, 59, 60, 71, 84, 87, 88, 93, 96, 113]. There have also been studies, although less common, of C-ion impact on metals and other solid targets [8, 16, 45, 82, 85]. In order to fully understand the need and motivation for these measurements, a brief history and summary of relevant physical phenomena is given in the following sections.

2.2: Ionizing Radiation

Energy can be transmitted to matter as radiation, either in electromagnetic or particulate form, such as photons, electrons, neutrons, protons, and heavier atomic ions. When these charged or neutral particles have energy sufficient to produce ionizations in a medium, they are referred to as ionizing radiation. This is true for both the incident (primary) and secondary radiation that results from an ionization, such as secondary electrons. The effects of radiation on matter have been observed and studied over the course of written history and likely even earlier, with observations of how visible light impacts the growth and transformation of plants. Not long after visible light's effects on silver salts led to the birth of photography in the mid-19^{th} century, Wilhelm Roentgen discovered x-rays in 1895. This ionizing radiation was quickly applied to the medical field as a diagnostic and therapeutic tool and later to industrial applications, well before the fundamental processes or the biological consequences involved were adequately understood. These details are still under investigation today and involve the collaborative efforts of physics, chemistry, and biology in both experimental and theoretical approaches.

Before describing the fundamental physics involved with secondary electron production, some perspective can be gained by considering the various overlapping time scales of the stages of charged-particle irradiation of condensed matter. The shortest time scale of events occurs in the physical stage, followed by the chemical and biological stages. For instance, a fast electron or proton will traverse a water molecule in ~10^{-18}-10^{-17} s, whereas secondary radicals will form and react over ~10^{-3}-10^{4} s. Furthermore, the biological effects of ionization and radical formation, when genetic damage has occurred, can take minutes to years to manifest.

A time-scale summary of events occurring from irradiation of liquid water is given in Table 2.1, adapted from Mozumder and Hatano [65]. The events and stages shown are not

strictly limited to the given time scales and may contain many orders of magnitude of time, therefore Table 2.1 should be viewed liberally as a relative ordering of events. However, an important observation can be made that relatively few events compete within a given order of magnitude. The products of a given stage typically serve as the input to the following stage and so on. In ~10^{-14} s, an H-atom transfer follows the ionization of water (to H_2O^+) in the reaction $H_2O^+ + H_2O \rightarrow H_3O^+ + OH$. These free-radical products may proceed as the instigators of a spur

Table 2.1. Events associated with irradiation of liquid water, and the approximate time scale they occur. Adapted from Mozumder and Hatano [65].

$-\log_{10}$ t(sec) =pt		Event	Stage
	18	Fast electron traverses molecule	Physical
	17	MeV proton traverses molecule; energy loss to fast secondary electrons.	
fs	16	Energy loss to electronic states, (Vertical excitation)	
	14	Fast ion-molecule reaction (H-atom transfer). H_3O^+, H and OH formed.	Physico-Chemical
	13	Solvated electron formed in water. Longitudinal dielectric relaxation in water. Molecular vibration. Fast dissociation.	
ps	12	Electron thermalized or trapped. Spur formed. Self-diffusion time scales in simple liquids.	Chemical
	11	Transverse dielectric relaxation time in water.	
ns	9	Spur reactions continued.	
	8	Charge neutralization in media of low viscosity. Secondary reactions including intertrack reactions.	
	6	Electron escape time in low-viscosity media. Intratrack reactions completed. Secondary radical formation and reaction.	
	0	Radiative lifetime of triplets. Biochemical effects	Biochemical
	−3	Neutralization time for media at very high viscosity. Time for mitosis. Biochemical effects of metastables. DNA synthesis time	
		Biological effects Late biological effects	Biological

reaction, for instance, in a biochemical reaction with the sugar-phosphate backbone of DNA on the 10^{-9} s time scale. A single- or double-strand break that results may then yield an observable biological response at a much later time, that is dependent on many factors like cell cycle and type.

The cascade of events in the target medium result from the successive collisions of fast charged particles with that medium's atoms and/or molecules. Generally, these collisions are Coulombic interactions between the projectile and target electrons. They may be elastic or inelastic, with the latter resulting in an energy transfer from the incident charged particle to the medium.

A simple gauge to describe this energy transfer is the average energy loss per unit path length of the projectile in a material, known as the linear energy transfer (LET). A related quantity is the stopping power $S(\varepsilon)$, which is a measure of the energy received by the medium in the vicinity of the projectile's path. The difference between the two quantities arises from the removal of the deposited energy from the projectile track by fast secondary electrons, Cerenkov radiation, and/or bremsstrahlung radiation [65]. In this context, LET is generally used to describe the incident radiation, while stopping power is more relevant when referring to the target medium. However, theories of projectile energy loss are most often characterized as stopping power theories. Regardless, both LET and stopping power are averaged values and generalizations of the complex interactions that occur when charged particles traverse matter. Therefore, significant fluctuations around these values are to be expected.

Measurements of stopping power are used in conventional dosimetric applications but have become inadequate for determining the spatial distribution of dose, particularly by the

secondary electrons, sometimes referred to as delta rays. This is due to the clinical need to treat ever smaller target volumes and spare sensitive tissues in close proximity to a tumor, for instance. Clinical applications will be discussed in more detail in the following section, followed by a description of the predominant events that contribute to collisional stopping power, i.e. ionization and excitation, as well as electron transfer and dissociation.

2.3: Clinical Applications

Beyond the prolific diagnostic use of radiation in the medical field, where x-ray machines are used anywhere from hospitals to dental offices to chiropractic offices, photons and charged particles are also utilized in high doses for the treatment of cancerous tumors and other malignancies. Ion therapy was first proposed by Robert Wilson in 1946. Then, in 1954 at the Lawrence Berkeley Laboratory (now the Lawrence Berkeley National Laboratory, LBNL), a patient with a pituitary gland tumor became the first to be treated with protons. Two decades later, starting in 1975, carbon and other heavy ions were used to treat hundreds of patients at LBNL [64]. Japan and Germany joined-in during the 1990's by implementing C-ion therapy at the Heavy Ion Medical Accelerator in Chiba (HIMAC) and Gesellschaft für Schwerionenforschung (GSI) in Darmstadt, respectively. GSI has since moved its ion-therapy center to Heidelberg. Today, more than 50% of all cancer patients will receive radiotherapy at some point in the treatment process, typically in conjunction with chemotherapy, surgery, and/or immunotherapy [25].

While MeV x-rays produced by linear accelerators are used in radiotherapy in practically countless clinics across the world, ion therapy with protons and C ions is being employed for the treatment of solid tumors in the clinical setting at an ever-increasing rate [25]. According to the

Particle Therapy Co-Operative Group©, as of April 2018 there were 68 proton and 11 C-ion facilities in operation globally, having treated over 170,000 patients, as well as 60 proton and 6 C-ion facilities under construction or in the planning phase [107].

Radiotherapy is governed by the fundamental principle of maximizing the therapeutic ratio. This is accomplished by applying a prescribed dose to a tumor in a precise treatment volume while minimizing dose and damage to all normal tissues, thereby increasing the probability of tumor control and decreasing the probability of normal tissue complications. Photons penetrating biological material will deposit a maximum dose in the first few centimeters, with a decreasing dose at larger depths as they reach the tumor and continue irradiating tissue distal to the tumor. This is disadvantageous for treating non-superficial tumors because of the higher dose to the skin and other proximal healthy tissues.

In contrast, as heavy charged particles in matter lose energy and slow down, their LET increases and a substantial amount of energy is deposited at a well-defined depth at the end of their range, known as the Bragg peak. This is primarily due to the energy dependence of the ionization cross section, to be discussed in the following section. Using active or passive modulation, several peaks of varying depth in tissue from projectile energies up to ~400 MeV/u can be superimposed to encompass the target lesion by creating a spread-out Bragg peak (SOBP). The upper graph (a) in Fig. 2.1 shows the relative dose vs. depth curve of varying proton energies and the corresponding SOBP that is formed [46]. The lower graph (b) in Fig. 2.1 illustrates the superior dose ratio of tumor to normal tissue by protons and C ions as compared to x-rays [64].

a)

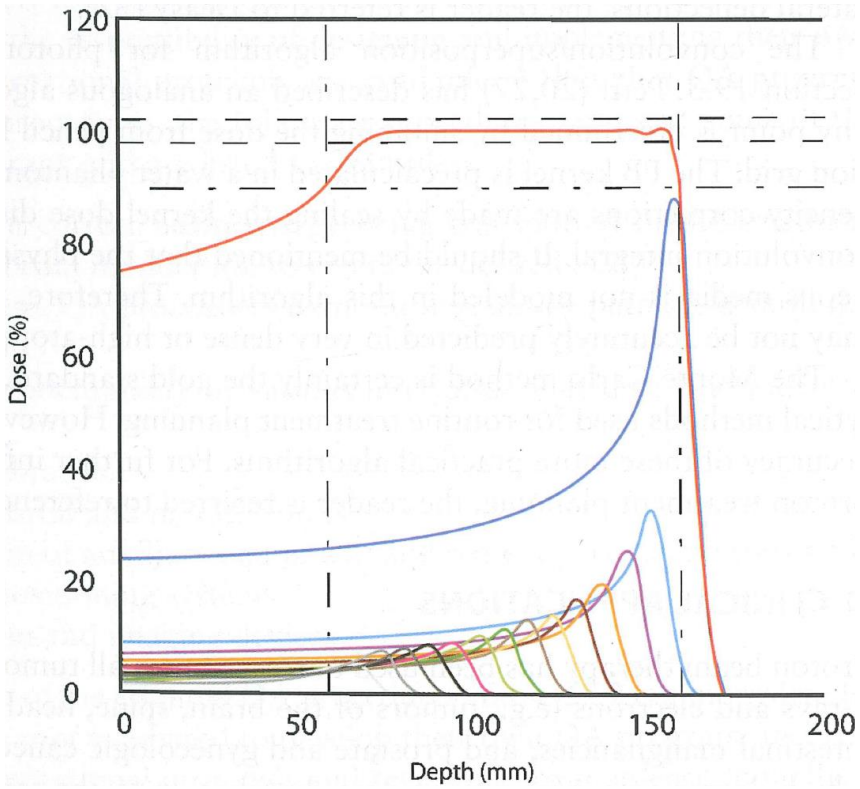

b)

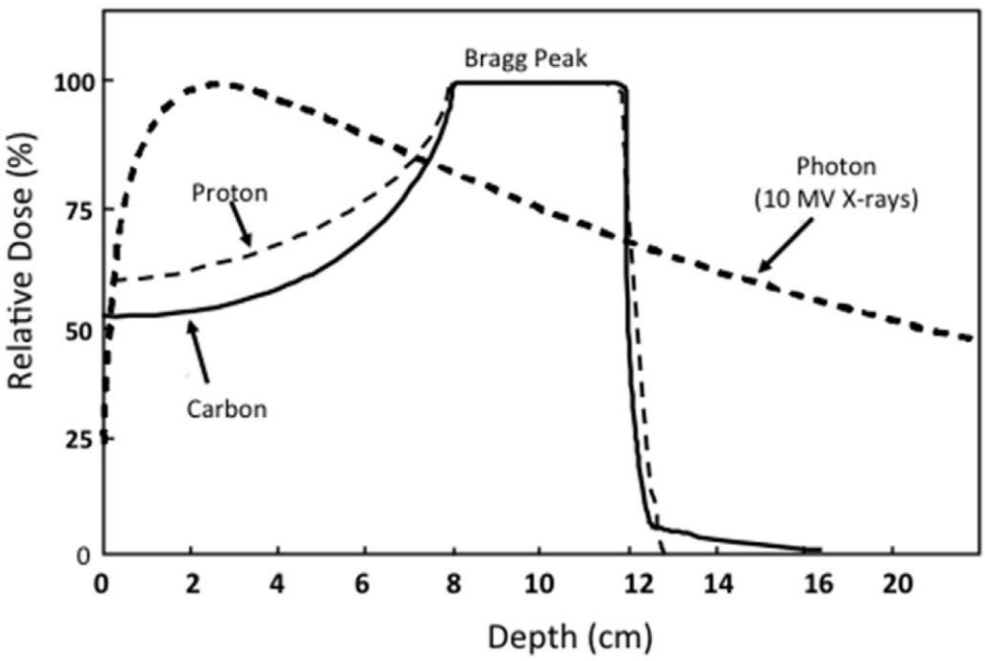

FIG. 2.1. The dose vs. depth curve (a) of 14 proton beams with increasing energy and thus Bragg peak depth are combined to create a SOBP, shown in red, with a nearly uniform dose to a large tumor. Adapted from Kahn [46]. 10 MV x-ray, when compared to protons and C ions (b), delivers ~75% of the dose to a deep-seated tumor while irradiating the healthy tissue both proximally and distally. Adapted from Mohamad *et al*. [64].

It should be noted that protons exhibit a very abrupt distal end fall-off, and therefore nearly zero dose is deposited beyond the Bragg peak or tumor. C ions have a small tail of dose at the distal end, due to fragmentation, but negligible when compared to x-rays. Fragmentation of heavy-ion projectiles, not including protons, results in a reduction of LET and additional range straggling [111]. However, the lateral fall-off around the tumor is steeper with C ions than protons [64]. This is due to the larger mass of C resulting in decreased beam scattering. The overall result is a more conformal dose distribution for a prescribed dose, leading to fewer healthy tissue toxicities and decreased late-effects, particularly in pediatric cases [25]. A comparison of proton and x-ray treatment plans for a prostate cancer patient is shown in Fig. 2.2, adapted from Durante *et al.* [25]. It can be seen that ion therapy has superior dose distribution to x-ray therapy.

In addition to superior dose localization compared to x-ray therapy, ion therapy exhibits a higher relative biological effectiveness (RBE) and lower oxygen enhancement ratio (OER), especially with C ions [26]. RBE is the ratio of dose needed to achieve a given amount of biological damage between a reference type of radiation, x-rays, and an alternative type, such as protons or C ions. Clinically, protons are assigned an RBE of 1.1 while C ions are assigned an RBE of 2-3 [26]. C-ion therapy does not show an oxygen effect, which is a decrease in cell killing due to a lower concentration of O_2 and consequently a decrease in free-radical formation. Therefore, tumors which are typically hypoxic due to poor vasculature are less resistant to C-ion therapy compared to x-rays. Also, C-ion therapy does not show sublethal damage repair and has less cell cycle related radiosensitivity when compared to x-rays [26]. This makes it an ideal treatment choice for radioresistant and/or hypoxic disease.

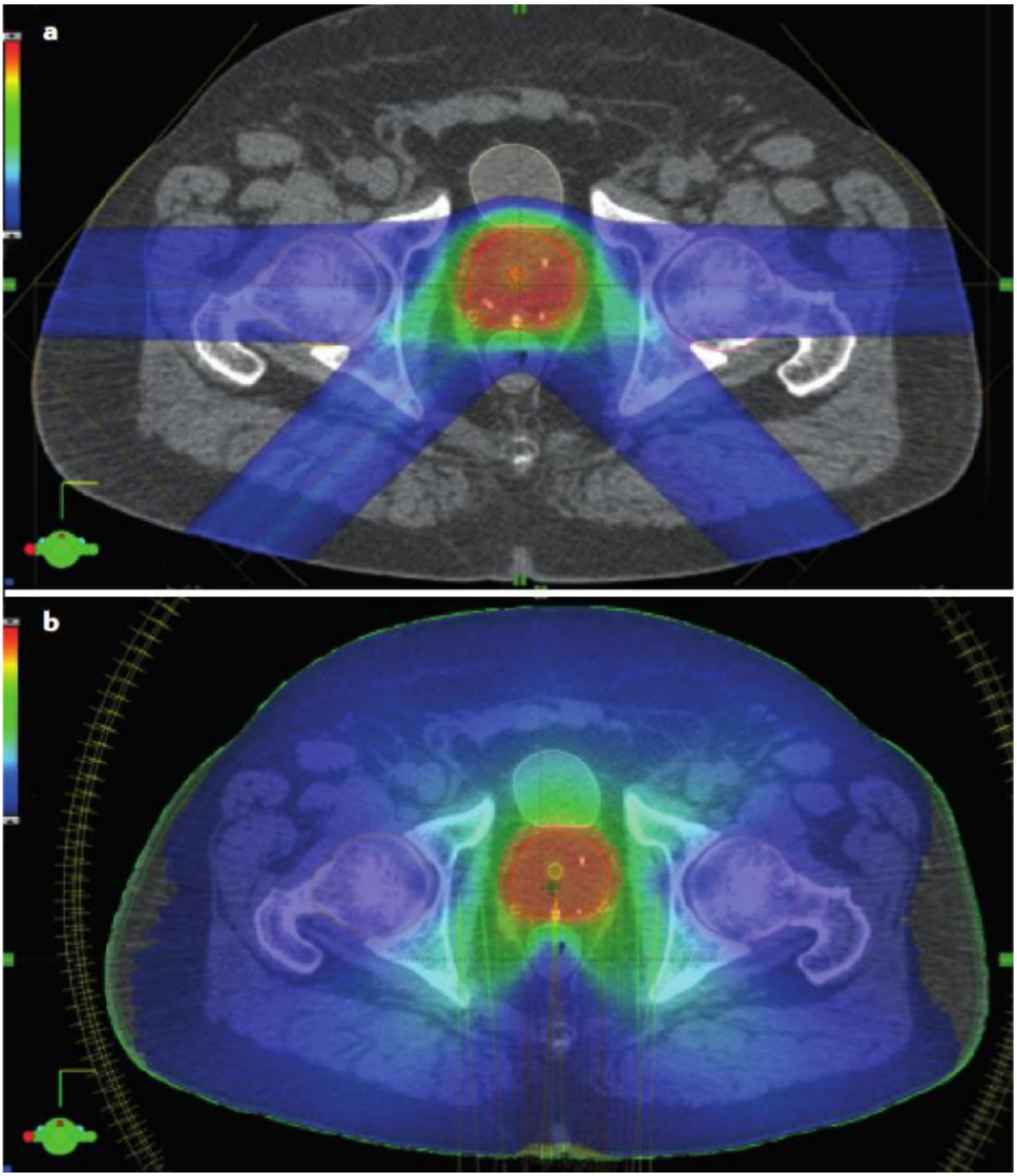

FIG. 2.2. Treatment plans are shown for (a) 4-field Varian ProBeam proton therapy and (b) Varian TrueBeam x-ray volumetric arc therapy of the prostate. The same target dose was delivered in both plans but less integral dose and rectal dose was achieved using protons, even though plan (b) was awarded the top scoring in the 2016 American Association of Medical Dosimetrists and Radiosurgery Society Plan Study. Adapted from Durante *et al.* [25].

An important aspect to consider for the biological outcome of charged-particle interaction with tissue is clustered DNA damage. The spatial and temporal makeup of biological damage from ionizing radiation is correlated to the final outcome. It has been shown that DNA repair mechanisms virtually negate the biological effectiveness of base damage and single-strand breaks; even double-strand breaks may not lead to a lethal effect [36]. However, high-LET radiation has a larger probability of inducing clustered DNA damage, which in turn corelates to a higher RBE [105].

Although ion therapy has several physical and biological advantages to x-ray therapy, larger facilities are required to operate the cyclotron, synchrotron, or synchrocyclotron and the associated beam manipulation equipment needed for ion therapy. Altogether, this entails a cost per treatment 2-3 times higher than that of conventional x-ray therapy [25]. There are several publications demonstrating the benefits of ion therapy and debating the justification for its higher cost [25, 26, 53, 64, 72, 83, 103], and phase-III clinical trials comparing C ions with x-rays or protons are underway [25, 107].

Another aspect of radiotherapy to consider is the use of radiosensitizers, which can enhance the effect of radiation on tissue. Heavy elements, such as high-Z metallic compounds of gold or platinum, are introduced to the tumor site as nanoparticles. This was suggested in the early 1990's for the improvement of x-ray therapy and is currently being studied for ion therapy as well [49, 53, 54, 101]. Radiation enhancement with heavy elements and nanotechnology is one of the factors driving the research performed here, and will be discussed further at the end of this chapter.

2.4: Charged-Particle Interactions with Matter

The phenomenon of ion-induced electron emission from the surface of a solid was discovered at the beginning of the 20th century by J.J. Thomson (1904) and Ernest Rutherford (1905) and has been studied extensively ever since, in an effort to gain insight into the basic structure of solids and the mechanisms of energy loss. The basic interactions between the incident ion and the atoms or molecules of the target material are ionization, excitation, electron transfer, dissociation, and elastic scattering [43]. Collective excitations in condensed-phase targets can also occur, such as volume and surface plasmons in thin films. In an inelastic collision, energy can either be transferred to or from the target atom/molecule. The latter is only important for epithermal and thermal projectiles and won't be discussed here [65].

2.4.1: Target Ionization and Excitation

The momentum transfer interactions are all governed by the screened Coulomb interaction and are stochastic in nature [65]. Primarily, the interactions responsible for projectile energy loss are with the electrons of the absorbing medium. When the velocities of the incident charged particles (atomic ions) or the secondary electrons they have produced are large relative to those of bound electrons, target excitation and ionization are the dominate processes of energy loss [65]. The approximate lower energy threshold for these "fast" projectile ions and secondary electrons is 100 keV/u and 100 eV, respectively. Ionization can be considered an extreme case of target electron excitation, and is sometimes implied when referring to electron excitation. Target ionization results in secondary electron ejection and residual positive ion formation, sometimes accompanied by Auger electron emission and/or characteristic x-ray emission. Auger electrons and characteristic x-rays result from an inner shell ionization creating a vacancy that is filled by an outer shell electron, where the excess binding energy results in either an outer shell

electron emission or a photon, respectively. The residual positive ions, or free radicals, of the target medium can have various final states that range from a ground state to an excited electronic or nuclear state where dissociation or fragmentation can occur. Within the solid, the electron and free-radical products of ionization may travel and deposit energy relatively far from the projectile's path, in so-called "spurs".

Table 2.2 summarizes the main reaction pathways that can result from a charged-particle projectile interacting with a molecular target AB. For the case of atomic ion projectiles P, like protons or C ions, all pathways except electron attachments (l) and (m) are possible. For secondary electrons e_s playing the role of the projectile P, all pathways except electron transfers (n) and (o) are possible. If the target is monoatomic, pathways of fragmentation or dissociation (f)-(h), (j), (k), and (m) are unavailable.

The ionization pathways occur for a wide range of projectile and secondary electron energies. For a fast projectile or secondary electron, the most probable reaction is target ionization as described by (a) in Table 2.2, typically with a valence target electron. As a charged particle slows beyond the threshold where momentum can be transferred in an excitation of target electrons, elastic scattering or nuclear scattering will dominate. This occurs for ions approaching the extreme end of their range, with energies less than a few keV/u [65]. In the intermediate range of projectile energies, a mix of elastic and inelastic processes will occur. The relative proportion of these processes is dependent on the target medium's atomic, molecular, and condensed-phase properties.

Additionally, for heavier charged particles like C ions, energy transfer mechanisms of projectile electron capture and loss become significant. For fast, heavy charged particles of

Table 2.2. Target molecule AB ionization and excitation pathways, when bombarded by a projectile P such as an atomic ion P^q (proton, C ion, etc.) or secondary electron e_s from a previous ionization [43, 65].

P + AB →		**Ionization Pathways:**
(a)	$AB^+ + P + e_s$	Single Ionization
(b)	$AB^{n+} + P + ne_s$	n-Multiple Ionization
(c)	$AB^{**} + P \rightarrow AB^+ + P + e_s$	Excitation → Autoionization
(d)	$AB^{*+} + P + e_s \rightarrow AB^{2+} + P + 2e_s$	Ionization → Autoionization
(e)	$AB^+ + P + e_s + h\nu$	X-ray Emission
(f)	$A^+ + B + P + e_s$	Fragmentation
(g)	$A^+ + B + P + e_s$	Dissociative Ionization
(h)	$A^+ + B^- + P$	Ion Pair Formation
P + AB →		**Excitation Pathways:**
(i)	$AB^* + P$	Simple Excitation
(j)	$A + B + P$	Neutral Dissociation
(k)	$A^* + B + P$	Excited Dissociation
(l)	AB^- ($P = e_s$ only)	Electron Attachment
(m)	$A^- + B$ ($P = e_s$ only)	Dissociative Attachment
(n)	$AB^+ + P^{q-1}$ ($P = H^+, C^{q+}$ only)	Projectile Electron Capture
(o)	$AB^- + P^{q+1}$ ($P = C^{q+}$ only)	Projectile Electron Loss

velocity v_p, a loosely bound electron may be scattered from the projectile with a velocity v_e where

$$v_e(\text{convoy}) \approx v_p . \tag{2.1}$$

This gives an electron energy ε of

$$\varepsilon \approx \frac{1}{2} m_e v_p^2 = T \frac{m_e}{m_p}, \tag{2.2}$$

where m_e is the mass of the electron, T is the kinetic energy of the projectile, and m_p is the mass of the projectile. These electrons lost to the continuum state of the projectile are commonly referred to as "convoy" electrons, since they travel along with the projectile at nearly the same speed and in nearly the same direction.

2.4.2: Stopping Power and Range

The total stopping power of charged particles in matter accounts for all energy loss mechanisms. Measurements of stopping power can be performed with high accuracy (~1%) due to modern charged-particle detection methods [65]. This makes them valuable gauges to test and refine the theoretical models and the understanding of charged-particle interactions with target materials. Numerous published values for various projectile/target combination stopping powers are available, and have been reviewed and conveniently compiled by Ziegler *et al.* [113, 114] along with charged-particle ranges in matter.

The range is the average pathlength an incident particle with an initial energy will travel in a material before stopping. A similar description is the penetration, which is the vector distance between the initial and final endpoints of the particle's path. As such, the (typically elastic) scattering of the projectile particle results in a smaller value of penetration vs. range. Both increase with higher initial projectile energy. Range R and penetration can be estimated with the so-called continuously slowing down approximation (CSDA) and integration of the inverse of stopping power $S(\varepsilon)$ with respect to particle energy ε, as in

$$R_{CSDA} = \int_{\varepsilon_f}^{\varepsilon_o} \frac{d\varepsilon}{S(\varepsilon)}. \tag{2.3}$$

In equation 2.3, ε_o is initial particle energy and ε_f is the final energy when the charged particle is considered to be stopped (thermalized). However, the CSDA formalism ignores fluctuations in energy loss and assumes stopping power is a continuous function of energy.

Due to the stochastic nature of charged-particle interaction and energy deposition in a medium, range straggling exists for projectiles with the same initial and final energies. By virtue of the central limit theorem, the mean-squared fluctuation in energy loss $\langle \Delta\varepsilon^2 \rangle$ of charged particles after travelling a distance x is a Gaussian distribution given by

$$\left(\frac{d}{dx}\right)\langle \Delta\varepsilon^2 \rangle = 4\pi e^4 z^2 NZ\,, \tag{2.4}$$

where e is the elementary charge, z is the atomic number of the projectiles, while N and Z are the number density and atomic number of the target medium, respectively. The corresponding range distribution is gaussian as well. The root-mean-squared (RMS) dispersion is typically a few percent of the mean range for heavy charged particles, and up to a few tens of percent for electrons [65]. Range straggling for electrons is more dominant because of their small mass and the large proportion of energy that they can lose in a single interaction. For thin films, the energy distribution of exiting charged particles will not be Gaussian but will exhibit a high-energy tail.

Figure 2.3 shows typical examples of calculated and experimental stopping powers (a) as well as CSDA range and RMS penetration of electrons in gaseous water (b), adapted from Pimblott *et al.* [76] and Laverne *et al.* [55], respectively. The uncertainty of electron range is important in the radiation biology or radiotherapy context, as the size of a cell may often be

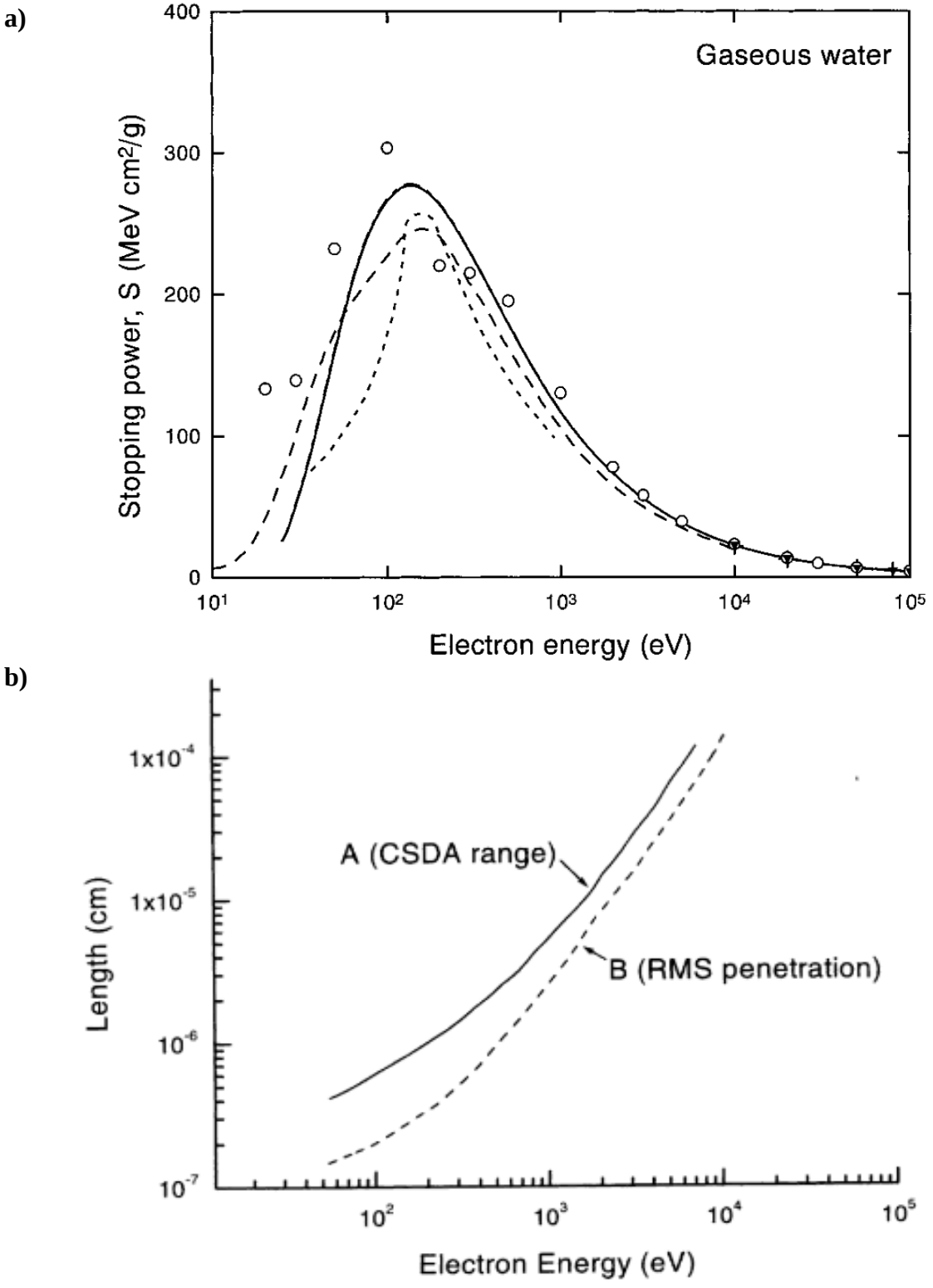

FIG. 2.3. Density normalized stopping power (a) of electrons in gaseous water, adapted from Pimblott *et al.* [76]. CSDA range and RMS penetration (b) of electrons in gaseous water, adapted from Laverne and Mozumder [55].

small compared to the particle range, and the biological effects of radiation in a cell are dependent on the localization of energy deposition in it [65]. MC track-structure simulation, to be discussed further in the next subsection, can provide a numerical solution to the analytical problem of combining elastic scattering with inelastic collision processes.

2.4.3: Theoretical Considerations

Theories and computational models involving cross sections are used to predict and describe the spatial distribution of energy deposition by charged particles in a medium. The cross sections depict probabilities for the various interactions that can occur in ion-induced electron production and transport through a medium. The MC simulation method requires cross section data for the charged-particle projectiles as well as the secondary electrons. These data are still incomplete, particularly for low-energy ionization [41]. Various theories involving energy loss of ions in matter have been developed, modified, and improved over the past century. This started in the early 1900's with Ernest Rutherford, J.J. Thomson and Niels Bohr, followed by many others like H. Bethe, F. Bloch, C. Møller, L. Landau, J. Lindhard, and A. Sørensen, to name a few.

However, the theory involves corrections for relativity, atomic energy structure, electron velocity distribution (shell correction), charge screening, Barkas-Andersen effect (stopping of positive ions differs from negative ions), and Fermi-density effect (dielectric polarization of target) that need to be considered [65, 112]. The manner they are applied can lead to many variations of a theoretical model's end result. Comprehensive cross section data would allow MC simulations to accurately follow the individual interactions of the projectile and all secondary electrons with the medium down to stopping or sub-excitation levels. This method of charged-particle track-structure simulation can also account for the reactive species (free

radicals) as they diffuse in the medium and undergo spur reactions, leading to DNA damage and repair. This is crucial for modeling dose deposition in radiotherapy, because the radial distribution of dose in the plane perpendicular to the beam axis, in biological material, can vary on the nanometer scale [103]. Some recent publications of MC track-structure simulations are available for electrons [69] and protons [1, 21] in water, C ions in water [56] and elemental films [21, 41], as well as DNA damage from protons, C ions, and other atomic ions [33, 103].

Total cross section data can be measured from the secondary electron emission of charged particles traversing a gaseous medium. In this manner, the target density is low enough that the probability of a projectile colliding with more than one target atom/molecule is negligible. Therefore, as detailed in ICRU report 55 [43] and elsewhere, the number of emitted secondary electrons N_e, where

$$\mathrm{N_e} = \mathrm{N_p n L \sigma}\,, \tag{2.5}$$

is proportional to the number of projectiles N_p, target particle density n, and length L of the target along the beam path by a constant σ. This constant of proportionality is called the "cross section" to satisfy the dimensionality of equation 2.5. For condensed-phase targets, where the probability of multiple projectile collisions can be significant, cross section data is extremely difficult to obtain.

MC charged-particle track-structure models rely on accurate information of the spatial distribution of ionization and excitation events. This requires extensive data of interaction cross sections for both the projectile and the secondary electrons with the target material, and is necessary for determining the biological damage following energy deposition by ionizing

charged-particle radiation. As mentioned, this data is available for gaseous targets [2, 43, 93-95].

Figure 2.4 shows a compilation of data from Uehara *et al.* [100] and ICRU report 49 [42] of some of the more important interaction processes of electronic stopping power of protons in gaseous water. It doesn't explicitly show the importance of differential cross sections of ionization that are needed for three-dimensional modelling of charge particle dose deposition in matter, however. The energy and angular distributions of secondary electron production by all charged particles (projectiles and electrons) is crucial for obtaining detailed MC track-structure models. This includes differential cross sections for partially screened atomic ion projectiles that either were initially dressed (not bare) or captured electrons from the target as they slowed.

To model charged-particle dose deposition in condensed-phase targets, scaling of gas target ionization data can be performed as an approximation. But, interatomic/intermolecular forces in the condensed phase can change electron ionization potentials and dielectric properties, for instance. Since differential cross section data cannot be obtained, an alternative measurement approach is needed.

So, doubly differential secondary electron emission yields can be measured to serve as a substitute to cross section data for quantifying the accuracy and validity of MC simulations for condensed-phase targets. This is accomplished by directly comparing these measurements to the doubly differential electron emission output generated by MC simulations mimicking the experimental setup (target/projectile species, target geometry, etc.). Thus, experimental electron emission yields are needed, particularly in the lower energy ranges, to validate or update existing MC code databases and improve the modelling of charge particle dose deposition in biological material.

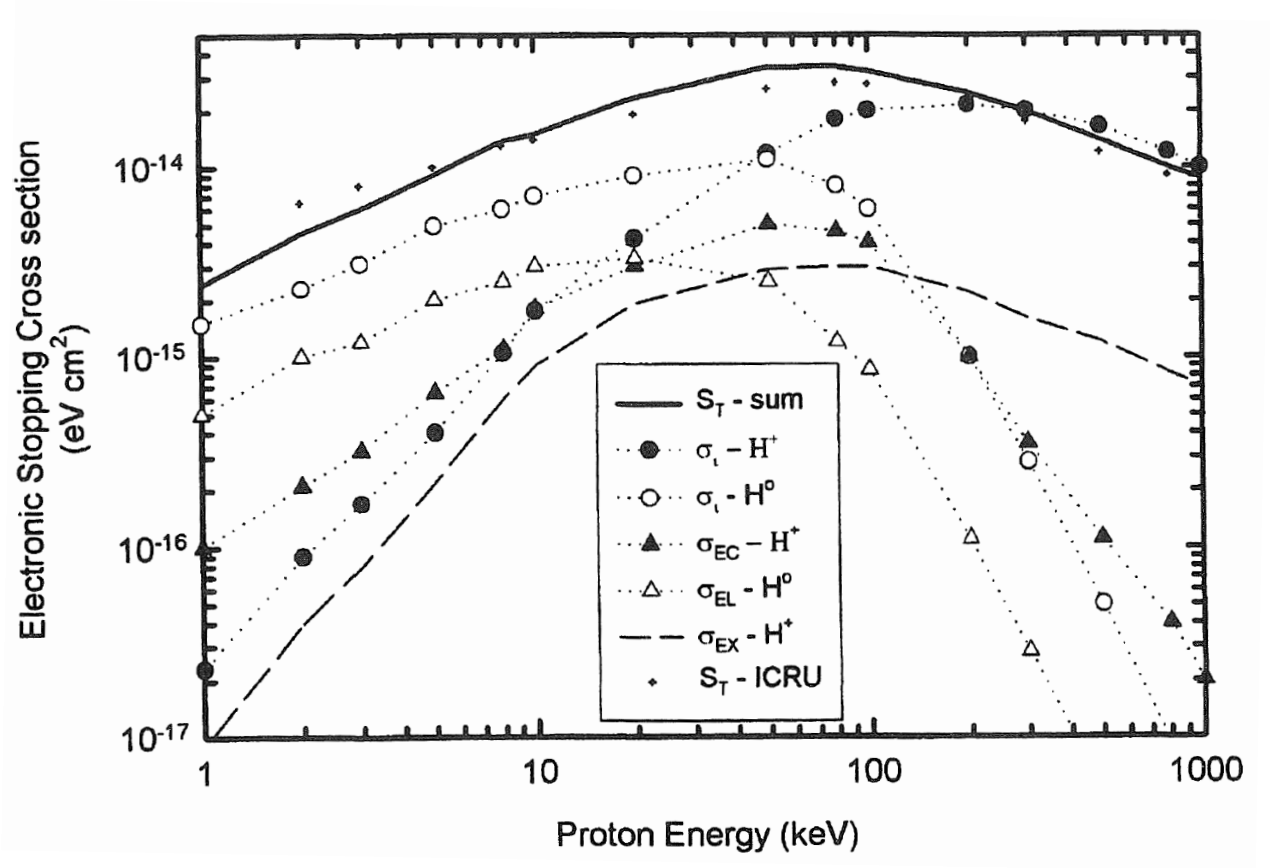

FIG. 2.4. Total stopping power S_T (solid line) and contributions from ionization σ_i by H^+ and H^0, electron capture σ_{EC} by H^+, electron loss σ_{EL} by H^0, and excitation σ_{EX} by H^+ from proton impact on water vapor from Uehara *et al.* [100] and S_T (dots) from ICRU report 49 [42]. Adapted from Mozumder *et al.* [65].

2.5: Secondary Electron Emission from Solids

There are three stages that are commonly used to describe ion-induced electron emission from a solid [40, 43, 65, 78, 89]. First, electrons are generated in the target medium by the projectile in an inelastic collision. Second, these secondary electrons undergo further scattering and energy loss interactions (ionizations) as they slow down and migrate to the surface. Third, they escape through the potential barrier at the surface and can be detected. Therefore, both bulk and surface processes must be understood for the incident particles as well as the secondary electrons they generate. For instance, the dielectric properties, atomic number Z, and purity of the target material are some factors that influence secondary electron transport within the solid. Also, surface conditions such as contamination will affect the surface barrier potential and thereby influence the energy threshold of secondary electrons capable of being emitted from the solid and detected. This is a very important consideration because the focus of the work presented will be on the low-energy portion of the secondary electron emission spectrum.

Spectra of secondary electrons produced by charged particles within a condensed-phase medium are different from gas targets in many respects. The transfer of energy in an inelastic collision depends strongly on the target material, where interatomic or intermolecular interactions alter the target electron energies and behavior. While some materials show little difference in gas vs. solid phase interactions (cross sections) due to weak van der Waal forces, as in argon, nitrogen, and oxygen, metal electronic levels are much different in the two phases [43]. A conduction band of free electrons is formed in condensed-phase conductors resulting in both localized electron excitations and delocalized resonant excitations from charged-particle impact over a wide energy range. These occur in addition to the localized excitations of the more tightly bound inner shell electrons. An intermediate case exists for water and other molecular solids or

insulators where energy transfer interactions are largely, but not exclusively, localized. All forms of target electron excitation may lead to ionization if the amount of momentum transfer is sufficient.

2.5.1: Secondary Electron Production in Solids

The production of secondary electrons in solids was described by the ionization reaction pathways shown in Table 2.2 and discussed in section 2.4.1. In this section, discussion of those reaction pathways for secondary electron production will be limited to only proton and C-ion projectiles. In addition to the pathways discussed previously, there are some specific theoretical descriptions for ionization occurring in condensed-phase targets. These include the binary encounter (BE) approximation and the dielectric response theory for plasmon decay electrons. BE approximation describes theories in which the target electron has an associated momentum distribution.

A free electron gas model can be used to describe the interaction between projectiles and free electrons of a metal target. In this model, the recoil energy and angle of the target electron follow from conservation of energy and momentum, where the angular distribution for an electron with a specific energy is a δ-function [43]. If the charge projectile particle interacts with a bound inner shell electron of a metal or a bound electron in a non-metal, however, the residual positive (target) ion will receive a portion of the total transferred momentum. Therefore, a secondary electron of a specific energy may be ejected at any angle. However, for the case where a considerable majority of the total momentum transferred from the projectile is given to the electron, at a small impact parameter, the angular distribution is sharply peaked in that momentum transfer direction. This classical treatment is called the binary encounter

approximation. The emitted direction θ_{BE} of the BE electrons is given for the non-relativistic case by

$$cos\,\theta_{BE} = \frac{m_e + m_p}{2m_p}\sqrt{\frac{m_p Q}{m_e T}}, \tag{2.6}$$

where m_e and m_p are the masses of the electron and projectile, respectively, T is the kinetic energy of the projectile, and Q is the energy transferred [43]. The angular dispersion of BE electron emission is dependent on the Compton profile, how tightly the electron is bound and the momentum distribution of the electron before impact [65]. The transferred energy Q is the sum of the secondary electron energy ε and the binding energy B, i.e.

$$Q = \varepsilon + B. \tag{2.7}$$

In the classical BE description of a free electron gas, there is no plasmon contribution to the secondary electron spectrum. A plasmon is a collective excitation or oscillation of the nearly free electron (NFE) gas and is described by the dielectric response theory. Plasmons can be excited in both the bulk (volume) and surface of the solid, with a bulk plasmon occurring at a frequency ω_V given by

$$\omega_V = \sqrt{\frac{n_e e^2}{m_e \epsilon_0}}, \tag{2.8}$$

where e, n_e, and m_e are the electron charge, density and mass, respectively, and ϵ_0 is the permittivity of vacuum (8.854 x 10^{-12} $C^2/N{\cdot}m^2$) [40, 43]. The frequency ω_s of a surface plasmon is related to the bulk plasmon frequency by

$$\omega_s = \frac{\omega_V}{\sqrt{2}} \ . \tag{2.9}$$

The corresponding energy ε_V of a bulk plasmon is

$$\varepsilon_V = \hbar\omega_V \ , \tag{2.10}$$

where $\hbar$=1.055 x 10^{-34} J·s is the reduced Planck constant. Likewise, a surface plasmon will have an energy ε_s related to its plasmon frequency by

$$\varepsilon_s = \hbar\omega_s \ . \tag{2.11}$$

A low-energy threshold exists for plasmon excitation, but at increasing projectile velocities the contribution of plasmon excitation to stopping power approaches that of localized electron excitation [43]. When the plasmon decays, its energy can be transferred to an electron. In this manner, the deposited energy (initially from the projectile) becomes localized and produces a secondary electron of energy ε_V or ε_s, depending on the origin of the plasmon.

2.5.2: Secondary Electron Transport and Escape from a Solid

Following charged-particle production in a solid target, all secondary electrons will undergo elastic collisions with angular scattering and inelastic collisions with energy loss and further target ionization (secondary electron "cascade"). Some will then either reach the end of their range and be absorbed by the target or escape through the surface potential barrier into the vacuum where they can be detected. Fig. 2.5, adapted from Rothard *et al.* [81] shows a schematic representation of these processes in a thin target foil with a projectile ion of initial charge q_i and final charge q_f. Secondary electrons escaping the solid are produced at varying depths beneath the surface, within the range dictated by their initial energy. They provide information on the interactions resulting from collisions varying from "soft" to "hard",

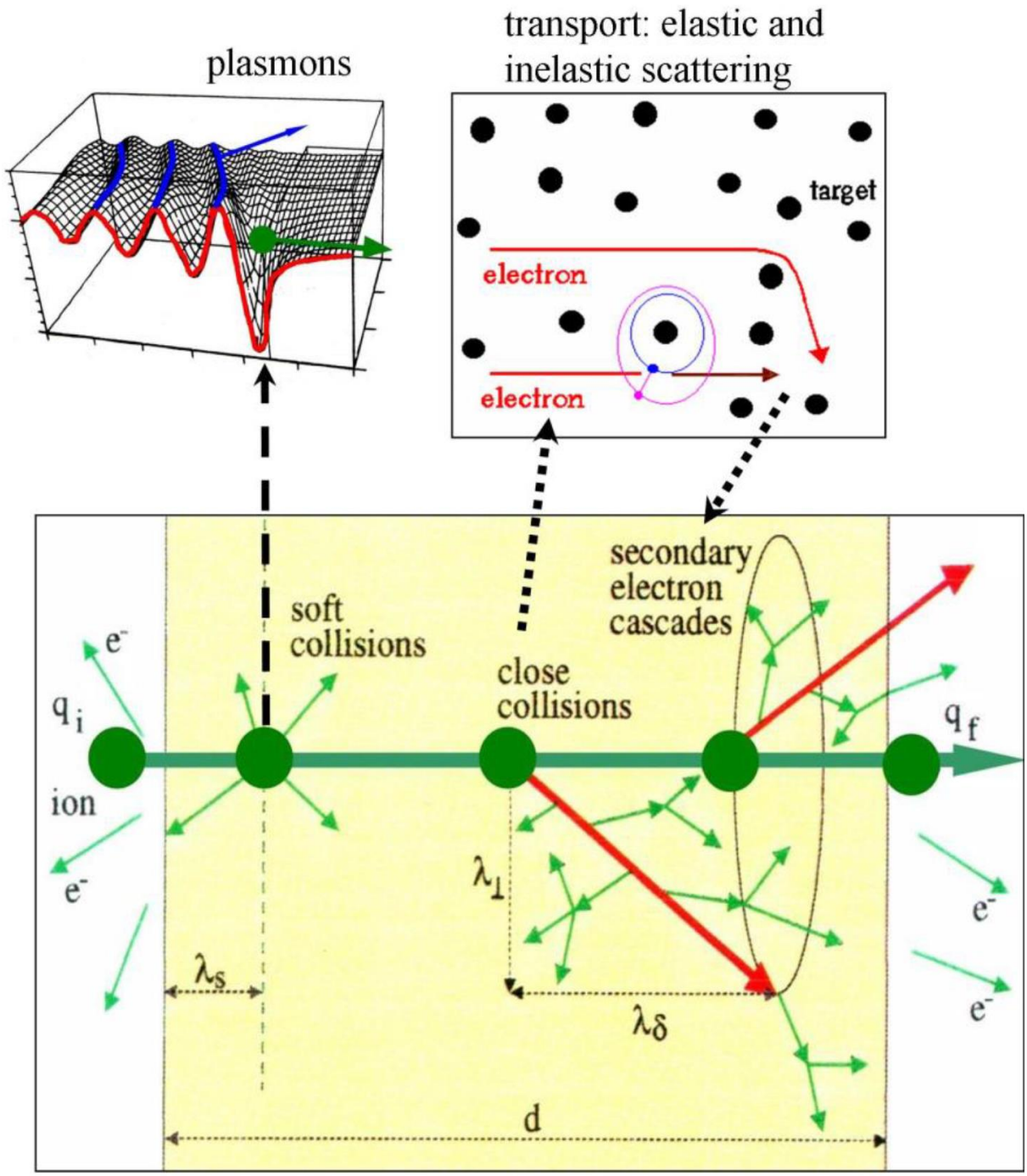

FIG. 2.5. Schematic of mechanisms involved in secondary electron emission for a thin foil target of thickness d after ion bombardment with initial charge q_i and final/exit charge q_f. Close collisions produce fast or BE electrons, while either soft collisions or plasmon decays (upper left) produce slow electrons. Secondary electrons undergo elastic and inelastic scattering during transport in the target medium (upper right). Adapted from Rothard *et al.* [81].

describing the impact parameter or distance of closest approach of the projectile and target electron.

Ion-induced secondary electrons in the low-energy range ε<50 eV, which comprise the majority of the electron energy spectrum, are the focus of the work presented in the following chapters. The internal motion of secondary electrons in this energy range is determined primarily by the band structure of the solid and the interactions with metal target conduction electrons [43]. The mean free path for low-energy electrons in Au and water is <1.5 nm and <4 nm, respectively [3]. Therefore, almost all slow electrons that are emitted from the Au or ASW targets have undergone a series of inelastic and elastic collisions. As such, essentially all secondary electrons that reach and escape the surface of the solid will have changed course and lost energy, compared to their initial conditions following ionization. This is also true for those not destined to escape the solid, and this means the internal distribution of electrons is isotropic [78]. For these secondary electrons, their behavior as they approach the end of their range can be considered diffusion-like [89].

The secondary electrons escaping from a solid target must overcome the surface barrier potential, which is dependent on the material. The barrier height in conductors $U_B(conductor)$ is the sum of the Fermi energy E_F and the work function of the metal Φ, i.e.

$$\mathrm{U_B(conductor)} = \mathrm{E_F} + \Phi\,. \tag{2.12}$$

The Fermi energy is the height of the conduction band and varies from 1-15 eV, while the work function is the energy gap from the conduction band to the vacuum level and for most metals typically varies between 4-6 eV, but can be less for the alkali metals [43]. So, a secondary electron reaching the surface of a metal will lose energy of ~5-21 eV in order to overcome the

surface barrier potential. For insulators, the surface barrier height $U_B(insulator)$ is equal to the electron affinity E_A, as in

$$\mathrm{U_B(insulator) = E_A}\,, \tag{2.13}$$

where E_A is slightly less than 1 eV for most insulators [43]. An electron will only lose energy of ~1 eV in order to escape.

For either case of conductor or insulator, only electrons with a component of kinetic energy, given by the component of velocity perpendicular to the surface, that exceeds the surface barrier potential will escape. By conservation of energy, the emitted electron will have an energy ε that is the difference of its energy inside the solid ε_i and the surface barrier potential, i.e.

$$\varepsilon = \varepsilon_\mathrm{i} - \mathrm{U_B}\,. \tag{2.14}$$

The probability $P(\varepsilon)$ of escape for an isotropic distribution of secondary electrons inside the solid is given by

$$\mathrm{P(\varepsilon)} = 1 - \frac{\mathrm{U_B}}{\varepsilon_\mathrm{i}}. \tag{2.15}$$

Only electrons inside the solid with a velocity vector inside an escape cone defined by a maximum angle $\theta_{i,max}$ measured to the surface normal will escape. The angle defining this escape cone is given by

$$\theta_{\mathrm{i,max}} = cos^{-1}\left(\sqrt{\mathrm{U_B}/\varepsilon_\mathrm{i}}\right). \tag{2.16}$$

In this manner, penetration of secondary electrons through the surface barrier is a refraction phenomenon: only the perpendicular component of velocity will be reduced and the emitted electron will bend away from the surface normal [78].

2.5.3: Total Electron Emission Yield

The total number of electrons emitted from a solid target per incident projectile is called the total electron emission yield, or simply total yield, denoted by γ. Total yields include the full range of electron energies ε. However, "total yield" has been used in the literature to define electrons emitted over the entire space at all angles θ relative to the projectile velocity as well as those emitted only over the half space prior to the target, i.e. electrons emitted in the backward direction. The ambiguity will be avoided here, by distinguishing total backward yields γ_B and total forward yields γ_F from total yields γ, where

$$\gamma = \gamma_B + \gamma_F \,. \tag{2.17}$$

Only total backward yields are able to be measured for targets thicker than the range of the projectile. This is a common experimental setup. However, a thin target such as a foil can be used when measuring total yields. The thickness of a thin target must be less than the range of the projectile and greater than the escape depths of the secondary electrons, which is on the order of ~1-10 nm for conductors and increases to ~10-50 of nm for insulators, due to their inefficient slowing of electrons [43]. With this condition for thin target thickness exceeding the range of secondary electrons, γ_B for thin and thick targets are equal by definition.

The total yield is dependent on the projectile energy and charge state, as well as the target material. For the case of proton-induced electron emission, the total yield is proportional to the electronic (inelastic) stopping power S_e by a material parameter Λ in the relation

$$\gamma = \Lambda S_e = \frac{PL}{2I} S_e \,, \tag{2.18}$$

where P is the probability of an electron escaping the solid as given in equation 2.15, L is the mean free path of the electron, and I is the mean ionization potential of target electrons [40]. Therefore, the (PL/2I) term is dependent only on the material and considered a constant. The relationship in equation 2.18 has been confirmed experimentally within 10% for proton projectile energies from 10 keV to 24 MeV [40].

This can be seen in Fig. 2.6 for proton impact on Au, Ag, Cu, and Al targets, adapted from Hasselkamp *et al.* [40]. In this figure, the total backward yield is used shown and plotted vs. proton energy using the relation

$$\gamma_B = \Lambda_B^* S_e \,, \tag{2.19}$$

where Λ_B^* is the experimental material parameter for backward electron emission. The equivalent forward material parameter Λ_F^*, with a proportional relation given by

$$\gamma_F = \Lambda_F^* S_e \,, \tag{2.20}$$

has also been found to be valid [18].

Derivations from equations 2.18 and 2.19 are observed for heavy ions, such as C ions, particularly at low projectile velocities at energies <150 keV/u [80]. The material parameter is known to depend on the projectile atomic number Z_p, and thus can no longer be interpreted as a "material" parameter. For increasing Z_p, the value of Λ^* decreases [7, 80]. A major reason for this may be the effective charge of the heavy ion, which can change within the escape depth of the secondary electrons. This would result in an electronic stopping power that changes as the heavy ion travels through the target. As a fast positively charged heavy ion slows, it can capture

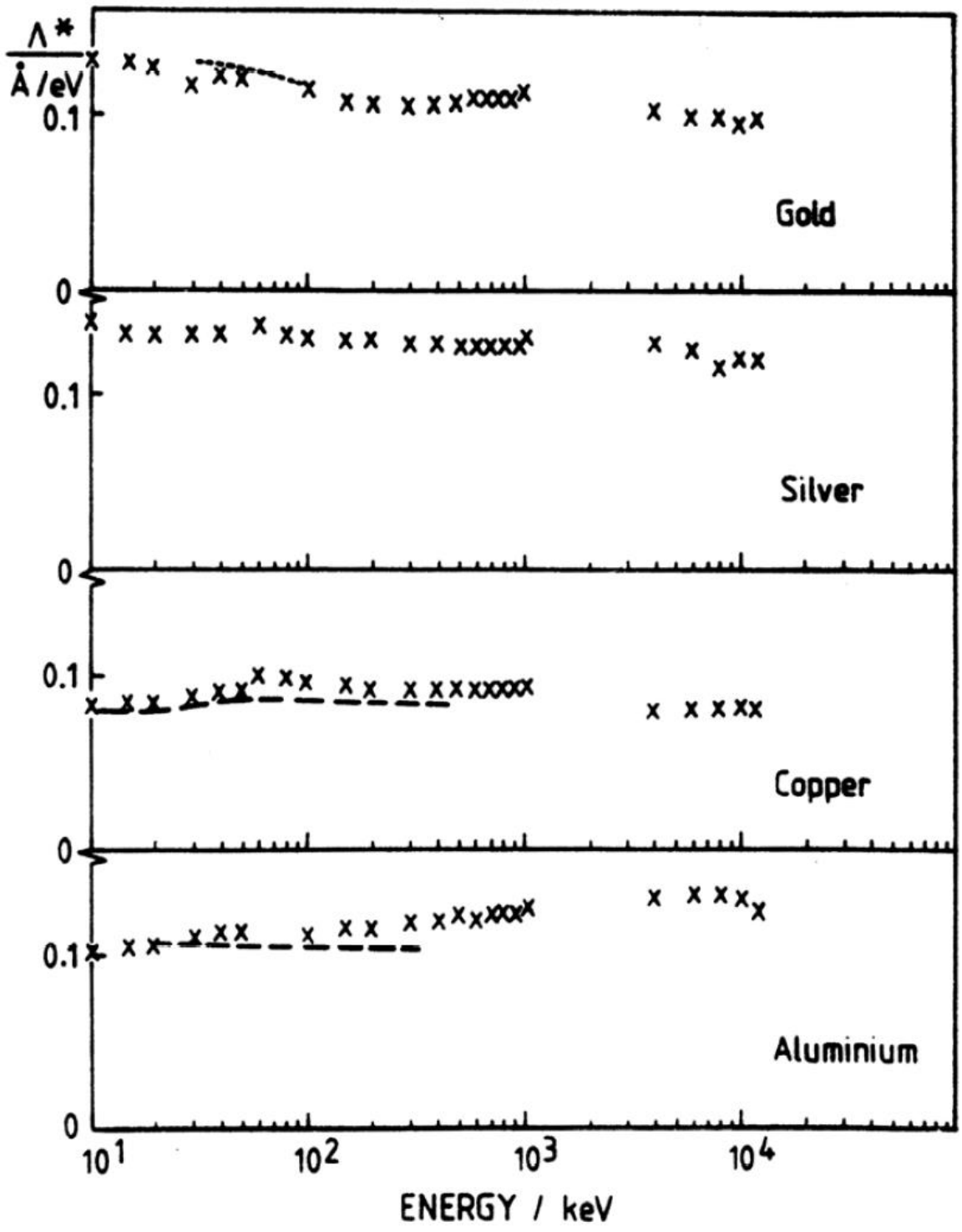

FIG. 2.6. Total backward yield, plotted as $\Lambda_B^* S_e$, from proton impact on metal targets over a wide projectile energy range. Adapted from Hasselkamp *et al.* [40].

and lose electrons. This leads to an evolving "average charge" or equilibrium charge as the ion travels through the target. The projectile may even become neutral in the extreme case, at very low energies [43].

The depth in the target where the projectile reaches charge equilibrium can be tens of nanometers and exceed the escape depth of electrons [50]. Electrons bound to the projectile will reduce the Coulomb interaction of the projectile with target electrons, thereby reducing the stopping power [16]. In the theory of stopping power discussed in section 2.4, cross sections are scaled according to projectile atomic number as Z_p^2, but a more appropriate value in this scaling is the effective charge of the projectile, i.e. Z_{eff}^2. In addition to being dependent on atomic number Z_p, the effective charge is dependent on the instantaneous projectile velocity. Also, as the projectile continues to slow, the Z_p^2 or scaling becomes invalid due to the secondary electron experiencing attractive forces from the residual target ion and the (now scattered) projectile [43].

2.5.4: Singly Differential Electron Emission Yield

The differentials of the total secondary electron emission yield with respect to energy ε or emission angle θ are helpful in illustrating and understanding the fundamental processes involved in secondary electron emission and stopping power of charged particles in matter. The energy distribution $d\gamma/d\varepsilon$ of secondary electron yield over all angles for a given electron energy is also designated as $\gamma(\varepsilon)$. Likewise, the angular distribution $d\gamma/d\theta$ over all energies at a fixed angle can be designated as $\gamma(\theta)$. The energy distribution for a thick target can only be obtained in the backward direction, i.e. $\gamma_B(\varepsilon)$. An experimental setup with a thin target can measure an energy distribution that incorporates electrons emitted from all angles, although it is useful to investigate any differences in the forward and backward direction, i.e. $\gamma_F(\varepsilon)$ vs. $\gamma_B(\varepsilon)$.

Some typical results for secondary electron energy distributions of charged-particle impact on solids show a dependence on projectile and target combination, as expected. For a given combination, the energy distribution shows a dominant low-energy peak at an electron energy of several eV, as seen in Fig. 2.7, adapted from Hasselkamp *et al.* [39]. The low-energy peak position and shape is determined by both the surface barrier potential and the rate of energy loss (stopping power) of the secondary electrons migrating to the solid surface [43]. Fig. 2.7 (a) shows the electron energy distribution in the backward direction $\gamma_B(\varepsilon)$ from 0.5 MeV proton impact. It can be seen that the low-energy electron peak position depends on target material, varying from 1.8-3.6 eV. In the lower graph (b), the low-energy peak position does not depend on projectile velocity (energy), but the yield increases as the projectile slows.

The purity and surface conditions of the target are major factors, in addition to the choice of target material. Contamination of the surface greatly affects the number and energy distribution of electrons <10 eV, as mentioned. Because surface contaminants on metals are likely oxides or other insulators, the surface barrier potential is lowered when a solid target is contaminated or "dirty" and the secondary electron yield is expected to increase [10, 27]. This shifts the dominant, low-energy electron peak to lower energy and higher magnitude. So, energy distributions only reliably depict electron emission from the target element if the surfaces are sputter cleaned and in ultra-high vacuum conditions. Otherwise, the secondary electron yield begins to resemble that of the contaminant material.

Conversely, surface contamination by oxide insulators can decrease the electron yield due to target charging effects [4]. As the target is bombarded by ions and emits secondary electrons, an insulator or metal with a sufficiently thick contamination layer will become

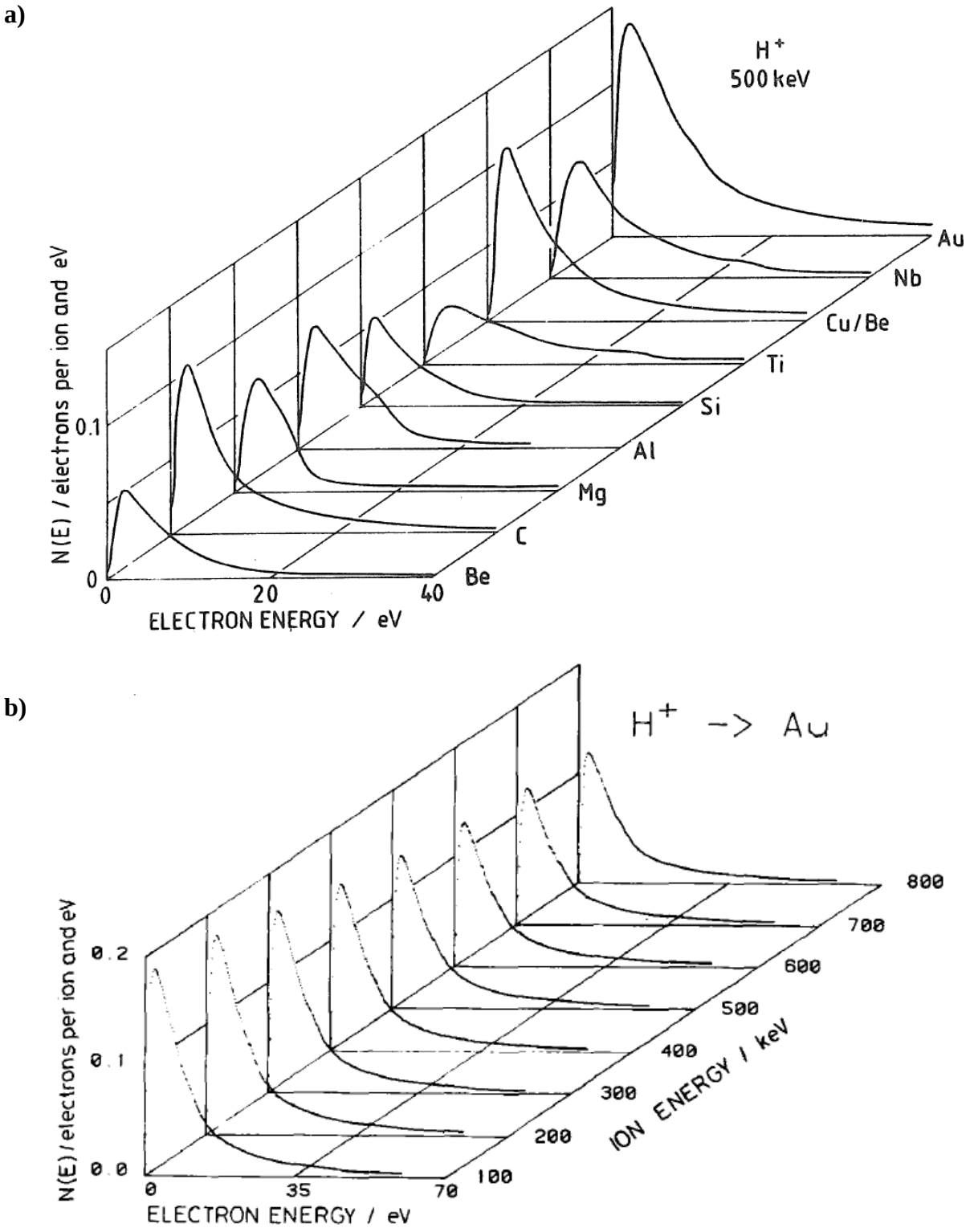

FIG. 2.7. Energy spectra $\gamma_B(\varepsilon)$ of secondary electron emission in the backward direction from (a) various targets by 500 keV proton impact and (b) Au target by 100-800 keV protons. Adapted from Hasselkamp *et al.* [39].

positively charged. Thus, the slow secondary electrons, which are the majority, might not escape the target and the yield will decrease.

2.5.5: Doubly Differential Electron Emission Yield

The differential of the total secondary electron emission yield γ with respect to both electron energy ε and emission angle θ, i.e. $d^2\gamma/(d\varepsilon d\theta)$, is the most illustrative and useful description of electron emission from solids. Also designated as $\gamma(\varepsilon, \theta)$, these yields contain features that provide information on electron emission processes that are affected by either energy or angle. Some of these features are associated with electrons produced by hard and soft collisions, plasmon decays, binary encounters, loss and capture to the projectile continuum (convoy electrons), and Auger emission from both target and projectile particles.

Fig. 2.8(a) is a generic representation of some typical features of doubly differential electron emission spectra for two electron emission angles, $\theta_2>\theta_1=0°$, adapted from Frischkorn *et al.* [34]. For $\theta_1=0°$, the electrons are emitted from the target in the same direction as the projectile beam. For $\theta_2>0°$, the electrons are emitted from the target at a small angle relative to the beam, i.e. 10-20°. Fig. 2.8(b) shows the first results from sputter-cleaned thin-foil electron emission in ultra-high vacuum (UHV) conditions, where the pressure is <10 nTorr. The data is from proton impact on a C-foil target at $\theta=0°$, shown on a velocity scale (upper) and energy scale (lower), adapted from Rothard *et al.* [80]. Both spectra reveal a dominant low-energy electron peak, followed by either a target Auger peak or a "cusp" peak of electrons travelling at the projectile velocity, i.e. $v_e=v_p$. Auger peaks are less pronounced in solid targets than gas targets, and are often not resolved in the electron spectra due to scattering and energy loss during transport to the solid surface. This de-resolution effect holds true for every feature in ion-induced secondary electron emission spectra from solids. The high-energy portion of electron

a)

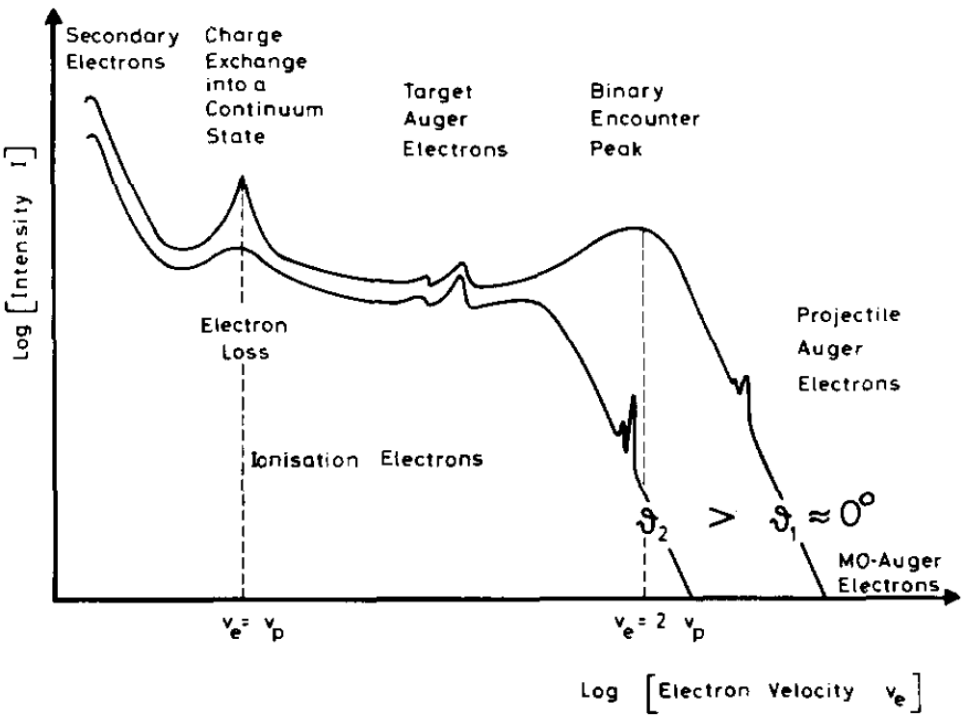

b)

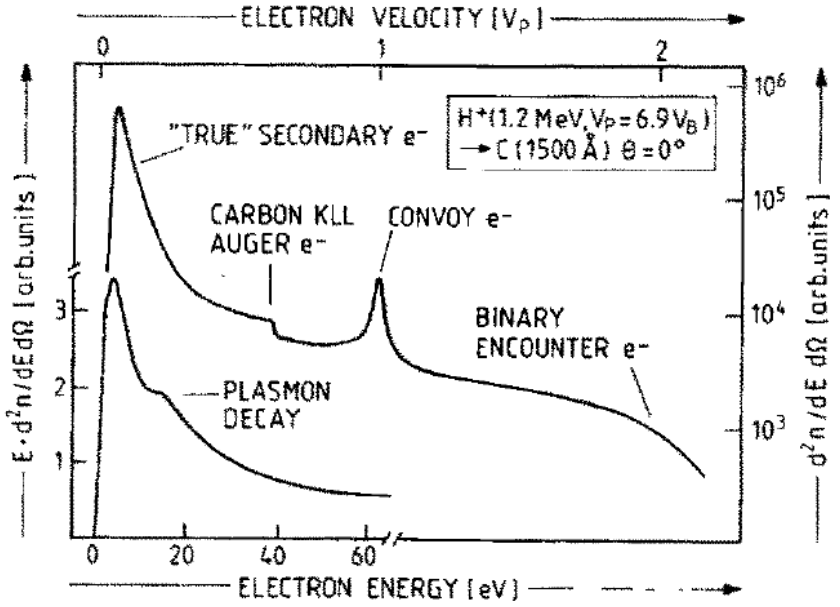

FIG. 2.8. Generic representation (a) of doubly differential electron yields at $\theta_2 > \theta_1 = 0°$, adapted from Frischkorn *et al.* [34] and data from proton impact on C foil at $\theta = 0°$ (b) shown on a velocity scale (upper) and energy scale (lower), adapted from Rothard *et al.* [80].

emission spectra show the BE peak (where $v_e=2v_p$ at $\theta=0°$) with or without projectile Auger electrons superimposed. Projectile Auger electrons are Doppler shifted due to being emitted from a moving source. The BE peak is located at lower energy (and electron velocity) as the emission angle increases above 0°, due to conservation of momentum. The C foil electron yield shows a plasmon decay peak, which is only observed in certain metals, like Al, Mg, C, and Cu where the contribution to secondary electron yield becomes significant [43].

2.6: Applications of Electron Emission Data

To test the MC track-structure models of the spatial distribution of dose deposited by charged-particle interaction with tissue and the cross sections they employ for condensed-phase materials, Au foil and ASW targets were chosen. Water constitutes roughly 80% of soft tissue by mass, and as such is the medium of choice for both theoretical models and experimental setups. Additionally, heavy elements have been shown to enhance the biological effectiveness of ionizing radiation, particularly by an enhancement of densely localized secondary electrons via the Auger process [49, 54]. In combination with the enhanced dose conformity and higher RBE of ion therapy, the combination of ASW on Au-foil substrates was chosen as a target for proton and C-ion irradiation studies of secondary electron emission.

2.6.1: Amorphous Solid Water

ASW is an ideal choice for mimicking the morphology of liquid water in the ultra-high vacuum (UHV) conditions necessary for measuring secondary electron yields, where liquid water instantly vaporizes. The deposition mechanisms, layering, surface conformity, porosity, and density of ASW have been studied for both biological and space applications [11, 47, 48, 77,

90]. The molecular distribution of ASW is similar to liquid water, but slightly more ordered, making it the preferred substitute compared to crystalline ice [48]. Water vapor introduced by the background dosing technique at low temperatures is not crystalline, but rather an amorphous solid. This technique requires a diffuse distribution of water vapor at pressures less than ~10 μTorr. At these low pressures, cubic crystalline ice is formed at temperatures between ~135-200 K, and hexagonal crystalline ice is formed above 200 K [47]. Below 135 K, water vapor condenses in UHV as a microporous amorphous film, with a varying density of approximately 0.6-0.93 g/cm^3 dependent on substrate conditions, temperature, and incidence of the water molecules [11, 90].

It has been shown that layer-by-layer growth of ASW occurring for random deposition in the temperature range of 20-130 K can be based on the "transient mobility" model [48]. In this manner, ASW grows as a flat, thin condensate with a very narrow Gaussian distribution of thickness, as seen in Fig. 2.9 by Kimmel *et al.* [48]. Therefore, at 100 monolayer (ML) thickness, 80% of the ASW film will have a thickness of either 99, 100, or 101 ML with constant density throughout [48]. Also, in the temperature range <130 K, water molecules impinging on a substrate will undergo an absorption rate with a coefficient of ~1.0 where every molecule that contacts the surface "sticks" to it [11]. This allows the thickness of films of ASW to be estimated based on the pressure of the water vapor in the vacuum chamber and the time of exposure.

2.6.2: Heavy Elements

The emission of Auger electrons was briefly discussed previously, where an inner-shell ionization leads to a process of deexcitation of an outer-shell electron filling the vacancy. This initiates a competing process of emission of either a characteristic photon or an Auger electron.

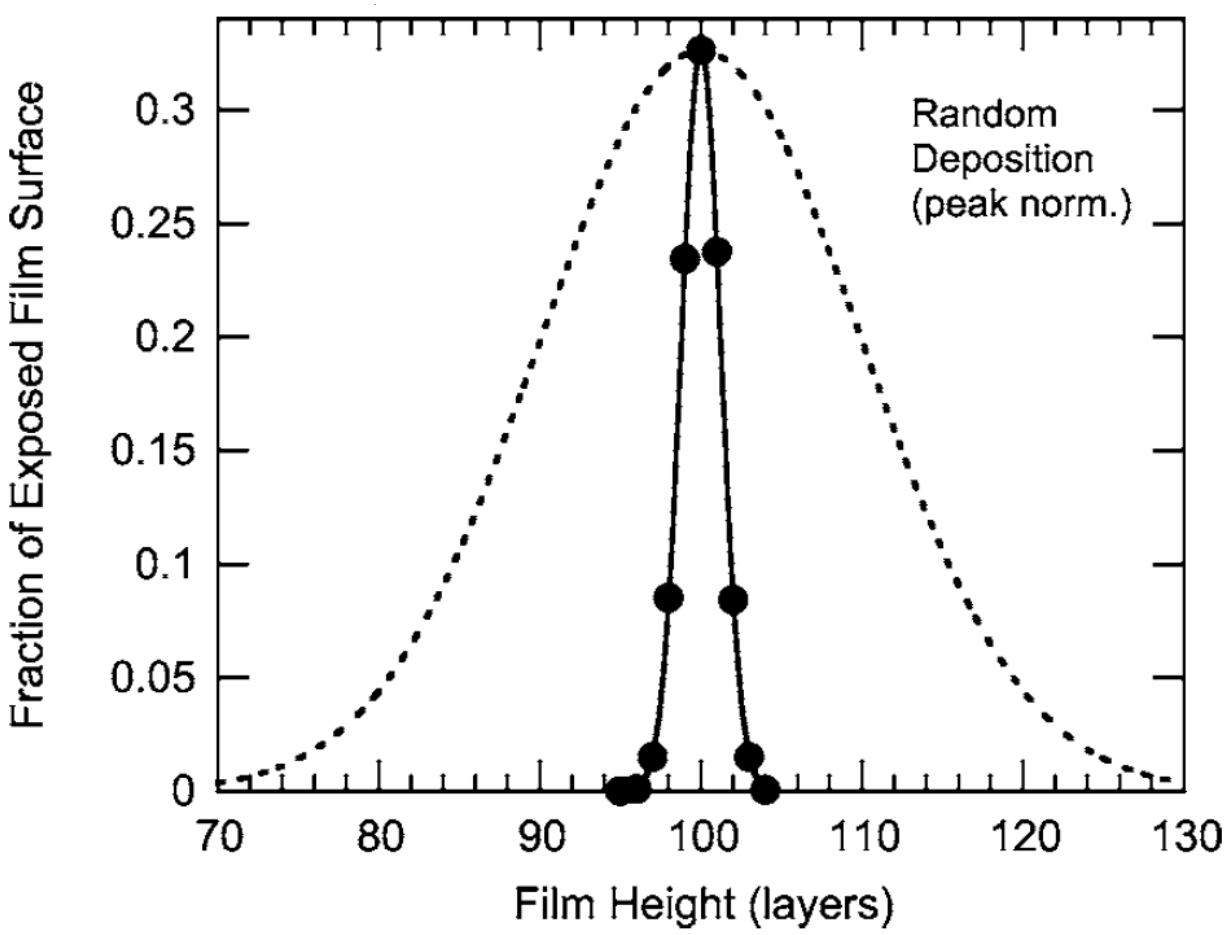

FIG. 2.9. The fraction of exposed film surface of a 100 ML ASW condensate, under random deposition with the transient mobility model (solid line) shows a full width at half maximum of 3%, correlating to an 80% coverage of ±1 ML. The dashed line represents random deposition without transient mobility. Adapted from Kimmel *et al.* [48].

In the latter, a single vacancy in an inner shell initially leads to two secondary electrons and two vacancies in an outer shell. For lighter elements with only a few occupied electron orbitals, just one transition of an outer-shell electron into the inner-shell vacancy is energetically possible, and the two vacancies remain unfilled. For heavier elements, however, those two vacancies can be filled by electrons in even higher orbitals. This results in a so-called "Auger cascade" and the emission of many secondary electrons, ~30 for a K-shell ionization of platinum, for instance [49]. The overall result of the presence of heavy elements in a medium irradiated by charged particles is densely deposited clusters of dose, which is known to enhance the biological effect of radiation [36, 104, 105]. This has been shown to override DNA repair mechanisms and enhance the killing of cells [54]. Fig. 2.10 shows a schematic of the clustered dose deposition that can occur from a Pt Auger cascade (upper left inset) leading to indirect damage of a DNA molecule by either secondary electrons or free radicals, adapted from Kobayashi *et al.* [49].

The incorporation of heavy elements into living cells without producing toxic effects has been accomplished with nanoparticles of diameter <200 nm (small enough to permeate blood vessel walls) and coated with organic or other hydrophilic moieties, as reviewed by Peukert *et al.* [75] and Lacombe [53]. Platinum and gold are currently the most promising choices for nanoparticle therapy. Although the secondary electron emission from Au in nanoparticle form is not expected to mirror that of Au foil, there still exists a need to improve the cross-section input used for Au targets in MC track-structure models.

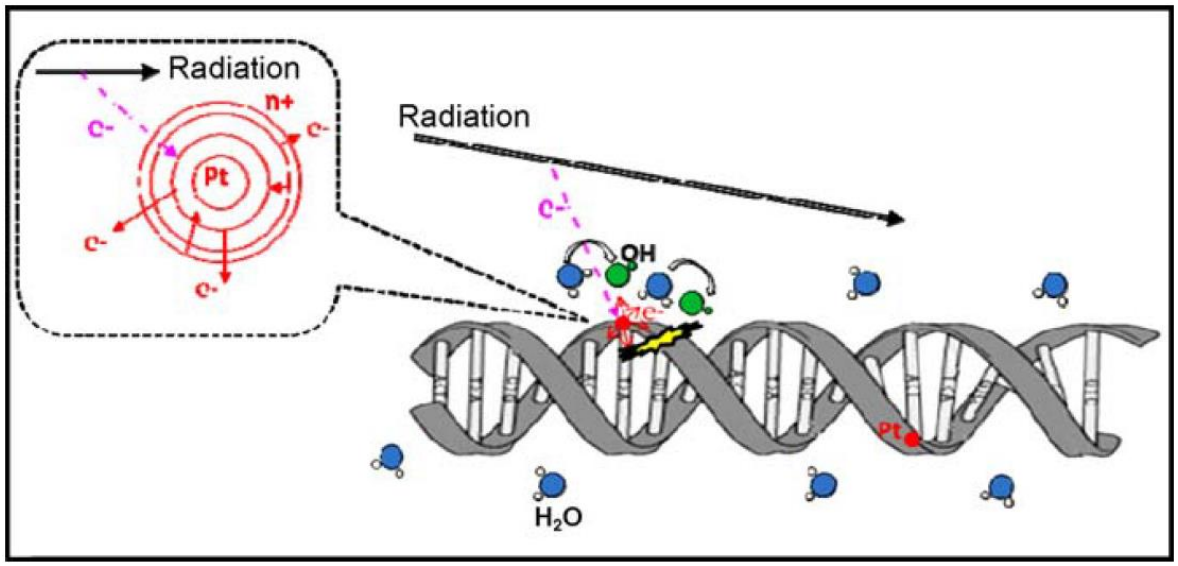

FIG. 2.10. Graphic representation of clustered dose deposition near a DNA molecule from the Auger cascade of Pt, creating free radicals and enhancing the damage. Adapted from Kobayashi *et al.* [49].

Chapter 3: Experimental Materials and Methods

3.1: Introduction

The measurements of doubly differential secondary electron emission yields $\gamma(\varepsilon, \theta)$ to be discussed in the following chapter, where ε is electron energy and θ is the electron emission angle relative to the projectile velocity, were obtained in the Accelerator Laboratory in the Physics Department of East Carolina University (ECU). This laboratory underwent a complete renovation in 2011, followed by the installation and commissioning of a newly built 2-MV tandem electrostatic Pelletron accelerator from National Electrostatics Corporation® (NEC). The ancillary equipment, some of which was custom built by ECU personnel, was installed and tested over the following year. Since then, four experimental beamlines were constructed for condensed and gas phase electron emission studies, cell irradiation and survival studies, and material analysis employing proton-induced x-ray emission. Currently, two additional beamlines are under construction for optically stimulated luminescence and microbeam irradiation studies.

The condensed-phase target experimental beamline was utilized for the work presented here, where 1-4 MeV protons and 2.4-6 MeV C ions collided with 1 μm Au foils with or without cryogenically condensed, purified water vapor films. The projectile beam was pulsed to allow time-of-flight (TOF) energy analysis of emitted secondary electrons. The TOF technique is superior for electrons in the low-energy range, $\varepsilon < 50$ eV, which comprise the bulk of secondary electrons emitted from solid targets [23]. Some of the experimental components used in the current setup had been developed at the Pacific Northwest Laboratories and utilized for electron emission studies of proton impact on C and Cu foils with or without cryogenically condensed gases [23, 24]. These components were incorporated into the ECU Accelerator Laboratory and

improved over the past ~20 years for further ion-induced electron emission studies using metal foils and gas condensates [15, 59, 87, 88, 96]. However, the range of proton projectile energies with Au and ASW targets had been limited to 2 MeV (and 6 MeV during a brief relocation of the experiment to the Kansas State University's James R. Macdonald Laboratory [59]) and C ions have not been studied until now.

While performing system tests and calibrations after the renovation of the ECU Accelerator Laboratory, the decades-old and unreliable 2 MHz beam "chopper" reached the end of its lifespan and was replaced with compact, custom-made semiconductor electronics. The Beam Pulser, as it's referred to, was a modernization that required several adjustments, reconfigurations, and system tests to maximize timing resolution and minimize signal noise. In addition, several system tests of the TOF detector and its associated electronics were performed prior to data collection. The process of "freeze thawing" the water to be deposited on the Au foil, in order to remove residual absorbed gasses, was also improved. The overall accomplishment of the preliminary modifications was a far more reliable data collection system, integrated with various computer software programs for more efficient data handling and processing.

3.2: Ion Source, Accelerator, and Beamline System

To generate an ion beam in the energy range of several MeV requires several stages of acceleration, steering, focusing, and collimation in a beamline evacuated by several turbo-molecular pumps to a pressure < 1 μTorr, as measured by several ionization gauges. The general layout of the accelerator beamline system is shown in Fig. 3.1. The whole process begins with the production of negative ions with a Cs-sputter ion source. A General Ionex Corporation®

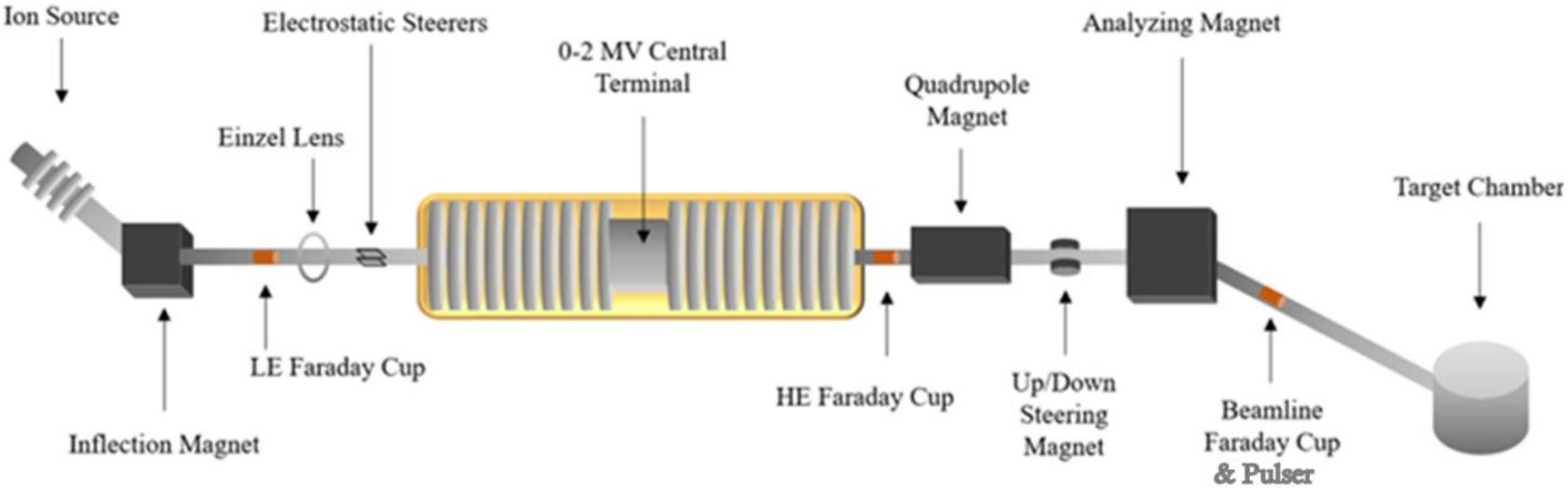

FIG. 3.1. Schematic of the ion source, low-energy beamline, accelerator, high-energy beamline, and target chamber beamline. Some steering and focusing equipment is shown, along with the UHV target chamber and beam Pulser.

model 860A ion source was used to produce both H^- and C^- beams. This negative ion source is highly prolific, generating ions for almost all elements except the noble gasses [61]. Beam currents vary by element but can exceed several hundred μA with this high intensity source, as described in the literature by Middleton [61-63]. To produce H^- and C^- ions, a target cathode of tightly packed TiH_2 or high-density graphite powder was used, respectively. Cesium was vaporized, ionized, and accelerated by approximately 2 kV toward the target cathode, where H^- and C^- ions were sputtered and accelerated away from the cathode by a combined 6 kV potential. An Einzel lens, which uses a shaped electric field to focus the beam, ensured a tight negative ion beam entered the subsequent 30 kV linear accelerator of approximately 70 cm length. The resulting 36 keV beam was then vertically steered by a magnetic field and momentum selected by a 25° inflection magnet in the low-energy portion of the accelerator beamline.

Before entering the Pelletron accelerator, the low-energy beam was shaped by grounded planar collimators and a second Einzel lens. In this region, the beam shape and intensity were monitored by a fluorescent crystal and Faraday cup, each able to be positioned in or out of the beam path. Additional vertical and transverse steering was performed by electrostatic plates before the negative ion beam entered the 2-MV tandem NEC® 6SDH-2 Pelletron model 2AA072310 accelerator.

The Pelletron accelerator charges a central high-voltage terminal with chains of alternating metallic and insulating links, as described in the literature [28, 70, 102]. The accelerating column was electrically insulated with dry SF_6 gas at 80 psi. An electric potential gradient was established along the 2-m portion from the grounded low-energy end to the central terminal, to accelerate the negative ions up to a maximum energy of 2 MeV. Here, N_2 stripper gas removed 2 or more electrons from the negative ions. The resulting positive ions were then

accelerated away from the central terminal to the grounded high-energy end of the accelerator, another 2 meters downstream, gaining up to 2 MeV of additional energy per elementary charge. Therefore, H^+ beams up to 4 MeV and C^{6+} beams up to 14 MeV were theoretically possible. However, it was found that the most reliable charge state of C ions for consistently high beam currents, over the full range of terminal voltages, was C^{2+}. Higher beam currents were needed to maintain reasonable data collection times. At this charge state, a maximum energy of 6 MeV was allowed for C ions, although higher energies and charge states can be obtained at reduced beam currents.

A transmission rate, between the low-energy and high-energy ends of the accelerator, of up to 80% was observed for H^- to H^+ and C^- to all measurable C^{q+}. This was determined by the beam current measured in the second Faraday cup located in the high-energy region. After the high-energy Faraday cup, a duplet of magnetic quadrupoles focused the beam and another magnetic field steered the beam vertically. An analyzing magnet, also called a switching magnet, was then used to momentum select the positively charged beam and deflect it 15° toward the target chamber. This ensured that the beam entering the target chamber beamline was the desired mass and energy (and desired charge state for C^{q+}). Careful consideration was taken to accurately identify the necessary electric current in the switching magnet that correlated to a given ion beam species.

As the ion beam travelled down the target chamber beamline, its relative position within the beamline as well as its shape and size in both transverse directions were measured by an NEC® model BPM80 beam profile monitor. The beam current was then measured by a third Faraday cup. Next, the beam was collimated by a second set of planar collimators before entering a duplet of electrostatic plates comprising the “Pulser”. These Pulser plates were

located as far upstream from the target as possible, to allow maximum deflection of the beam while limiting the required voltage to less than 2000 V. The design and implementation of the Pulser will be discussed in further detail in the following section. The beam was then collimated by a third set of planar collimators, which allowed precise control of the beam current entering the target chamber. A fluorescent quartz crystal was positioned just prior to the entrance of the target chamber, and was moved into the beam path and monitored via closed-circuit television while steering and focusing the beam. In this fashion, a highly intense beam spot of up to 5 μA and roughly 1-3 mm diameter was achieved. The target chamber beamline was kept in the 100 nTorr range by a turbo-molecular pump, as measured by an ionization gauge. The target chamber was evacuated by an additional turbo-molecular pump, as well as a titanium-sublimation pump to achieve ultra-high vacuum (UHV) between 0.5-5 nTorr, which is necessary for maintaining a clean target surface over the time span needed for data collection. The UHV target chamber will be discussed further in section 3.4.

3.3: Beam Pulser

As mentioned previously, a pulsed beam is necessary for electron TOF energy analysis. By pulsing the beam at a regular interval, the time of impact of the projectile(s) with the target is known, allowing for the measurement of the emitted secondary electrons' TOF and thus velocity and energy. This was accomplished by electrostatic steering of the ion beam in an oscillating fashion in the vertical and horizontal directions, both transverse to the projectile velocity.

Initially, only a vertical, 1-dimensional pulsing of the beam was done with a single set of electrostatic plates. This created a fast (several ns), downward sweep of the beam followed by a slow (several hundred ns), upward return sweep. The rates for upward and downward sweeps

were dictated by the solid-state characteristics of the metal-oxide-semiconductor field-effect transistors (MOSFETs) controlling the beam Pulser, to be discussed below. After thorough testing of beam parameters, electron emission rates, and timing parameters it was determined that a 1-D beam pulsing would unnecessarily expose the target to projectile bombardment, during the slow, upward return sweep, when electron TOF data could not be measured. This "wasted" bombardment could have compromised the integrity of the Au foil or ASW surface and sputtered away deposited layers of ASW, effectively changing the target thickness during secondary electron emission measurements. Therefore, an alternative approach was employed using a second set of electrostatic plates (horizontal steerers) to pulse the beam in 2 dimensions.

A phase shift between the vertical and horizontal steerers created a counter-clockwise sweep of the beam in a "D" shape at 10 kHz, of which only a 2-4 nanosecond pulse of beam would be aligned with and able to enter the UHV target chamber once every 100 μs. Fig. 3.2 shows this "D" shape as visualized on the quartz crystal, which is 18 cm before the UHV target chamber and angled 45° relative to the beam direction, for both H^+ and C^{2+} beams. The beam was steered to position the middle of the vertical, left side of the "D" in line with the UHV target chamber entrance. This portion of the beam sweep is the fastest, giving the best timing resolution for projectile impact, as can be seen in Fig. 3.2 by the relative intensity of the fluorescence.

The Pulser deflection plates, located 2.73 m before the UHV chamber entrance, required voltage sufficient to vertically deflect the beam a distance more than twice the diameter of the beam spot at the chamber entrance. This was necessary to ensure beam was only allowed to enter the chamber and impact the target during the fast, downward sweep. The Pulser deflection plates have a length L_{pp} = 12.7 cm, along the projectile path, and are 2.54 cm wide for electric field uniformity. Given the known translational kinetic energy T of the projectile, its velocity v_p,

a)

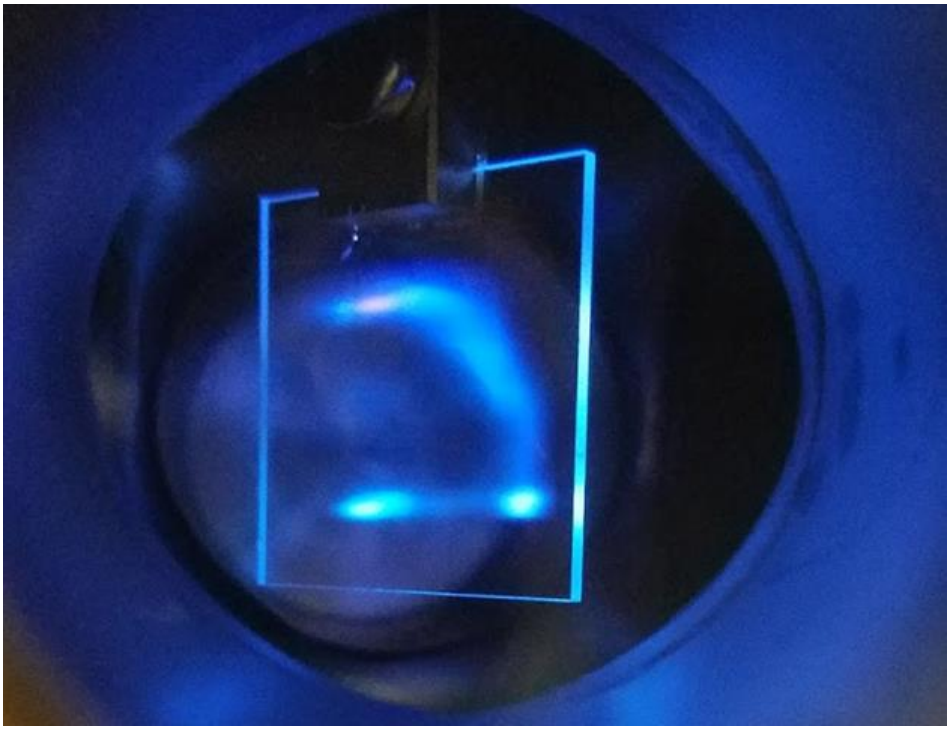

b)

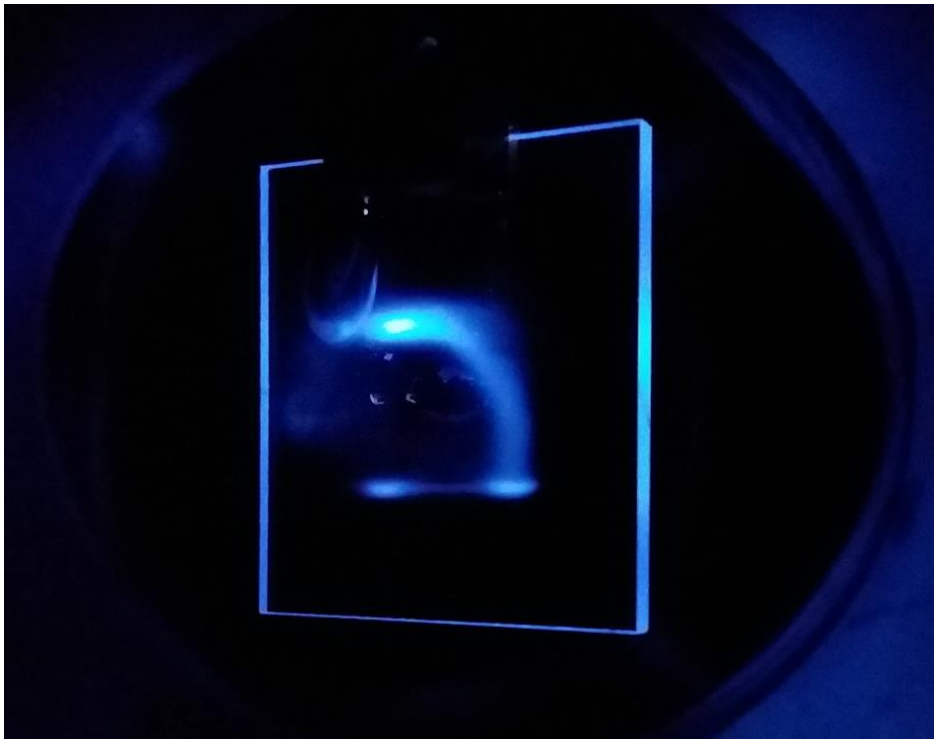

FIG. 3.2. The fluorescent quartz crystal is shown with a pulsed beam of 2 MeV H+ (a) and 6 MeV C^{2+} (b). The fast, downward sweep of the beam is barely visible. The crystal is 2.5 x 2.5 cm^2, angled 45° to both the ion beam and the view seen here.

in the horizontal projectile direction, can be calculated from

$$T = {}^{1}/_{2}\, m_p v_p^2 , \tag{3.1}$$

where m_p is the non-relativistic mass of the projectile. The time t_{pp} the projectile was within the electric field of the plates is, therefore

$$t_{pp} = \frac{L_{pp}}{v_z} = L_{pp}\sqrt{\frac{m}{2T}} . \tag{3.2}$$

The electrostatic force on a charged particle F_E in an electric field can be related to its acceleration a by Newton's Law

$$F_E = qE = q\frac{V_{pp}}{d_{pp}} = m_p a , \tag{3.3}$$

where V_{pp} is the potential difference across the Pulser plates, separated by a distance d_{pp} = 1.27 cm. The vertical velocity v_y of the projectile leaving the Pulser plates can be calculated from

$$v_y = at_{pp} , \tag{3.4}$$

where the initial vertical velocity is zero. Therefore, the vertical deflection y of the beam was found using the time t_{UHV} for the projectile to travel the distance L_{UHV} from the Pulser plates to the UHV chamber entrance by

$$y = v_y t_{UHV} = v_y \frac{L_z}{v_p} = \frac{qV_{pp}L_{pp}L_{UHV}}{2d_{pp}T} . \tag{3.5}$$

For a 4 MeV H^+, applying 2 kV to the Pulser plates resulted in a vertical deflection of 6.8 mm. This increased to 27 mm for a 1 MeV H^+. The deflection was 9.1 mm for a 6 MeV C^{2+}, increasing to 23 mm for a 2.4 MeV C^{2+}.

The voltage was applied to the vertical deflection plates and switched off at a frequency of 10 kHz and duty cycle of 5%. This was accomplished by LabView® software and a custom designed circuit utilizing power MOSFETs, built by William Holland in the ECU Physics Department. This Fast High-Voltage (HV) Switch circuit, as diagrammed in Fig 3.3, was driven by a square input pulse of 5 V. The frequency and on-time of the input pulse was controlled by software from 1-15 kHz and 1-10% duty-cycle, and was generated by a National Instruments® (NI) model BNC-2110 interface board. It was split to simultaneously trigger the Fast HV Switch of the Pulser circuitry and serve as a delayed start signal for the TOF system, to be discussed in a later section. A block diagram of the signal propagation can be seen in Fig. 3.4.

Initially, RG-58 coaxial cable was used, but the capacitance of the cables and impedance mismatch between the cables and the Fast HV Switch resulted in reflections of the input pulse and inconsistent timing. Extensive investigation of coaxial cable lengths, higher impedance coaxial cables, alternate positioning of the "tee" to split the signal, and various cable terminations led to the conclusion that coaxial cable could not be used. An alternate approach using "twisted pair" cables was investigated, and eliminated the reflection in the input signal that caused the power MOSFETs in the Fast HV Switch to turn off during the on-cycle of the output. The location of the input signal "tee" and the lengths of the cables were again investigated until a reliable, clean output was obtained.

The Fast HV Switch was comprised of 2 out of phase circuits, each powered by a separate Ortec® model 556 High-Voltage Power Supply. As labeled in Fig 3.3, the switch for "Plate 2" powered the Pulser plate responsible for the fast, vertical sweep of the beam, while the switch for "Plate 1" powered the horizontal "push" of the beam. The "push" was necessary to keep the beam off alignment with the UHV chamber entrance during the slow return while the

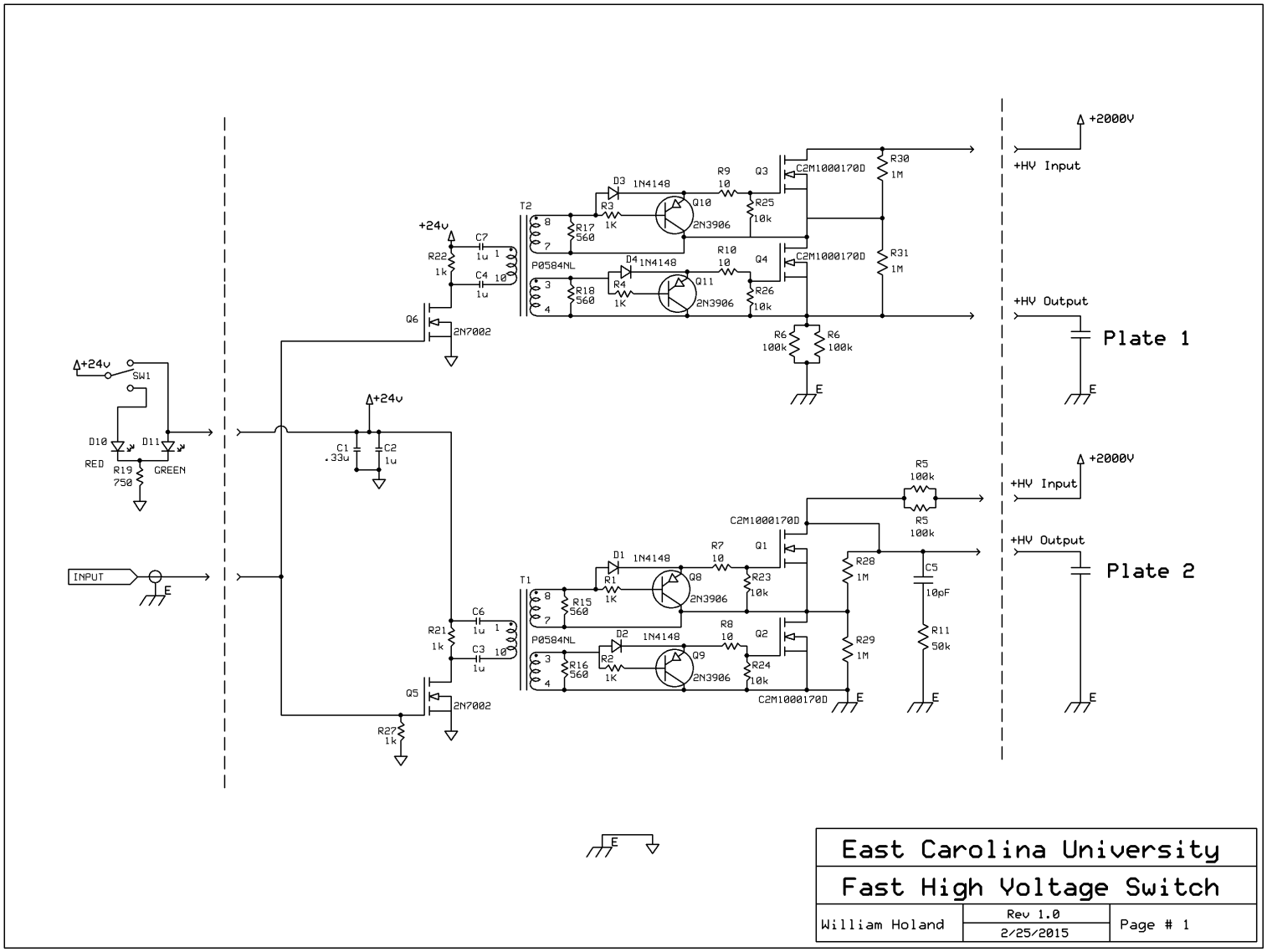

FIG. 3.3. A circuit diagram of the Fast HV Switch is shown. The upper "Plate 1" circuit was used to drive the horizontal "push", and the lower "Plate 2" circuit was responsible for powering the fast, vertical sweep of the beam.

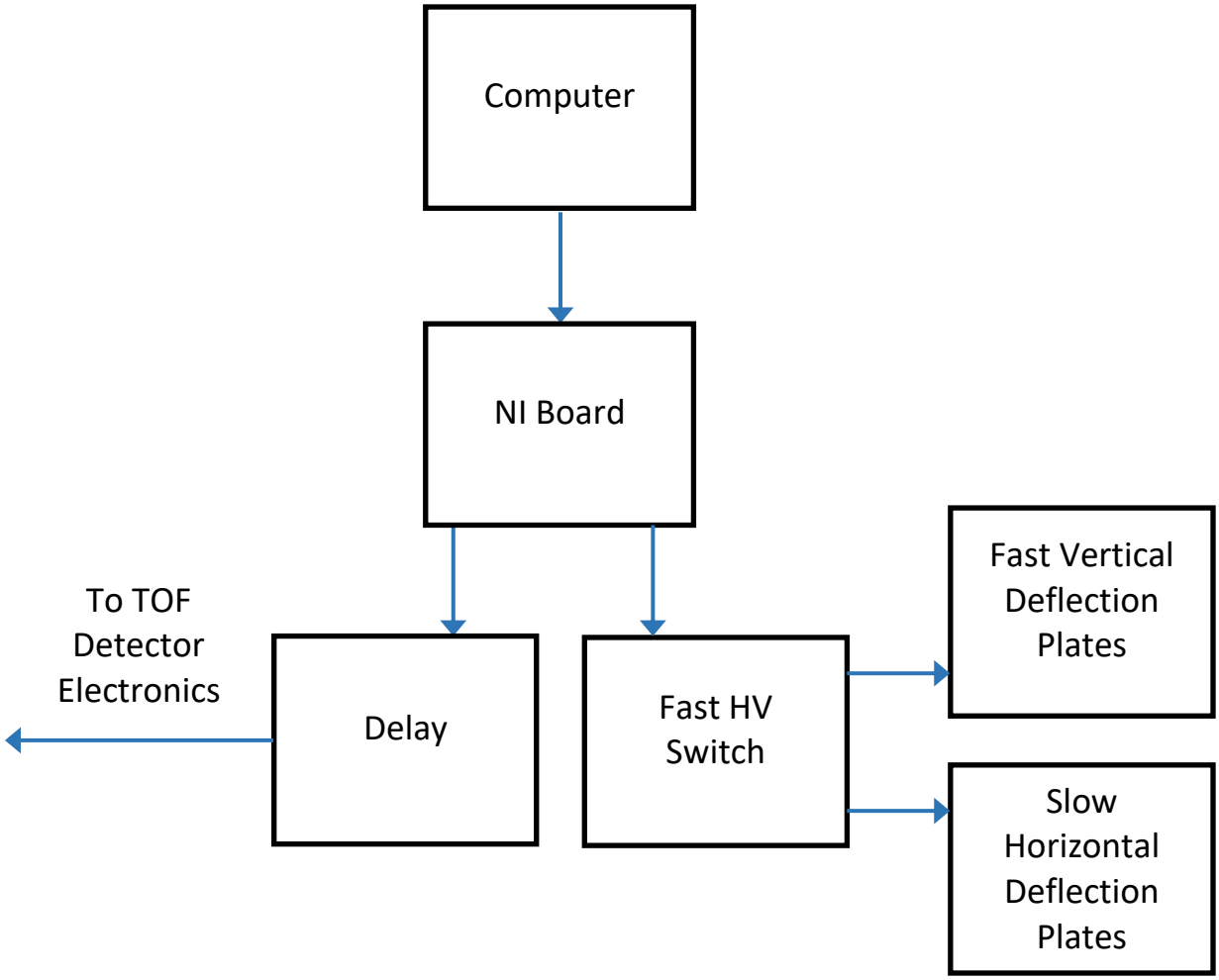

FIG. 3.4. Block diagram of the beam Pulser and related components.

vertical Pulser plate recharged. This ensured the target was only exposed to the fast pulse of the beam to reduce target sputtering and minimize the workload for the detectors.

3.4: UHV Target Chamber

The UHV target chamber used for the work presented here has been described by McLawhorn [59] and represented in other literature [15, 20, 21, 96]. Minor modifications have since been made, including an attempt at internalizing the TOF detector circuitry, to be described later. Multiple components were replaced, rewired, and/or adjusted in some manner, but the overall configuration of the UHV target chamber remained the same as shown in Fig. 3.5 and Fig. 3.6 by McLawhorn [59]. The base components of the chamber were the vacuum pumps and gauges, magnetic shielding and coils, ion-sputter guns, gas leak valve, residual gas analyzer (RGA), entrance beam collimator, and Faraday cup. Specialized components included a channel electron multiplier (CEM) "Rutherford detector", cryogenic target holder assembly, and microchannel plate (MCP) TOF detector with manipulator.

3.4.1: Base Components

The chamber was constructed from non-magnetic stainless steel, with a double-walled lining of high permeability μ-metal for magnetic shielding. The lid of the chamber was sealed with a 20" Viton® rubber O-ring, while all other joints utilized ConFlat® flanges sealed with high-purity copper gaskets. All interior surfaces were cleaned with isopropyl alcohol, and only materials suitable for UHV conditions were permitted inside the chamber.

A bake-out was performed over a 24-hour period after each exposure of the chamber to atmospheric conditions. By heating the chamber to 375 K, adsorbed and absorbed contaminants

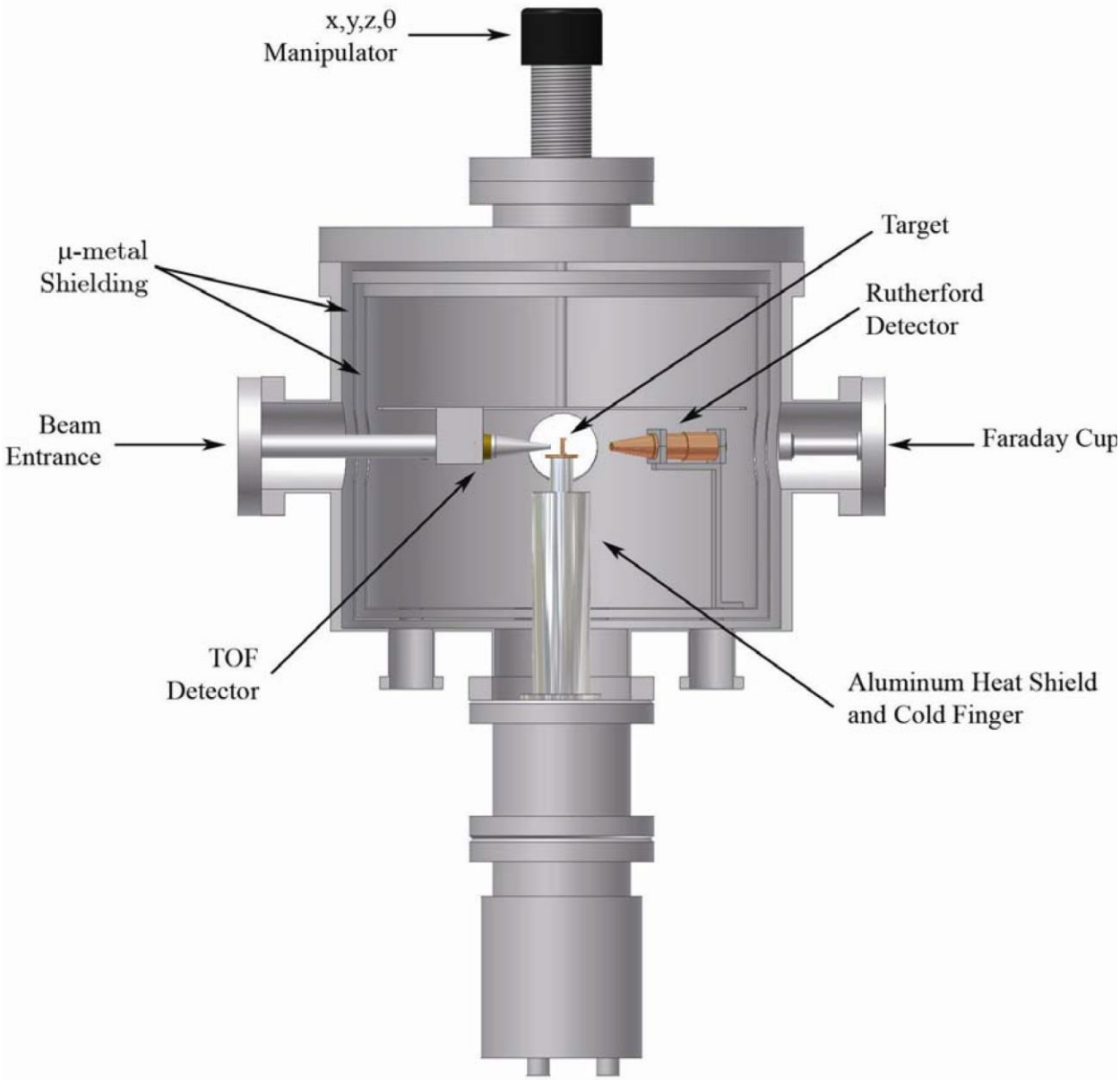

FIG. 3.5. A side-view, cut-away schematic of the UHV target chamber. Adapted from McLawhorn [59].

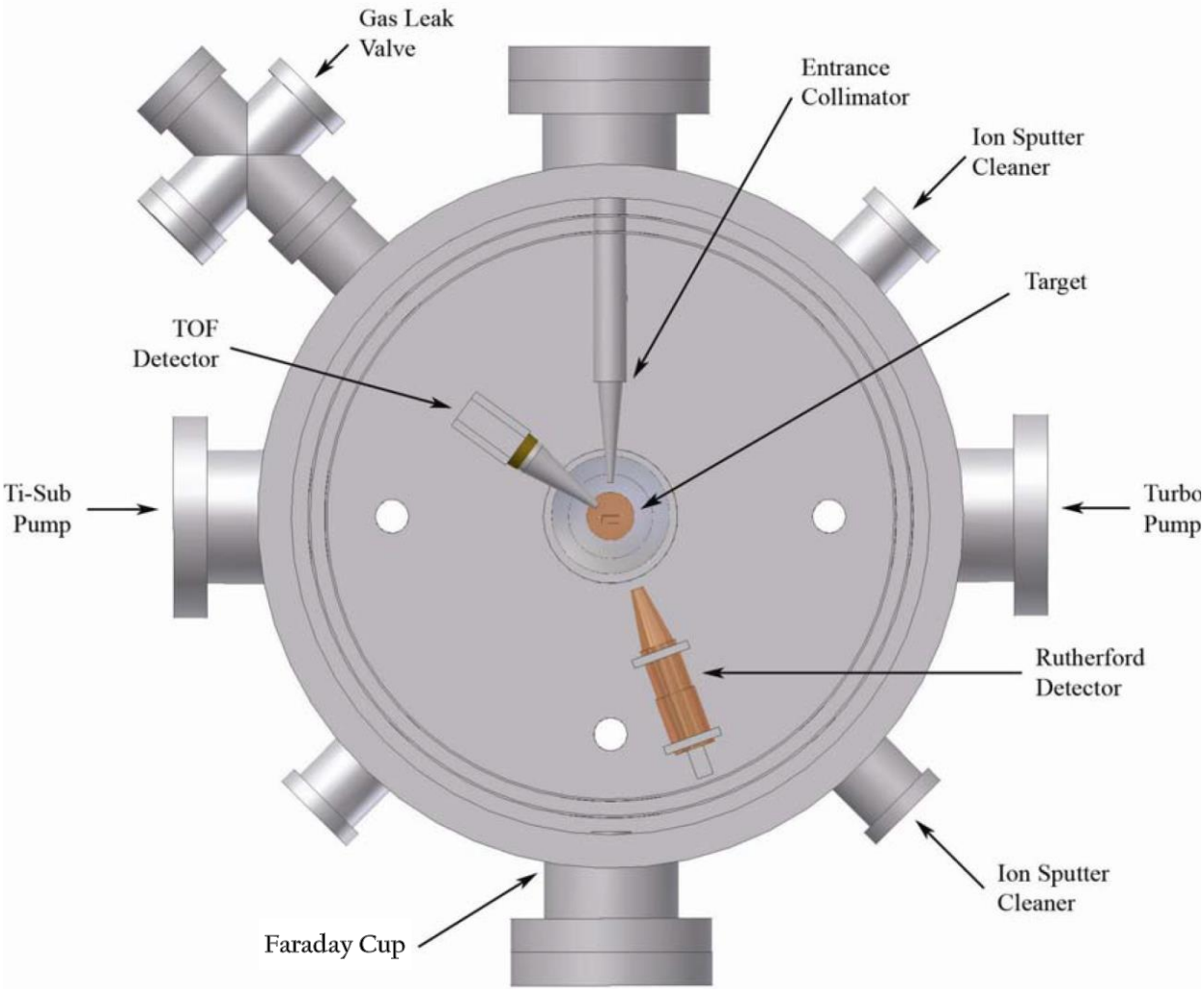

FIG. 3.6. A top-view schematic of the UHV target chamber, as seen with the lid removed. Adapted from McLawhorn [59].

were removed from the surfaces of the chamber, allowing a further reduction in pressure. This was accomplished with a system of resistive heating straps wrapped around the exterior of the chamber. A typical pressure between 0.5-5 nTorr was obtained after bake-out, with a turbo-molecular pump and titanium-sublimation pump. This pressure was measured with a Bayard-Alpert gauge located above the turbo-molecular pump as well as a nude ion gauge mounted on the bottom of the chamber itself.

In addition to the magnetic shielding inside the UHV target chamber, a pair of exterior Helmholtz coils were mounted to the support stand of the chamber to produce a vertical magnetic field. Using a Bartington® model Mag-01H Single Axis Fluxgate Magnetometer, the magnetic field at the center (target location) of the UHV chamber was measured for a wide range of currents in the Helmholtz coils. The μ-metal and chamber walls reduced the total magnetic field from 49 μT to 0.72 μT. This was reduced further to a total field of 0.61 μT by minimizing the vertical component of the magnetic field to less than 0.1 μT, with 0.3 A in the coils. At this minimal magnetic field, the deflection of low-energy electrons was insignificant. For instance, a 1 eV electron would have a radius of trajectory r = 1.8 m if travelling perpendicularly to a field of 0.6 μT, as given by

$$\mathrm{r} = \frac{\mathrm{mv}}{\mathrm{qB}\,sin\,\theta}, \tag{3.6}$$

where *m*, *v*, and *q* are the electron mass, velocity, and charge, respectively. *B* is the magnitude of the magnetic field and θ is the angle between *v* and *B*. For a total B-field of 0.61 μT with parallel components to the electron's velocity, the radius of trajectory would be even larger and not affect the detection of low-energy electrons over the short (~10 cm) distance of travel.

Protons and C ions entering the UHV target chamber were shaped by a grounded entrance collimator with a circular aperture of 1 mm diameter and measured by either a Faraday cup or CEM. The entrance collimator was telescoping, which allowed it to also serve as a guide for aligning the target foil with the ion beam. To ensure a consistently defined beam spot during data collection, it was positioned close (~2 cm) to the target. This limited the backward angular range of the rotatable TOF detector to 160°. A Faraday cup was positioned on the rear flange of the UHV chamber, past the target foil, to measure the beam current during alignment of the beam. However, during data collection when the Pulser was operating, the pulsed-beam current was < 1 pA, too low to be accurately measured in the Faraday cup. To account for this, relative beam current was measured from Rutherford scattered protons and C ions, to be discussed in the next section.

The target foil was held in place by a target assembly, positioned at the center of the UHV chamber and mounted on a cold-finger. The cold-finger and target assembly were cryogenically cooled with a Leybold® model RW3 closed-cycle helium compressor when needed. At this temperature, water vapor introduced to the chamber via the gas leak valve would condense as amorphous solid water (ASW) on the target foil. The "background dosing" technique was used to measure the thickness of the ASW condensation. In this technique, < 1 μTorr of vapor is introduced into the chamber, establishing a diffuse distribution where molecular interaction with the target occurs isotropically. To measure the thickness of the ASW condensate required an accurate measurement of the vacuum pressure as well as mass spectrometry of the UHV atmosphere. The nude ion gauge, which was positioned at the base of the UHV chamber, was used to monitor the background pressure during vapor deposition. It was considered to more accurately represent the chamber pressure than the Bayard-Alpert gauge,

positioned above the turbo-molecular pump hanging from the side of the chamber. Mass spectrometry was accomplished with an Ametek® model Dycor LC residual gas analyzer, also mounted to the base of the UHV target chamber. The background dosing technique will be discussed further in section 3.6.

Two Omicron® model ISE 10 sputter ion sources, also referred to as sputter guns, were mounted at 45° and 135° relative to the projectile velocity. This allowed cleaning of both the forward and backward surfaces of the target foil, using 5 keV neon ions. Neon was chosen for its extremely low melting and boiling points, both below 28 K, to allow sputter cleaning when the target was cryogenically cooled.

3.4.2: Rutherford Detector

A Dr. Sjuts Optotechnik® model KBL 10RS channel electron multiplier, referred to as the Rutherford detector, was positioned 20° from the beam. A voltage difference from entrance cone to collecting anode of 2425 V was applied. This voltage was found to produce a maximum count rate in the CEM without approaching its rated limits. Instead of grounding the cone of the CEM to allow detection of both positive and negative ions, a -1800 V bias was applied, as seen in Fig. 3.7 (a). In this manner, the vast majority of secondary electrons would not be detected, and a more accurate measurement of scattered protons and C ions could be made. The full 2425 V was not applied directly to the anode because the UHV-compatible wiring used for all HV connections in the UHV chamber was limited to 2000 V, due to the Kapton coating insulation on the copper wire.

The +HV cone bias needed to be shielded by a grounded copper enclosure to minimize the electric field around the target, as seen in Fig. 3.7 (b), adapted from McLawhorn [59]. The

a)

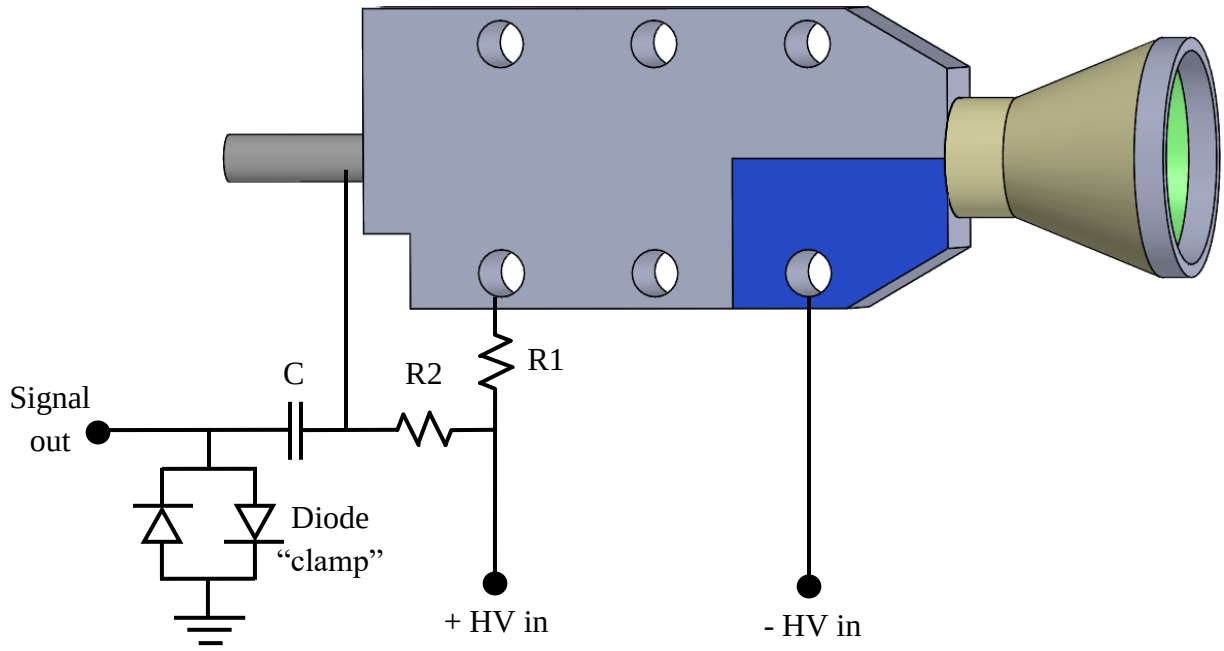

b)

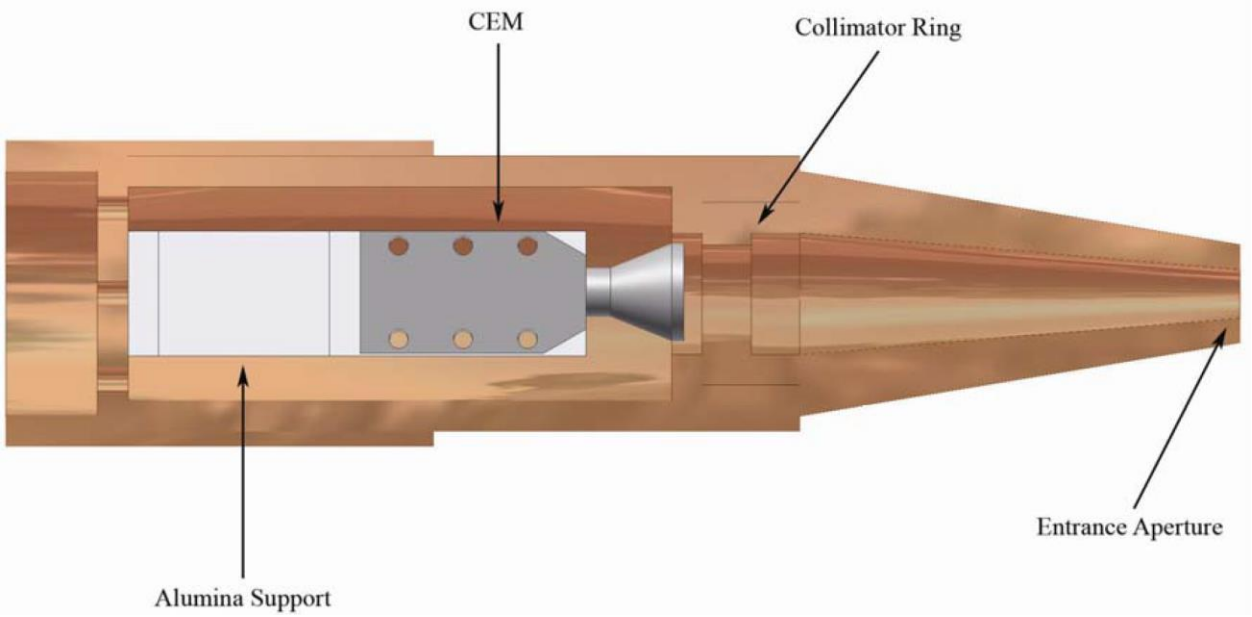

FIG. 3.7. A schematic of the CEM and wiring is shown (a), along with a cut-away view of the CEM mounted in the copper enclosure (b). The lower diagram (b) was adapted from McLawhorn [59].

entrance aperture was 5 mm in diameter, and its distance to the target was roughly 63 mm. However, for the purpose of comparing the scattered projectile counts from one data set to the next, the solid angle subtended by the detector was irrelevant. Also, the detector efficiency was not needed. The CEM was replaced before data collection began, and the same voltage biases were applied to the cone and anode for all data set, allowing direct comparisons to be made.

3.4.3: Cryogenic Target Holder Assembly

The target support and its base were constructed from copper for superior thermal and electrical conductivity. The base was surrounded by a ceramic sleeve, as seen in Fig. 3.8, adapted from McLawhorn [59]. This sleeve was interlaced with high purity tungsten wire to provide "flash" heating of the target holder assembly via an external power supply. In this manner, large quantities of condensed gasses and contaminants on the target foil surface could be removed relatively quickly, when sputter cleaning would be inefficient, without significantly raising the temperature of the entire cold-finger assembly. The flash heater was also used during the UHV chamber bake-out.

The temperatures of the target assembly and cold-finger base were monitored by two type-K thermocouples, designated as "A" and "B" in Fig. 3.8, and a Lakeshore® model 330 temperature controller. Typically, without the He-compressor running, both the target assembly and cold-finger base temperatures would remain stable at 289-291 K. With the He-compressor running for 2 hours or more, the target assembly temperature was typically 35-45 K, slightly warmer than the base of the cold-finger, as expected. A heater in the base of the cold-finger was found to be unnecessary, and wasn't used.

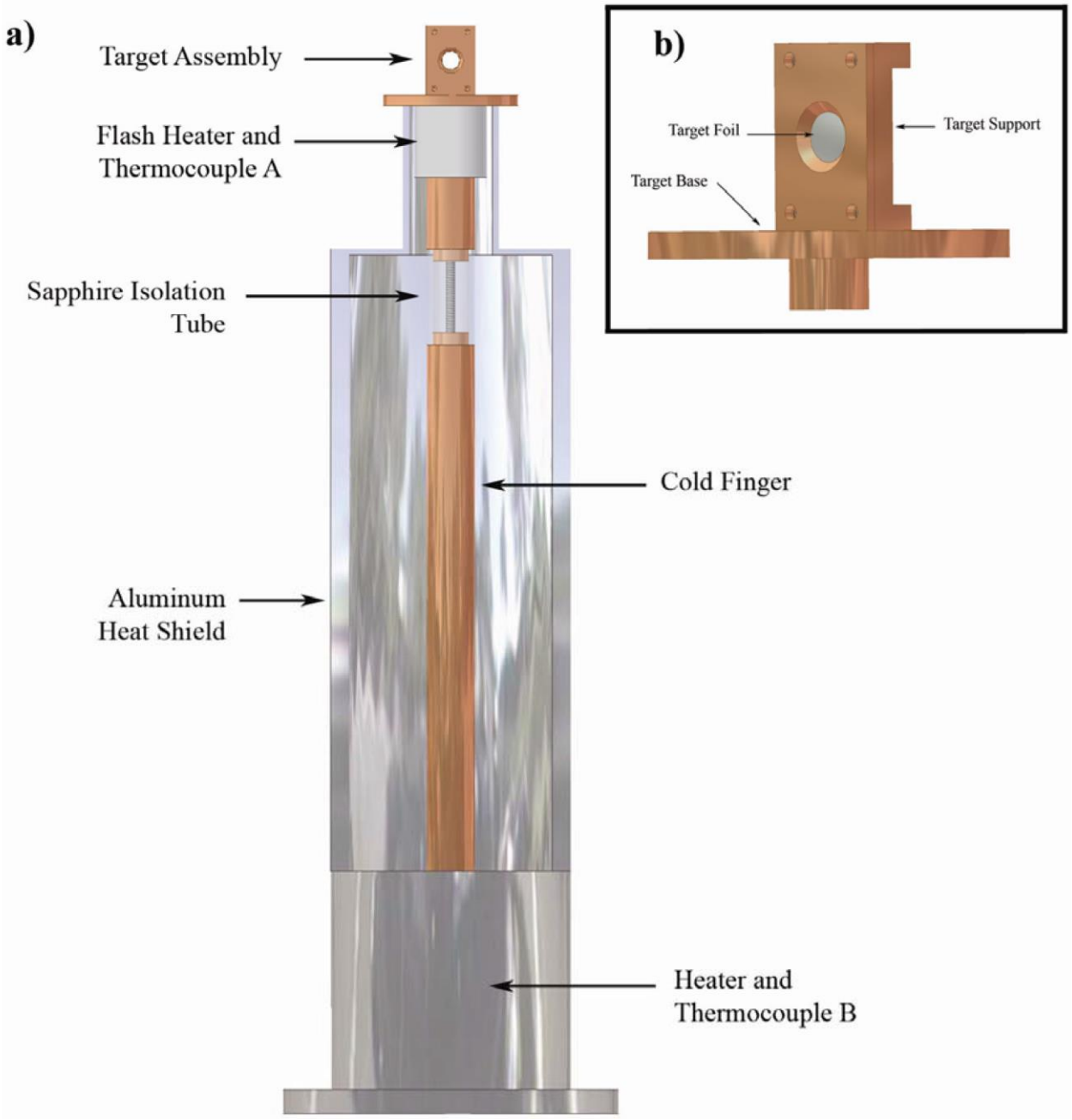

FIG. 3.8. A schematic of the cold finger assembly (a) surrounded by an aluminum heat shield, and a close-up view of the electrically isolated target holder assembly (b). Adapted from McLawhorn [59].

To electrically isolate the target assembly from the cold-finger and the UHV chamber, a sapphire tube was positioned between the target base and the cold-finger. Sapphire was chosen for its thermal conductivity, to keep the target assembly in good thermal contact with the cold-finger. The screw connecting the target base to the cold-finger was electrically isolated by an alumina washer. A wire connected to the target assembly, as well as both thermocouple wires and the flash heater wiring, exited the UHV chamber via a feed-through on the bottom flange. These wires were shielded behind an aluminum heat shield to prevent stray electric fields from interfering with data collection and to provide a thermal barrier for the cold-finger. The target assembly wiring allowed for external control of the target potential, to electrically ground or bias the target, if needed.

3.4.4: Time-of-Flight Detector

A cut-away diagram of the translatable, rotatable TOF detector, positioned next to the target assembly, along with a wiring diagram are shown in Fig. 3.9 (a) and (b), adapted from McLawhorn [59]. The TOF detector's main components were the entrance cones and collimators, grids, microchannel plates (MCPs), and anode. This detector was used for the detection of secondary electrons emitted from the target in the forward and backward directions, i.e. θ = 10-160°, and projectile ions that traversed the target without scattering, i.e. θ = 0°. Both types of measurements were correlated to the Pulser input signal for TOF calculations.

Charged particles entering the TOF detector were first collimated by a non-defining entrance aperture of 3.2 mm diameter at the tip of the detector cone. A scattered electron collimator was positioned inside the detector cone, with a second non-defining aperture of 4.2 mm diameter. Behind both entrance collimators was a defining rectangular collimator of 9.1 x

a)

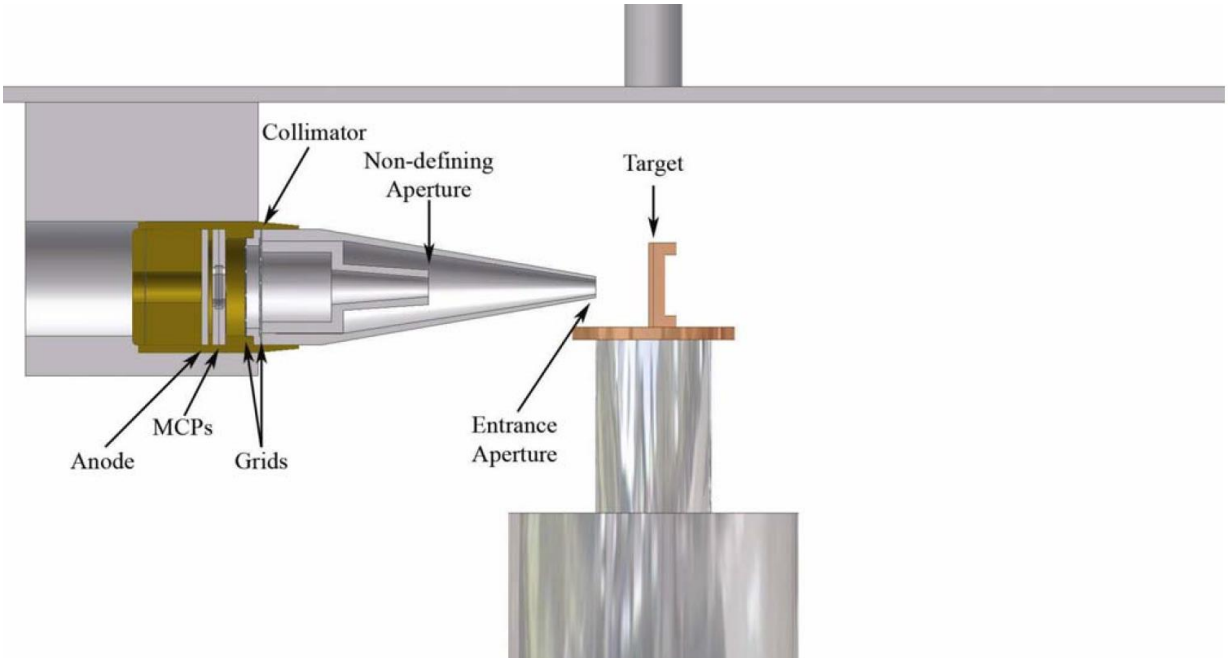

b)

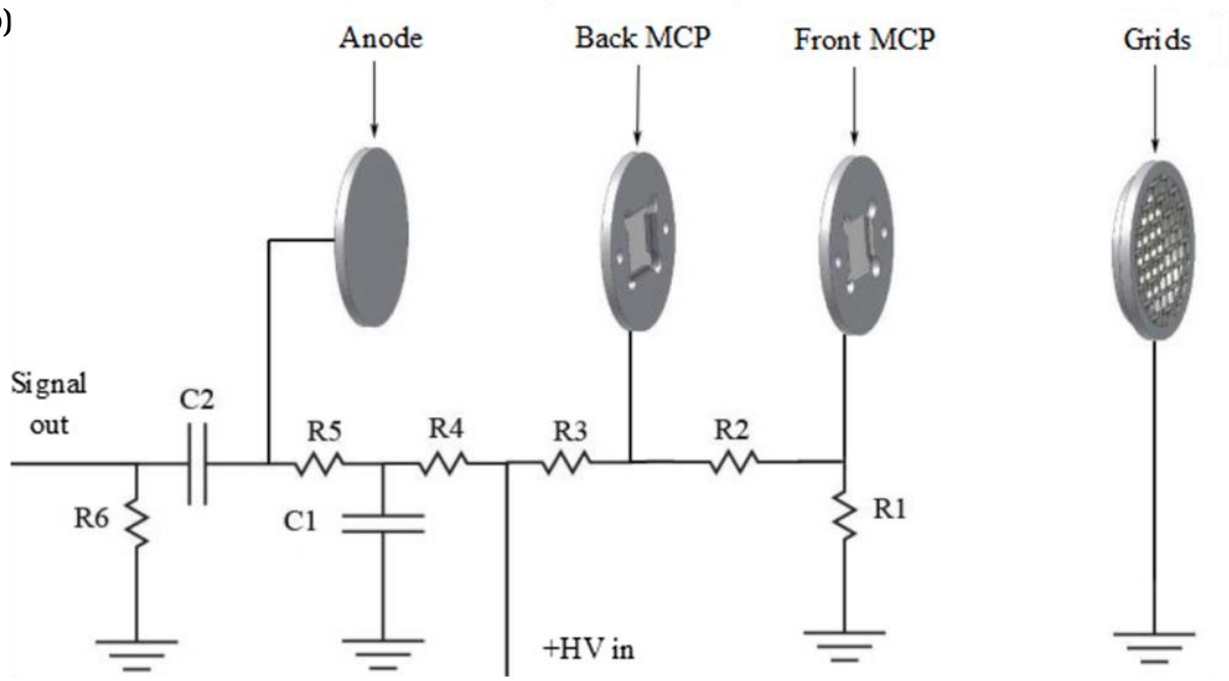

FIG. 3.9. A cut-away view of the TOF detector is shown (a) positioned at θ = 0° from the target assembly. The wiring diagram in (b) is shown along with an exploded view of the main components of the TOF detector. Adapted from McLawhorn [59].

3.1 mm^2 area. All three collimators were held at ground potential. The distance from target to rectangular collimator was 87.5 mm, defining a solid angle of 2.9×10^{-4} sr.

MCPs are used extensively for charged particle and energetic photon detection, and their properties and performance characteristics have been described in the literature [29, 110]. Typically, a gain of $10^3 - 10^5$ is expected per MCP, with the upper limit only attainable in high-vacuum conditions of pressure < 1 μTorr [110], which were easily met in this experiment. Two impedance-matched MCPs were used in a Chevron arrangement. The front MCP was biased with 52 V to improve the detection efficiency of low-energy electrons. The acceleration region this bias produced was minimal in length compared to the total pathlength of the emitted secondary electrons. The grids shown in Fig. 3.9 were held at ground potential and positioned 1.1 mm before the front MCP. The total distance from the target to the front MCP was 94.0 mm, of which 92.9 mm was in a field-free region. The total distance was measured each time modifications or adjustments to the TOF detector were made, to ensure an accurate electron or projectile TOF could be calculated.

The total bias applied to both MCPs was 1848 V. This was accomplished by a single +HV input of 1925 V and a series of resistors, as diagrammed in Fig. 3.9 (b). The +HV input was limited to 2000 V by the Kapton-coated wiring used for UHV applications. To determine the appropriate bias to apply, a series of investigations were made to optimize the output from the TOF detector. This was done by varying the signal gain and discrimination level, to be discussed in the next section. It was found that a range of +HV inputs of 1875 – 1975 V maximized the signal-to-noise ratio, and the median value of 1925 V was used.

The electrical components shown in Fig. 3.9 (b) were located outside the UHV chamber. Therefore, a total of ten coaxial connections were required between HV cables, voltage divider electrical boxes, and chamber feed-throughs. In an attempt to simplify and upgrade the configuration, UHV compatible resistors and capacitors were purchased to make almost all connections permanent and located inside the UHV chamber. This would reduce the number of connections to only two. An added benefit of this upgrade, due to the sensitive nature of electron detection, would be the additional electric and magnetic shielding of the TOF detector circuitry provided by the UHV chamber. Several attempts were made to accomplish this circuitry move, but it was found that the signal-to-noise ratio wasn't significantly improved by the upgrade. Moreover, issues with maintaining the UHV pressure conditions arose, and further attempts at internalizing the TOF detector circuitry were abandoned.

The TOF detector was suspended from the lid of the UHV chamber, on a four-axis (x, y, z, θ) manipulator. This manipulator allowed for three-dimensional alignment of the TOF detector with the projectile interaction site of the target, via micrometer controlled translations in the projectile direction z, the vertical direction y, and the transverse horizontal direction x. This alignment was done by maximizing the count rate in the TOF detector at several angles, as well as comparing electron emission spectra for various x, y, z settings. Once alignment was obtained, the detector was revolved around the target with the angular θ manipulator. The angular precision obtained with the manipulator was ±1°. The θ manipulator was capable of 360° rotation, but this full-rotation was limited by several components in the UHV chamber. This included the Rutherford scattered projectile detector in the forward direction and the target chamber entrance collimator in the backward direction.

3.5: Data Acquisition and Analysis

3.5.1: Electronics

The system required to perform all the tasks necessary for secondary electron emission measurements is complex, as can be seen in Fig. 3.10. Counts from the TOF detector were recorded in correlation to the projectile impact, as determined by the Pulser timing, and related to counts from the Rutherford detector. This all happened while the UHV chamber pressure was monitored, with intermittent analysis of the partial pressures of constituent gasses. To accomplish this, several stand-alone electronics and Nuclear Instrument Module (NIM) electronics were used.

The TOF signal was first amplified inline by an Ortec® model VT120A fast timing preamplifier (PreAmp). This PreAmp signal was then amplified by an Ortec® model 474 timing filter amplifier (TFA) and relayed to a Canberra® model 2126 constant fraction discriminator (CFD). The TFA gain was set to the highest level without exceeding the CFD limitations. The CFD threshold was set to a level limiting the "dark" counts from the MCPs or other electrical noise that entered the detector system between the UHV feed-through connection and the TFA output. An acceptable rate of background counts was determined to be < 1 per second.

Significant time was spent trying to eliminate sources of background noise in order to avoid increasing the CFD threshold to a level that would discriminate low-energy electron signals from the TOF detector. For instance, the HV cables powering the Pulser deflection plates were discovered to act as a transmitter, so shielding was added. Additional shielding was applied to the electrical boxes housing the TOF detector circuitry. Also, grounding straps were added, and several other attempts were made to relocate NIM electronics, physically isolate

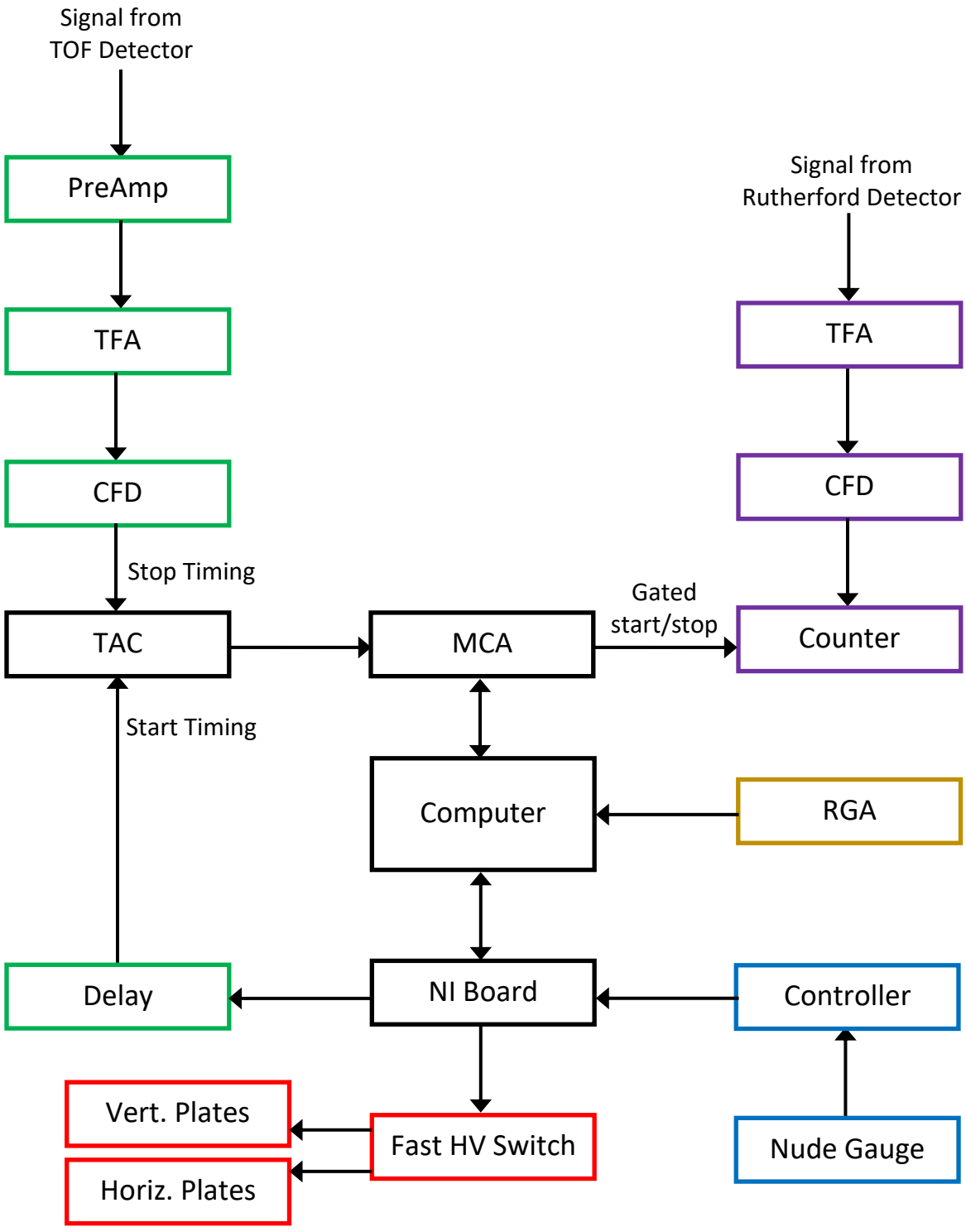

FIG. 3.10. Block diagram of the data acquisition system, including the Pulser components from Fig. 3.4, shown here partially in red (bottom left).

signal cables, optimize cable lengths, eliminate cables, add cable terminations, introduce inductive traps, or isolate beamline ground loops.

The CFD produced a fast, negative pulse that was sent to a Canberra® model 2145 time-to-amplitude converter (TAC). The TAC required a "start" and "stop" signal pulse. The delayed Pulser input pulse acted as the start signal, while the amplified, discriminated TOF detector pulse was the stop signal. The delay NIM converted the square +5 V Pulser input pulse into a fast, negative pulse. The length of delay was dependent on the velocity of the projectile and varied from 260-690 ns. The TAC was set to a range of 500 ns, such that stop signals that occurred after the start signal, but beyond this range, were ignored. This allowed enough time for an electron of energy < 0.2 eV to travel the distance of 94 mm from target to detector, as determined by equations 3.1 and 3.2. Based on the length of time between the start and stop signals, the TAC would output a square voltage pulse between 0-10 V. This output was relayed to the computer by a Canberra® model MultiportII multichannel analyzer (MCA). There, Canberra® Genie2000 software performed pulse-height analysis (PHA) by assigning each signal to one of 2048 digital channels.

Whenever PHA was initiated by the software, the computer, via the MCA, would remotely trigger an Ortec® model 874 quad counter/timer to count pulses it might be receiving. This gated start/stop of the counter was utilized to coordinate the counting of Rutherford detector pulses of scattered projectiles with the TOF detector counts of secondary electrons. First, the signal from the Rutherford detector was amplified and discriminated by a separate TFA and CFD combination. As with the final product of the TOF detector pulses, the Rutherford detector CFD produced a fast, negative pulse. The settings for the Rutherford detector TFA and CFD were chosen, as with the TOF detector electronics, to maximize the signal-to-noise ratio without

exceeding the limitations of the electronics. The scattered counts were necessary for normalization of the secondary electron spectra. So, after optimizing the settings, they were never adjusted to ensure compatibility of scattered counts from one data set to another.

3.5.2: Conversion to Electron Emission Yields

A raw data set, or run, consisted of a spectrum of counts from the PHA of the TAC output, i.e. the secondary electron channel distribution, and the scattered projectile counts from the Rutherford detector. In order to convert these data into doubly differential electron emission yields, several data processing steps were performed. First, each channel number from the channel distribution was correlated to an electron TOF. Then, the resulting electron TOF distribution was converted into an electron energy distribution via calculation of velocity from TOF and target-to-detector distance. Finally, incorporating the scattered projectile counts resulted in relative doubly differential electron emission yields. For target and projectile species/energy combinations that have published data for total electron emission yields (γ or γ_B) the relative yields were normalized to produce absolute yields. Otherwise, estimated absolute yields were produced from relevant published data.

The first step of converting channel number to electron TOF required calibration of the PHA. To accomplish the first requirement, an Ortec® model 462 time calibrator was used for the start and stop signals of the TAC. The time calibrator produces a start pulse, followed by a stop pulse at random multiples of a selectable period. This creates uniformly spaced pulses in the TAC, as observed in the PHA from the TAC. According to the product manual, the accuracy is ±0.005% of the total period. The resulting PHA distribution can be seen in Fig. 3.11, as a timing spectrum with 20 ns pulses. The average interval between pulses was 161.3 channels,

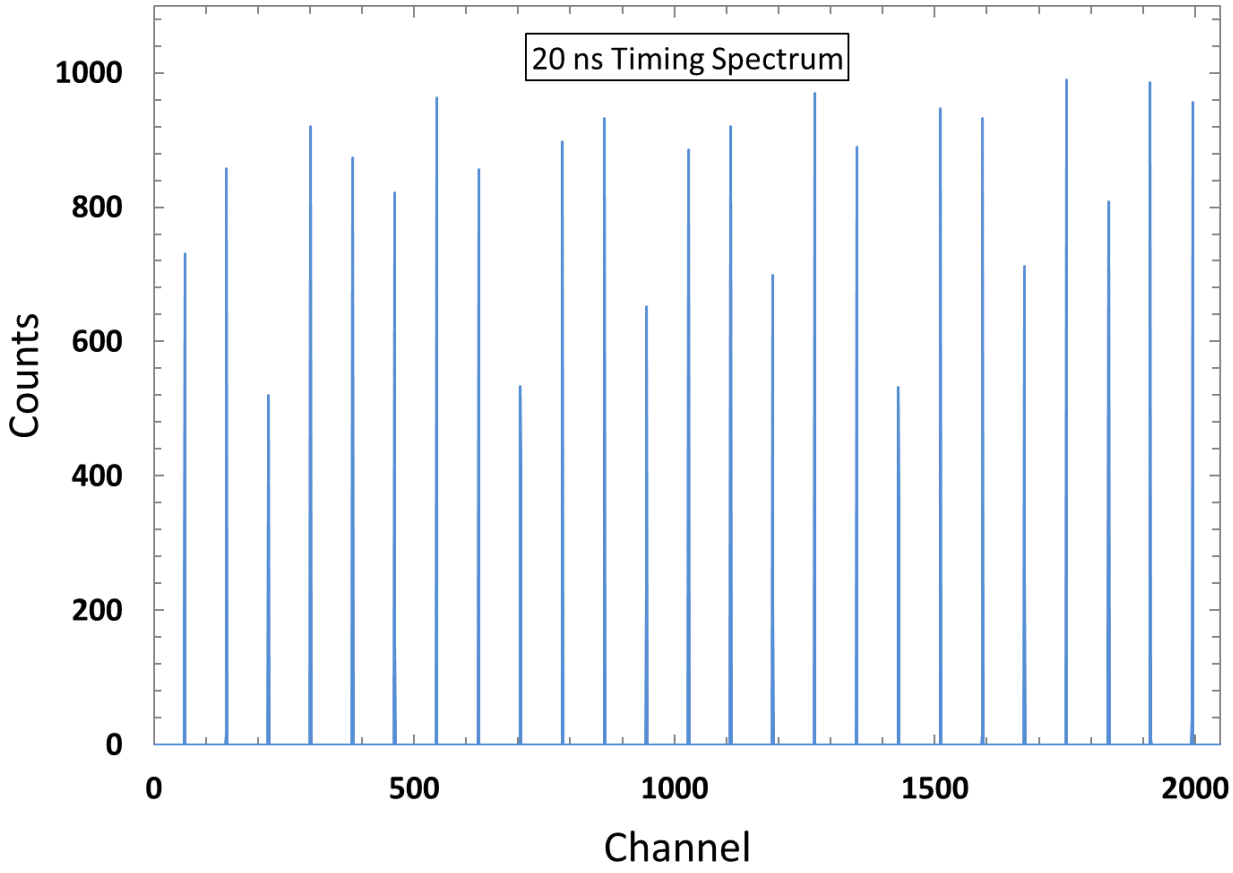

FIG. 3.11. Timing spectrum with 20 ns pulses generated by a time calibrator. The resulting peaks are 161.3 channels apart, on average, resulting in a timing factor Δ_t = 4.032 channels/ns.

resulting in a timing factor Δ_t = 4.032 channels/ns. This process was repeated with 10, 40, and 80 ns periods, all resulting in the same timing factor.

The second step in converting channel number to electron TOF was calculation of the channel corresponding to projectile impact with the target, or Ch_0 for t = 0 in the TOF method. This was accomplished by performing a PHA with the TOF detector positioned at 0°, to first determine the channel corresponding to projectile detection, after traversing the target. Typical spectra of 0° peaks from both protons and C ions are shown in Fig 3.12. The channel corresponding to the projectile peak location was designated Ch_p. The "0° runs" were measured with all electronics connected as shown in Fig 3.10. Additionally, all electronic settings used for electron emission measurements were also used for the 0° runs. Minor day-to-day variations in beam alignment from the ion source up to the UHV chamber would shift the 0° peak up or down several channels. This approximately ±1 ns fluctuation was not considered to be significant. However, to account for this, a 0° run was performed at the start of each day that data would be collected, and the Pulser delay was adjusted as needed.

Because some initial "entrance" kinetic energy is lost as the projectile traverses the gold foil's thickness of 1 μm, the final "exit" energy was determined from the Stopping and Range of Ions in Matter (SRIM) software package by Ziegler *et al*. [113]. This was needed to accurately determine the TOF for the projectile in the 0° runs. For instance, a 1.0 MeV H^+ would exit the Au target with 0.873 MeV energy, losing approximately 13% of its initial energy. Entrance and exit energies, as determined by SRIM, for the projectiles studied are listed in Table 3.1. The addition of ~100 ASW monolayers to the Au target contributed insignificantly to the projectile energy loss. It should be noted that when referring to the various proton and C-ion beams, the initial energy will be stated. Using the final exit energy, the projectile TOF t_p was calculated

a)

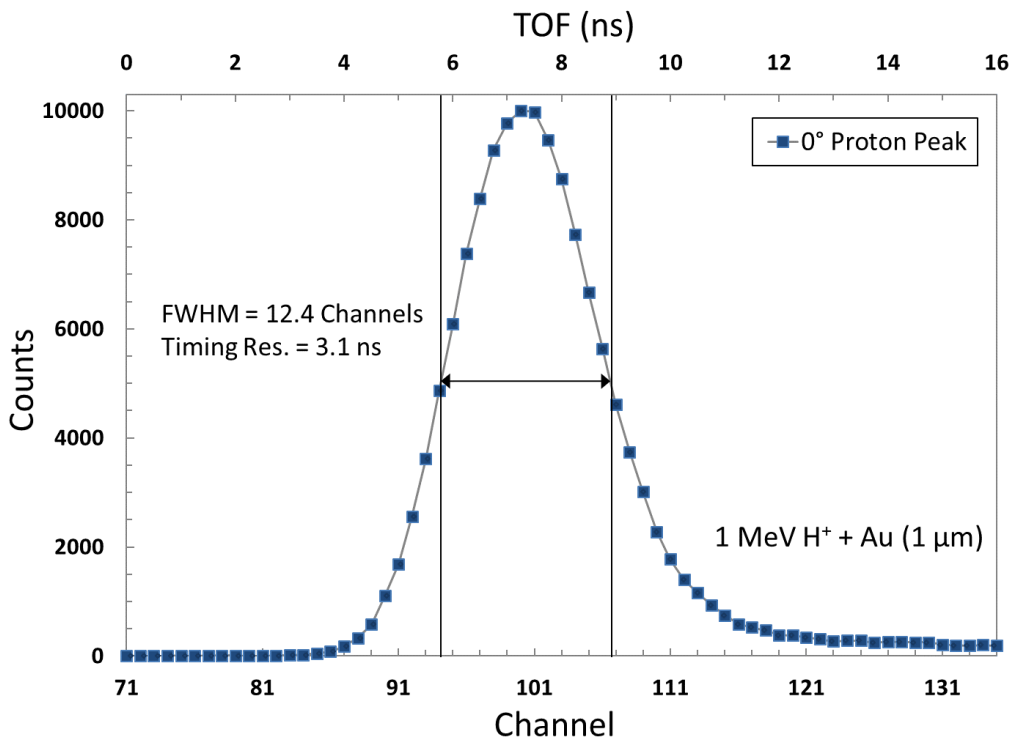

b)

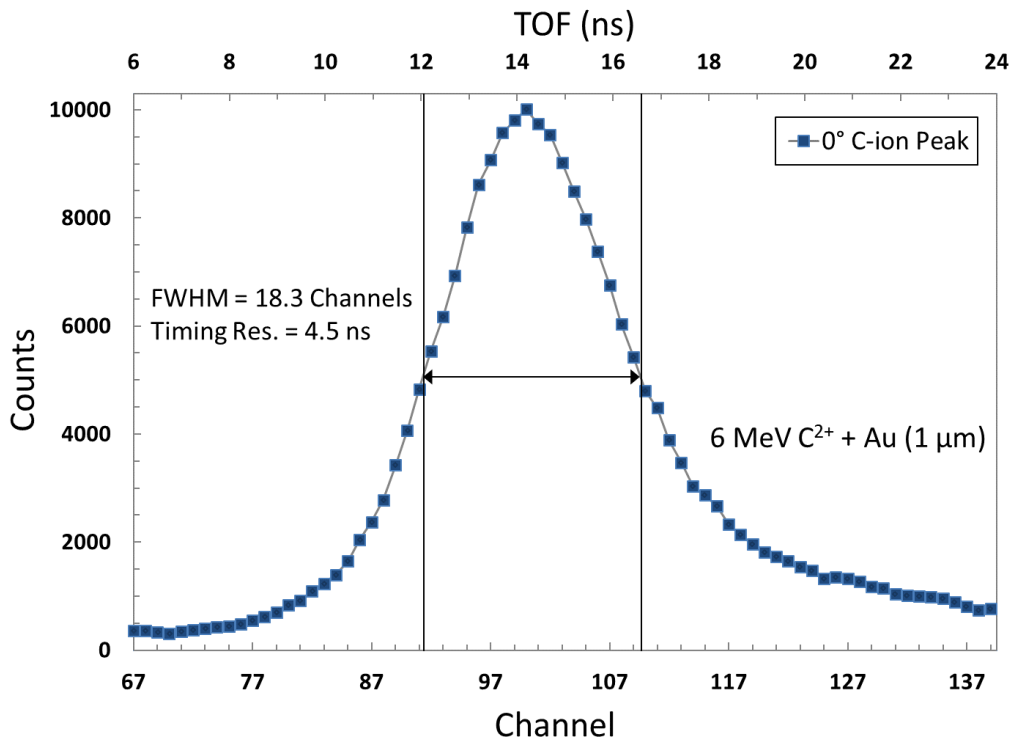

FIG. 3.12. Typical 0° peak channel spectra, shown with corresponding TOF, for 1 MeV H^+ (a) and 6 MeV C^{2+} (b). The timing resolution was determined by the FWHM of the 0° peak channel spectra, with the timing factor conversion Δ_t = 4.032 channels/ns.

from its velocity v_p by replacing the plate length L_{pp} with the target to TOF detector distance d = 94.0 mm in equations 3.1 and 3.2. Values for v_z and t_z are listed in Table 3.1. With the 0° peak channel Ch_p determined by the 0° runs, the timing factor Δ_t= 4.032 channels/ns, and the TOF of the projectile exiting the Au foil v_p, the channel Ch_0 corresponding to time of impact t = 0 is

$$\mathrm{Ch_0} = \mathrm{Ch_p} - \mathrm{t_p}\Delta_\mathrm{t}\,. \tag{3.7}$$

For instance, the projectile peaks for both spectra in Fig. 3.11 are located at Ch_p = 100, and the corresponding Ch_0 locations are 71 for the proton peak spectrum (a) and 43 for the C-ion peak spectrum (b).

Table 3.1. Initial and final energies of H^+ and C^{2+} projectiles traversing 1 μm of Au, and the corresponding percentage of energy loss, as determined by SRIM [113]. Also listed are projectile velocities and times in the 0° path from the target to the TOF detector.

Projectile	H^+			C^{2+}	
Initial Energy (MeV)	**1.00**	**2.00**	**4.00**	**2.40**	**6.00**
Final Energy (MeV) 1 μm Au exit	0.87	1.91	3.94	0.39	2.73
% Energy Loss	13%	4%	2%	84%	55%
Final v_p (m/s)	1.29E+07	1.91E+07	2.75E+07	2.51E+06	6.62E+06
t_p (ns)	7.27	4.91	3.42	37.49	14.19

The full width at half maximum (FWHM) of the 0° peak was used to describe the timing resolution of the data acquisition system. Values shown in Fig. 3.12 were typical, however a range of 2.5-5.0 ns was observed for protons. It should be noted the while there is a Gaussian shape to the 1 MeV proton peak in Fig 3.11 (a) and all other proton peaks recorded, the C-ion peak in Fig. 3.12 (b) is less Gaussian shaped and shows some range-straggling effects. This was especially true for 2.4 MeV C-ion peaks. The timing resolution observed in the proton peaks

was considered to more accurately represent the data acquisition system; therefore, the data collection timing resolution was ≤ 5 ns, even though some 6.0 MeV and 2.4 MeV C-ion peaks exhibited larger FWHM values.

The third and last step to convert channel number to electron TOF t_e was to simply scale all channels, from Ch_0 upward, using the timing factor as follows:

$$\mathrm{t_e} = \frac{\mathrm{Ch_t} - \mathrm{Ch_0}}{\Delta_\mathrm{t}}. \tag{3.8}$$

Ch_t in equation 3.8 is the channel that corresponds to the resulting electron TOF. Once the electron TOF scale was established, the electron energy ε followed from

$$\varepsilon = \frac{1}{2}\mathrm{m_e v_e^2} = \frac{1}{2}\mathrm{m_e}\left(\frac{\mathrm{d}}{\mathrm{t_e}}\right)^2, \tag{3.9}$$

where m_e is the non-relativistic mass of the electron and d is the target to TOF detector distance of 94.0 mm. From equation 3.9, the timing resolution of 5 ns equated to an electron energy resolution of 6.3% at 1 eV, decreasing to 20.4%, 49.4%, and 77.8% for 10 eV, 50 eV, and 100 eV, respectively.

Once the electron TOF and energy scales were established, the electron channel distribution, the number of secondary electron counts in each of the 2048 channels, could be converted to electron TOF and energy distributions. The electron TOF distribution $\gamma(t, \theta)$ is given by

$$\gamma(\mathrm{t}, \theta) = \frac{\mathrm{N_e}}{\mathrm{N_p}\xi \mathrm{G}\Omega\Delta_\mathrm{t}}, \tag{3.10}$$

where N_e is the number of electron counts in a given channel, N_p is the number of incident projectiles, ξ is the detector efficiency for electrons, G is the detector grids' transmission coefficient, and Ω is the solid angle subtended by the detector. The electron energy distribution $\gamma(\varepsilon, \theta)$, or doubly differential electron emission yield, is related to the electron TOF distribution by

$$\gamma(\varepsilon, \theta) = \left|\gamma(t, \theta)\left(\frac{dt_e}{d\varepsilon}\right)\right|, \tag{3.11}$$

where ε is given in equation 3.9. Combining equations 3.9-3.11, the electron energy distribution can be rewritten as

$$\gamma(\varepsilon, \theta) = \frac{N_e t_e^3}{N_p \xi G \Omega \Delta_t m_e d^2}. \tag{3.12}$$

Unfortunately, as mentioned earlier, the projectile beam current was too small, when the beam was pulsed, to be directly measured. Without direct measurement of the incident projectile current, the number of incident projectiles N_p could not be determined. So, the number of scattered projectiles counted by the Rutherford detector N_{sp} was used for making relative electron emission yield measurements. Therefore, the relative measurement didn't require knowledge of the detector efficiency, solid angle, or grid transmission coefficient, as these could all be accounted for by normalization of the relative yields to published values for total (backward) electron emission yields. Therefore, the relative doubly differential yields were calculated using

$$\gamma(\varepsilon, \theta)_{rel} = \frac{N_e t_e^3}{N_{sp} \Delta_t m_e d^2}. \tag{3.13}$$

The normalization was accomplished by numerical integration of the relative doubly differential yields over all electron energies ε and angles θ (90-180° for γ_B) to obtain relative total yields that were scaled to published values. Relative angular singly differential electron emission yields $\gamma(\theta)_{rel}$ are given by

$$\gamma(\theta)_{\mathrm{rel}} = \int_0^{\infty} \gamma(\varepsilon, \theta)_{\mathrm{rel}} \mathrm{d}\varepsilon \,, \tag{3.14}$$

and relative total yields γ_{rel} are given by

$$\gamma_{\mathrm{rel}} = \iint_0^{2\pi} \gamma(\theta)_{\mathrm{rel}} \, sin\,\theta \, \mathrm{d}\theta \mathrm{d}\phi = 2\pi \int_0^{\pi} \gamma(\theta)_{\mathrm{rel}} \, sin\,\theta \, \mathrm{d}\theta \,. \tag{3.15}$$

Published data for total electron emission yields were available for all proton energies with Au targets, but not ASW targets. Because the majority of the projectile pathlength in the ASW target was through the Au-foil substrate and Rutherford scattering scales with the target atomic number Z (79 for Au vs. ~7.8 for water), the normalization factor for Au scattered protons was also used for ASW. For C-ion projectiles, estimated normalizations were performed by comparing with total backward electron emission yields from bare C^{6+} ions of similar energy.

3.6: Target Preparation and Measurement Parameters

For all doubly differential electron emission yields, a 99.9% pure polycrystalline Au foil of thickness 1.0 μm was used. The Au foil was mounted in the target support of the target assembly after being cut to size. During bake-out of the UHV chamber, the flash heater surrounding the target assembly was used to heat the target to ~450 K, above the chamber bake-out temperature, to remove adsorbed gasses and limit condensation on the target after all heaters

were turned off. By the time the target and chamber cooled to an ambient temperature of ~290 K, however, residual gasses in the chamber would condense or adsorb to the target surface. This "dirt" as it was referred to, was known to affect the low-energy portion of the electron emission spectra, as seen in Fig. 3.13.

For both Au and ASW electron emission measurements, a sputter-cleaned Au foil was first prepared. The amount of cleaning required to remove adsorbed gasses depended on the length of time since a UHV system bake-out or previous target cleaning was performed. It was also dependent on the UHV chamber pressure, the partial pressures of the constituent gasses, and the target temperature. The total UHV chamber pressure was always <10 nTorr at the start of data collection and, under cryogenic target assembly conditions when the He compressor had been running for >2 hours (usually overnight), would fall to 0.2-1.0 nTorr. A typical cryogenic target temperature of ~40 K was obtained. The dirt that accumulated on the target surface was comprised of the residual gasses measured by the RGA. A typical RGA spectrum of the UHV chamber atmosphere is shown in Fig. 3.14. Water vapor and its H, H_2, or OH components were the dominant gasses present in the chamber along with nitrogen gas N_2.

Between 2-30 min of initial Ne sputter cleaning of the Au target, either at room temperature or after recent "flash heating", would be performed before data collection each day. After the target and cold-finger were under cryogenic conditions for an extended period, in preparation for ASW deposition, it was found that flash heating the target by temporarily raising its temperature to >350 K vastly reduced the needed sputtering time once the target cooled back down to 40 K. This was considered a better alternative to prolonged sputter cleaning, which could degrade the integrity of the Au-foil surface, of the cryogenically condensed contaminant

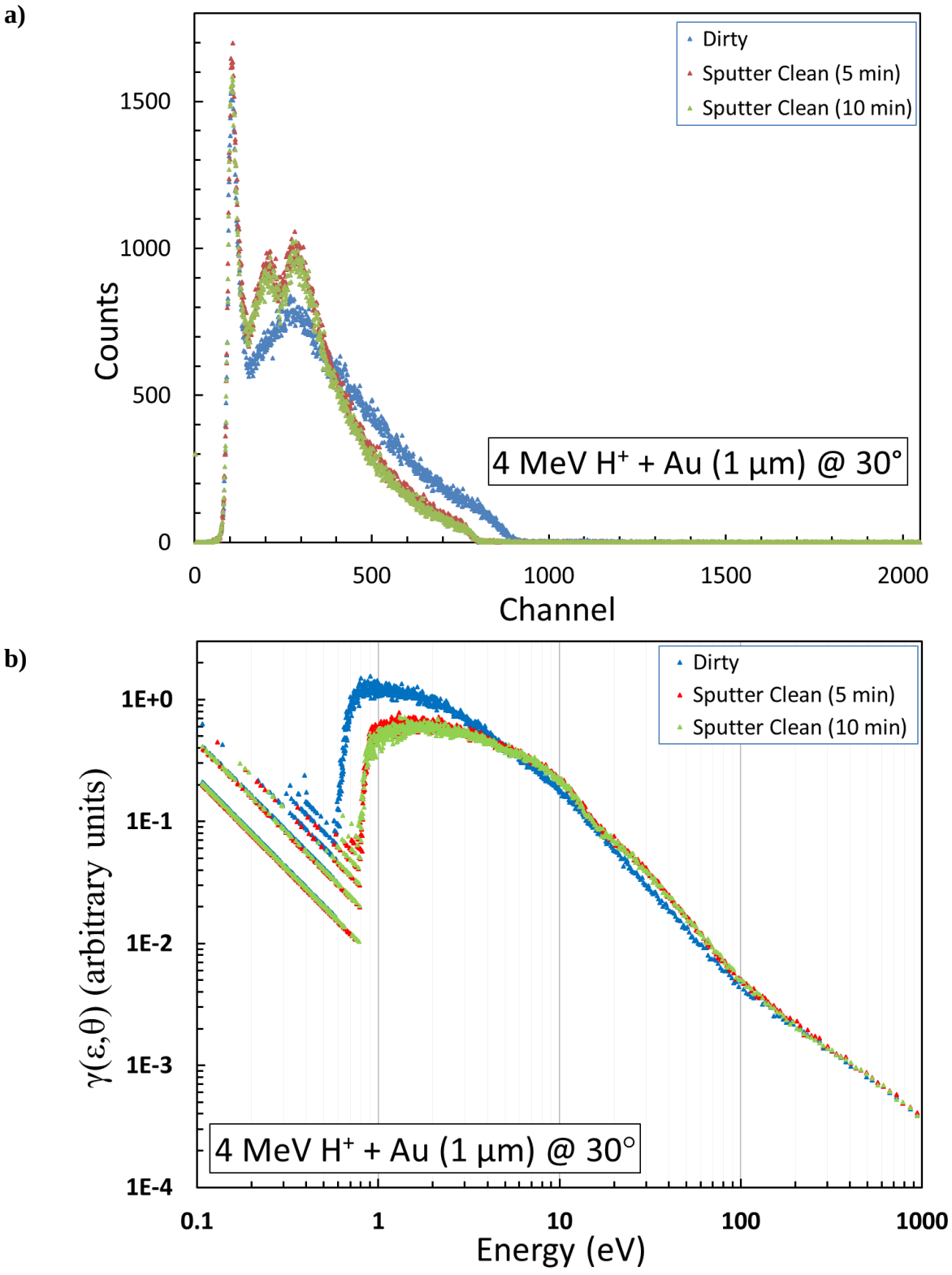

FIG. 3.13. A typical electron emission channel spectrum (a) and corresponding relative yield spectrum (b) are shown to illustrate the effects of target cleaning. Measurements were taken after successive 5-min sputter cleaning sessions until no observable changes were seen.

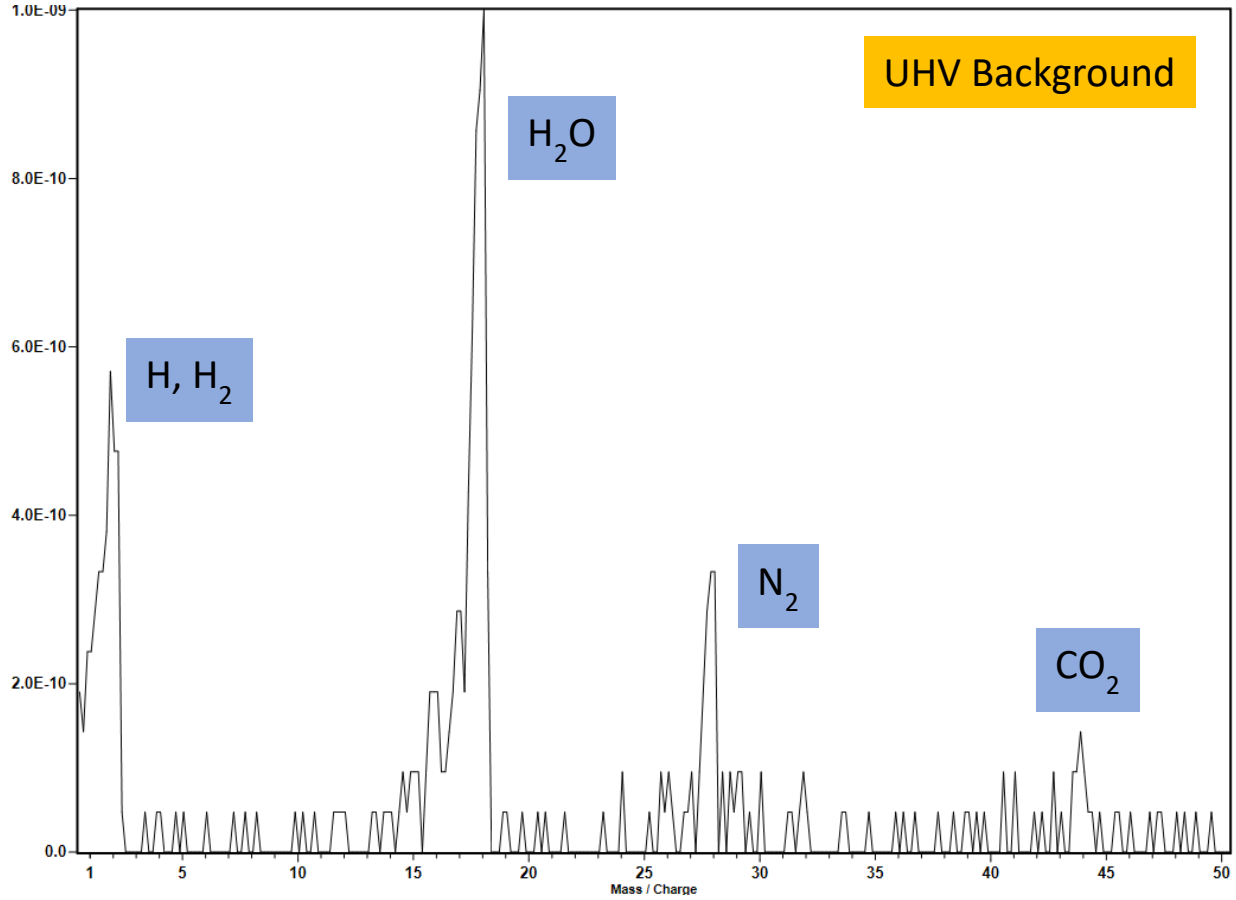

FIG. 3.14. A typical RGA spectrum of the UHV atmosphere is shown.

gasses (dirt). When the target assembly and cold-finger were not being cooled, for Au target electron emission measurements, an initial sputter cleaning was all that was necessary.

3.6.1: Amorphous Solid Water Target

After a clean Au-foil surface was obtained and the target assembly was cooled to ~40 K, purified de-ionized water was deposited on its surfaces as ASW by the background dosing method. To accomplish this, de-ionized (DI) water was purified by a "freeze-thaw" process to remove absorbed atmospheric gas contaminants. Then, the water vapor purity was verified and monitored by the UHV chamber RGA, by introduction of the water into the UHV chamber via the gas leak valve. Finally, the Au foil was exposed to the purified water at ~100 nTorr while the UHV chamber pressure was being monitored and recorded by the nude ion gauge, to determine the condensate thickness.

De-ionized water was purified by the freeze-thaw process. First, a 75-cm^3 stainless steel cylinder was cleaned with isopropyl alcohol and rinsed several times with DI water. Next, ~20 cm^3 of DI water was added to the cylinder, and the cylinder and DI water were frozen using liquid nitrogen. Then, while frozen, the cylinder was evacuated with a rotary-vane roughing pump, removing gasses from the cylinder. Last, the cylinder and DI water were allowed to thaw so remaining absorbed gasses could vaporize. This cycle of freezing, evacuating, and thawing was repeated several times.

The purity of the freeze-thawed water was confirmed by measurement of the constituent gasses with the RGA. The RGA spectra from DI water before and after the freeze-thaw process are shown in Figs. 3.15 and 3.16. The main absorbed atmospheric (contaminant) gas in the DI water was N_2, as seen in Fig. 3.15, accounting for ~34% of the total pressure of 51.9 nTorr,

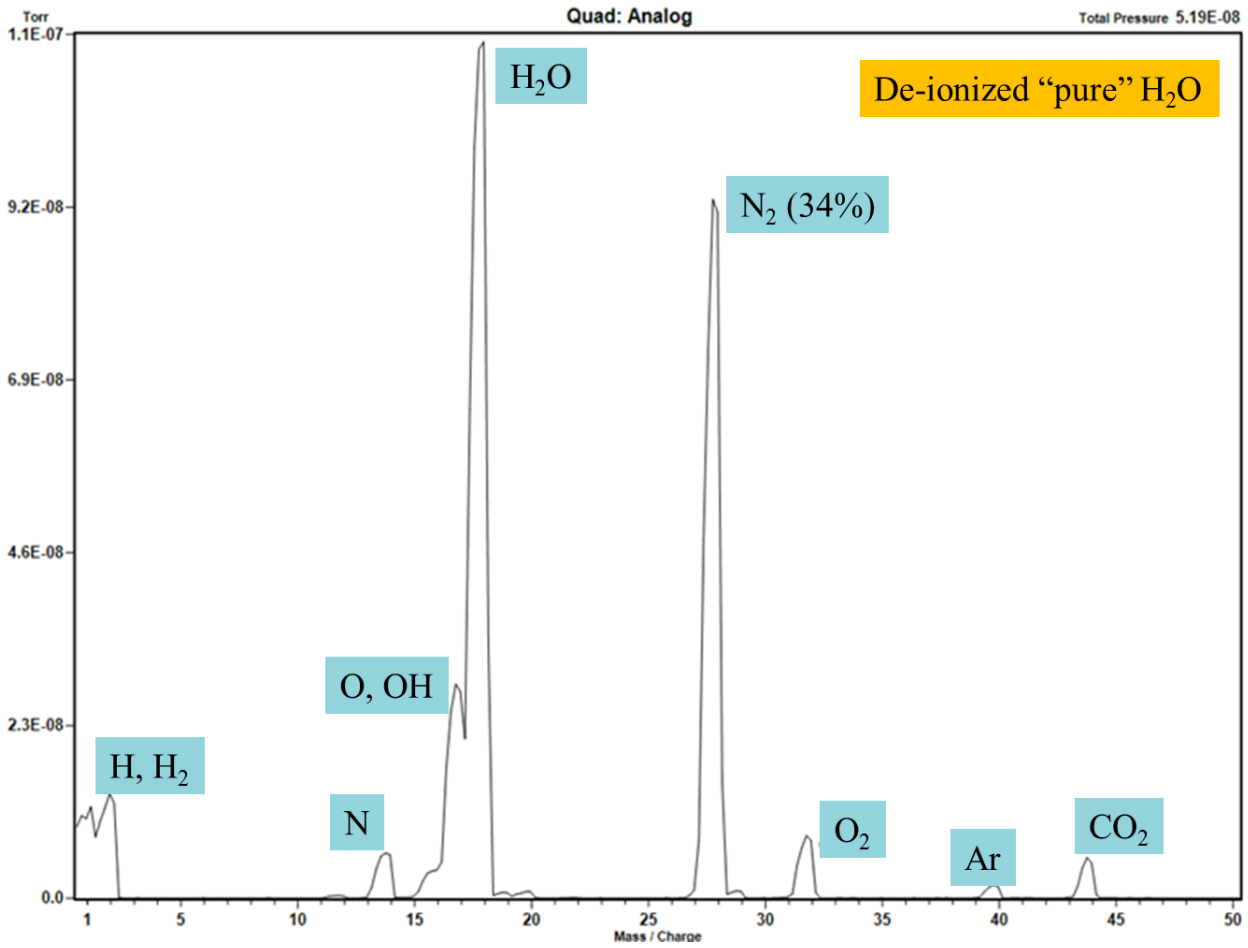

FIG. 3.15. Typical RGA spectrum of the DI water before the freeze-thaw process. Absorbed gasses of N, N_2, O_2, Ar, and CO_2 were present in significant proportions, particularly N_2. The H, H_2, and OH peaks are believed to be fragments of water.

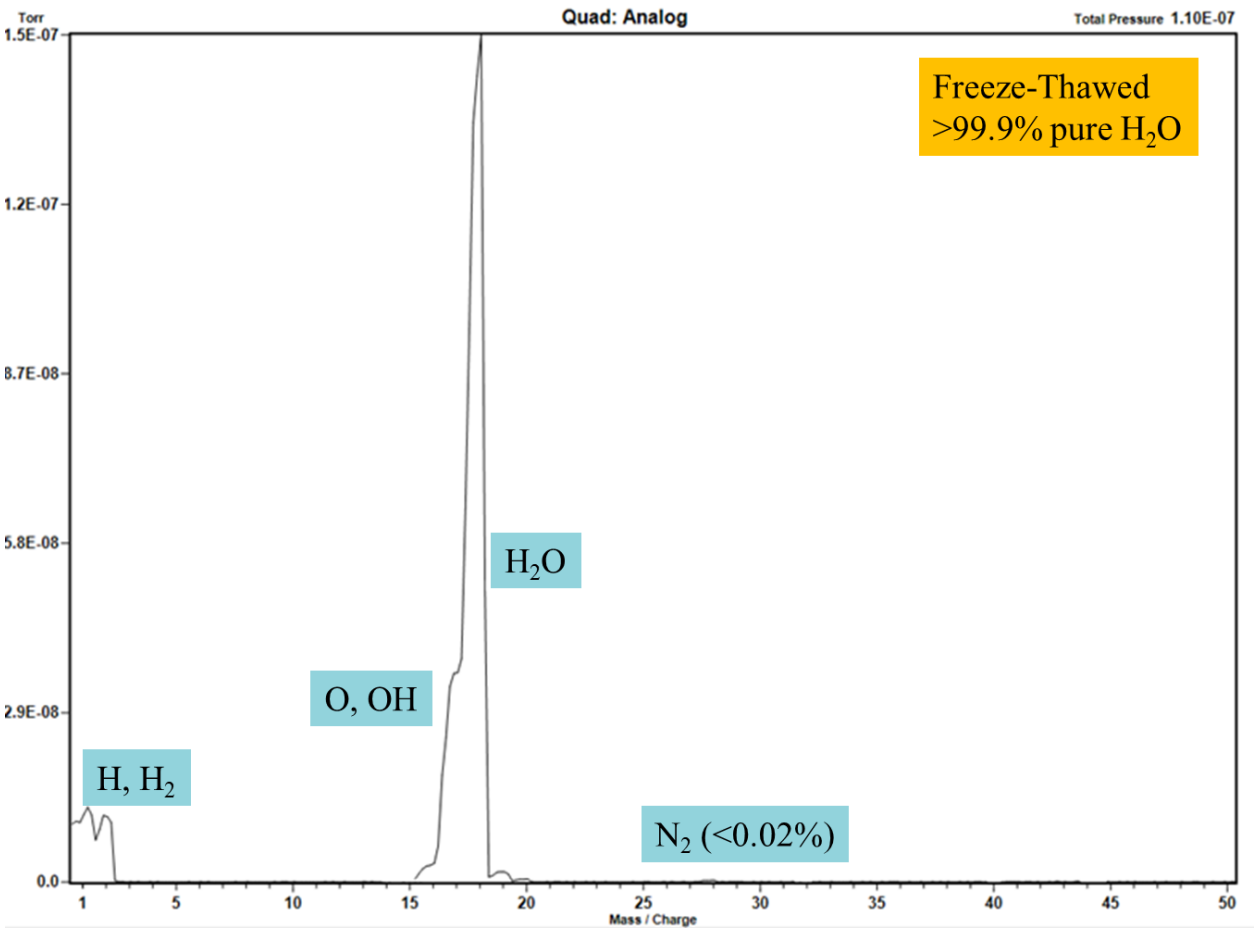

FIG. 3.16. Typical RGA spectra of the DI water after the freeze-thaw process, where N, N_2, O_2, Ar, and CO_2 absorbed gasses were reduced to insignificant proportions. The H, H_2, and OH peaks are believed to be fragments of water.

compared to ~42% water. Along with an N_2 fragment N, the other contaminants were O_2, Ar, and CO_2. As before, the peaks of H, H2, and OH were assumed to originate from water fragmentation in the RGA. After the freeze-thaw process, as seen in Fig. 3.16, the partial pressure of N_2 was 0.02 nTorr out of a total pressure of 110 nTorr, or <0.02%. This was similar to the background partial pressure of N_2 seen in Fig. 3.14. The absence of all other absorbed gasses indicates the freeze-thawed DI water contained at most only trace amounts of contamination and was >99.9% pure.

During ASW deposition, the UHV chamber pressure as measured by the nude ion gauge was recorded every 0.1 sec via the controller, NI board, and computer as shown in Fig. 3.10. The pressure was integrated over time by LabView® software to measure the cryogenic Au-foil exposure in units of Langmuir (L). A Langmuir is defined as the exposure resulting from 1 sec of interaction between a substrate and a gas of 1.0 μTorr pressure [58]. Expressed mathematically, 1 L = 10^{-6} Torr·sec. This exposure can be scaled linearly for lower gas pressures. For instance, 1 L would result from 10 seconds of 100 nTorr exposure as well as 100 seconds of 10 nTorr exposure. During ASW deposition, the pressure in the UHV chamber was limited to ≤100 nTorr to ensure the water vapor was diffuse. In this manner, the water molecules were assumed to impinge on the Au-foil isotropically. This isotropic incidence is important because it has been shown that ASW morphology depends on incident angle [47, 48, 90].

At the 40 K temperature used for ASW deposition, a monolayer is formed for each L of exposure, because any water vapor molecules impinging on the ~40 K Au foil will “stick” [48]. Electron emission measurements were made for successively thicker ASW condensates until a convergence was observed. This indicated that the electrons being detected were produced in the ASW, and not the Au foil. Therefore, it was concluded that a sufficiently thick ASW film was

deposited, thicker than the pathlength of any electrons generated in the Au-foil substrate. Once this thickness was obtained, secondary electron TOF was measured in 5-min runs for each angle. This process was repeated up to 3 times, in a random fashion to avoid systematic errors.

3.6.2: Gold Foil Target

After the initial Au-foil cleaning, 1 min of sputter cleaning was performed immediately before each electron emission measurement from the Au target, to ensure a clean target surface. In addition, data collection times were limited to ≤5 min. This time limit was decided upon because at a chamber pressure ~3 nTorr, up to a monolayer of condensation can adsorb to a surface every 333 seconds. This is an overestimation of adsorption rate, however, because Au target electron emission measurements were made at room temperatures of ~290 K, where the sticking coefficient is <1. Measurements were performed at each emission angle in a random ordering, to avoid systematic errors. The measurements were repeated up to 3 times per angle, in order to achieve higher total counts and show reproducibility.

Chapter 4: Results and Discussion

4.1: Introduction

For both Au and ASW targets, doubly differential electron emission yields $\gamma(\varepsilon, \theta)$ with respect to electron energy ε and emission angle θ were measured from proton and C-ion impact at several projectile energies. These relative yields were normalized to published values of total electron yields for Au targets, as discussed in chapter 3, resulting in absolute doubly differential electron emission yields. A thin-foil target was used to allow electron emission measurements to be made in both the forward and backward directions. Au was chosen for its relevance to nanoparticle radiotherapy. Additionally, its high atomic number (Z=79) made Au an ideal choice as a substrate for ASW film deposition. The high atomic number of Au ensured scattered projectiles predominantly interacted with the foil substrate as compared to the ASW condensate films, allowing normalization of ASW electron emission yields without the need for total yield data from ASW targets. ASW was chosen as a condensate target for its similarities to liquid water, the main constituent of soft tissue. The relative yields were measured with the TOF technique to optimize the energy resolution of the low-energy electron regime (<50 eV). These results help clarify the fundamental physics of charged-particle interactions with matter and allow direct tests of Monte Carlo track-structure simulations of the spatial dose deposition in biological materials.

Systematic tests were performed to assess the effects of surface contamination, level of signal pulse discrimination, and target temperature of many repeated measurements over the course of several weeks. Results of these tests will be presented in section 4.2.

Section 4.3 contains results from doubly differential electron emission measurements of proton impact on Au and ASW targets. These electron emission spectra were measured in the backward and forward directions, i.e. on the sides of the target that the proton enters and exits, respectively. Singly differential and total electron emission yields will be presented for proton energies of 1, 2, and 4 MeV.

C-ion projectiles were also studied, and the doubly differential electron emission spectra from their impact on Au and ASW targets are presented in section 4.4. Doubly-charged C ions of both 2.4 MeV and 6 MeV were studied. Additionally, triply-charged C-ion impact on Au was investigated to demonstrate the charge-state dependence, if any, on secondary electron emission from thin, condensed-phase targets.

4.2: System Tests

Several system tests were performed to assess the validity of the measurement system. For instance, electron emission measurements were performed over the course of the day to study the rate of surface contamination. Also, the level of discrimination used during the data acquisition process was studied to determine how the electron emission spectra were affected. Another test assessed the reproducibility of electron emission measurements over the course of a day and from week to week. This reproducibility test also examined the influence of target temperature on the emission spectra.

The surface conditions of the target are known to greatly affect the emission of secondary electrons in the low-energy region, particularly for $\varepsilon<10$ eV. As such, a reliable method of sputter cleaning the Au target surface was developed. Depending on the projectile and energy of

a particular measurement, the count rate of electrons in the TOF detector varied from several hundred to several thousand counts per second. Due to this fact, the total number of counts would depend on the run length (period of time for a measurement at a given angle). However, it was found that visible changes in the low-energy regime of the electron emission spectra were seen after only 10 min of exposure to background gasses in the UHV chamber. Fig. 4.1 shows the progression of the low-energy electron peak toward lower energy as time elapsed after an initial target sputter cleaning. This test was performed by repeatedly taking measurements at 30° every 5 minutes over the course of one hour, then every 15 minutes for several hours beyond that. The cutoff in the low-energy peak is initially at approximately 0.90 eV, decreasing to 0.75 eV after 15 minutes and 0.60 eV after 60 minutes. The height of the low-energy peak increased by roughly 13% over the 60 minutes interval. After completing these contamination measurements, the Au surface was sputter cleaned again, and a final electron emission measurement revealed a return to the shape and location of the initially clean spectrum.

This test confirmed that contamination lowers the surface barrier potential and increases the yield of low-energy secondary electrons, as discussed in chapter 2. For this reason, it was determined that measurements should be performed within the first ~10 minutes after sputter cleaning. So, a protocol was followed where a 5-minute electron emission measurement was performed immediately after sputter cleaning, and the next measurement would require a newly cleaned surface.

The level of discrimination used with the CFD was known to greatly affect the count rate of secondary electrons in the TOF detector. It was believed that due to the efficiency of the MCPs in detecting low-energy particles, it was possible that increasing the discrimination level could disproportionally affect the low-energy region of the electron emission spectra. To

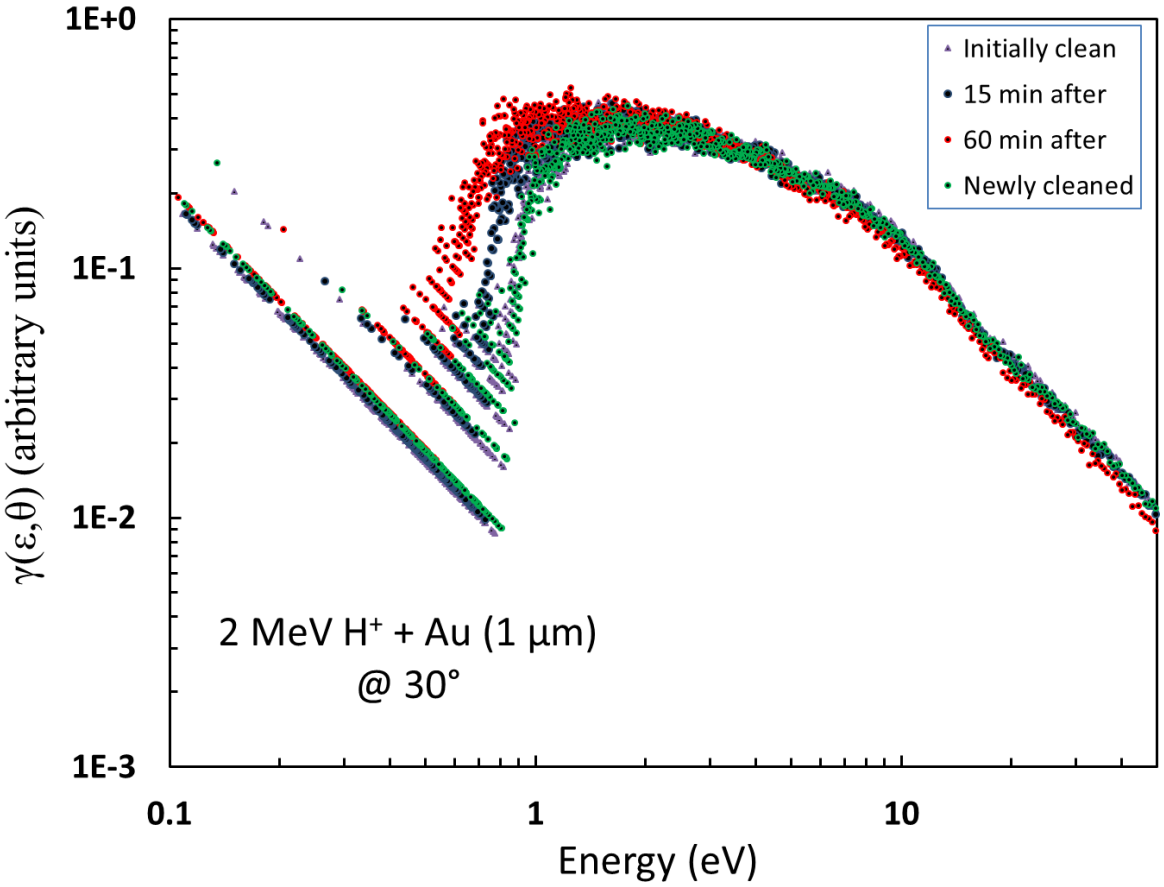

FIG. 4.1. Electron emission spectra at 30° from 2 MeV proton impact on Au are shown. The energy scale is truncated to focus on the low-energy portion, where it can be seen that surface contamination quickly affects the emission of electrons from a solid surface.

examine this affect, extended measurements were taken with a dirty Au-foil surface. In this manner, more low-energy electrons would be present in the emission spectra, and differences in the spectra at varying discrimination levels would be more apparent. Over the course of several days, measurements were repeated at over a dozen levels of discrimination.

Fig. 4.2 shows the spectra of two discrimination levels to illustrate the effects. These spectra were produced from extended measurement times of 40 minutes or more at 30°, and are composed of 2 million total counts. This was only valid because the Au target was dirty. It can be seen that a discrimination setting of 5.0 reduced the yield by approximately 50% across the entire range of energies. No observable differences are seen for low-energy vs. high-energy electron emission. Additionally, the low-energy cutoff does not seem to shift and is located at roughly 0.5 eV for both spectra. This cutoff value was determined at 10% of the maximum yield.

Fig. 4.3 shows the electron emission spectra at 30° from 15 separate measurements of 1 MeV proton impact on sputter cleaned Au at both room temperature of ~290 K and at cryogenic temperature of ~44 K. The titles for each series correspond to the run number, and are just for reference. Also shown is a numerical sum over all electron energies of these measurements, labeled “ALL”. This test was performed to determine the reproducibility of the measurement system over the course of several weeks and under varying target temperatures. It can be seen that a ±15% shift in energy is observed over the entire spectra from 1-100 eV. This can be attributed to several factors, including the energy resolution of the data acquisition process as described in chapter 3.

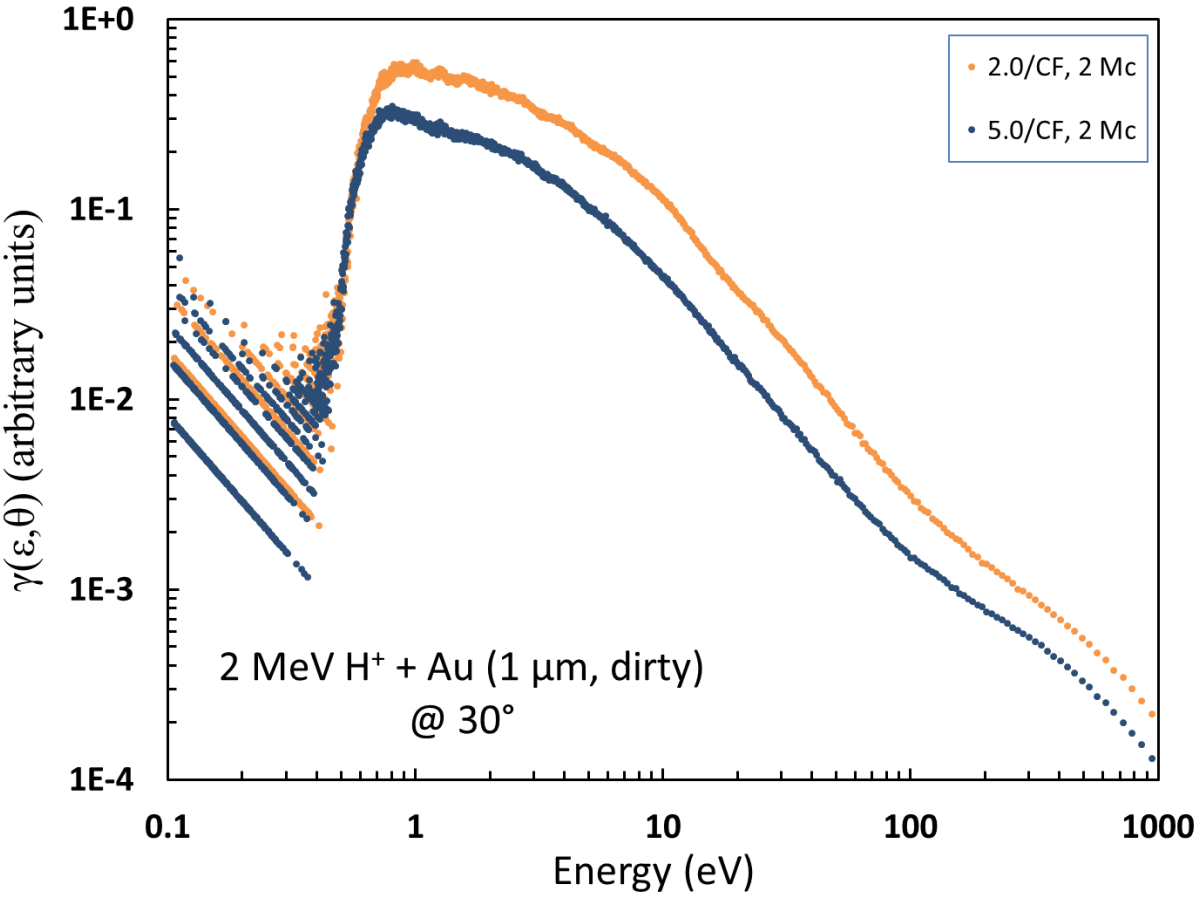

FIG. 4.2. Electron emission spectra at 30° from 2 MeV proton impact on a dirty Au target, where a shift in yield is seen over all energies due to the level of discrimination of the TOF detector pulses.

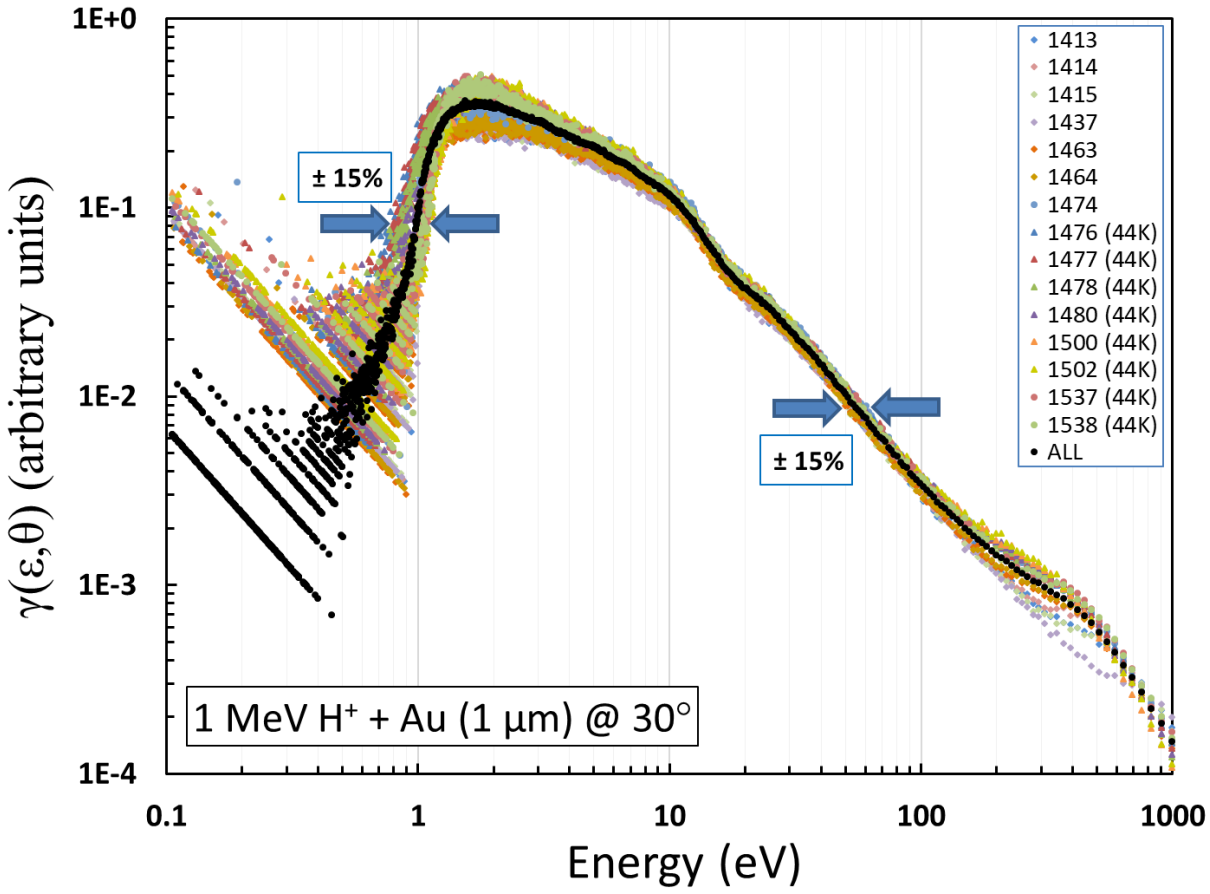

FIG. 4.3. Electron emission spectra at 30° from 1 MeV proton impact on Au. 15 measurement runs were performed over several weeks at both 290 K and 44 K, showing systematic error of 15% over all energies.

The reproducibility of a given data set over the course of a day showed no variation in electron emission spectra structure of yield. However, some variation was seen over the course of several days or weeks, even with the same target temperature. This is considered to be systematic error. Fig. 4.3 shows an estimate of the systematic error. The resolution of the TOF energy analysis technique is >20% at electron energies of 10 eV or more, so the 15% resolution seen in the reproducibility test is better than expected. However, at 1 eV the energy resolution is expected to be about 6%. The larger variation seen in Fig. 4.3 once again indicates the effects of surface conditions on low-energy electron emission from a solid. Even after sputter cleaning the target on a regular basis, variations in electron emission are still expected. This could be attributed to alterations in the surface of the Au target after repeated sputter cleanings.

4.3: Proton-Induced Electron Emission Spectra

4.3.1: Au Target

The spectra of absolute doubly differential electron emission yields from 1 MeV impact on Au-foil target of 1 μm thickness are shown in Fig. 4.4. These electron emission spectra were normalized using total backward yields from Benka *et al.* [8]. The upper graph shows the spectra from the forward direction at angles of 10-65° relative to the proton velocity. The spectra show a dominant low-energy peak at all angles. The location of this peak varies from ~1-4 eV and is dependent on angle. The peak location decreases from approximately 2.0 eV at 10° to approximately 1.6 eV at 30°, then increases at larger angles to roughly 3.5 eV at 65°. The heights of the low-energy peaks display a similar, yet opposite pattern. From 10° to 30°, the height increases approximately 41%. This is followed by a drop at increasing angles to a

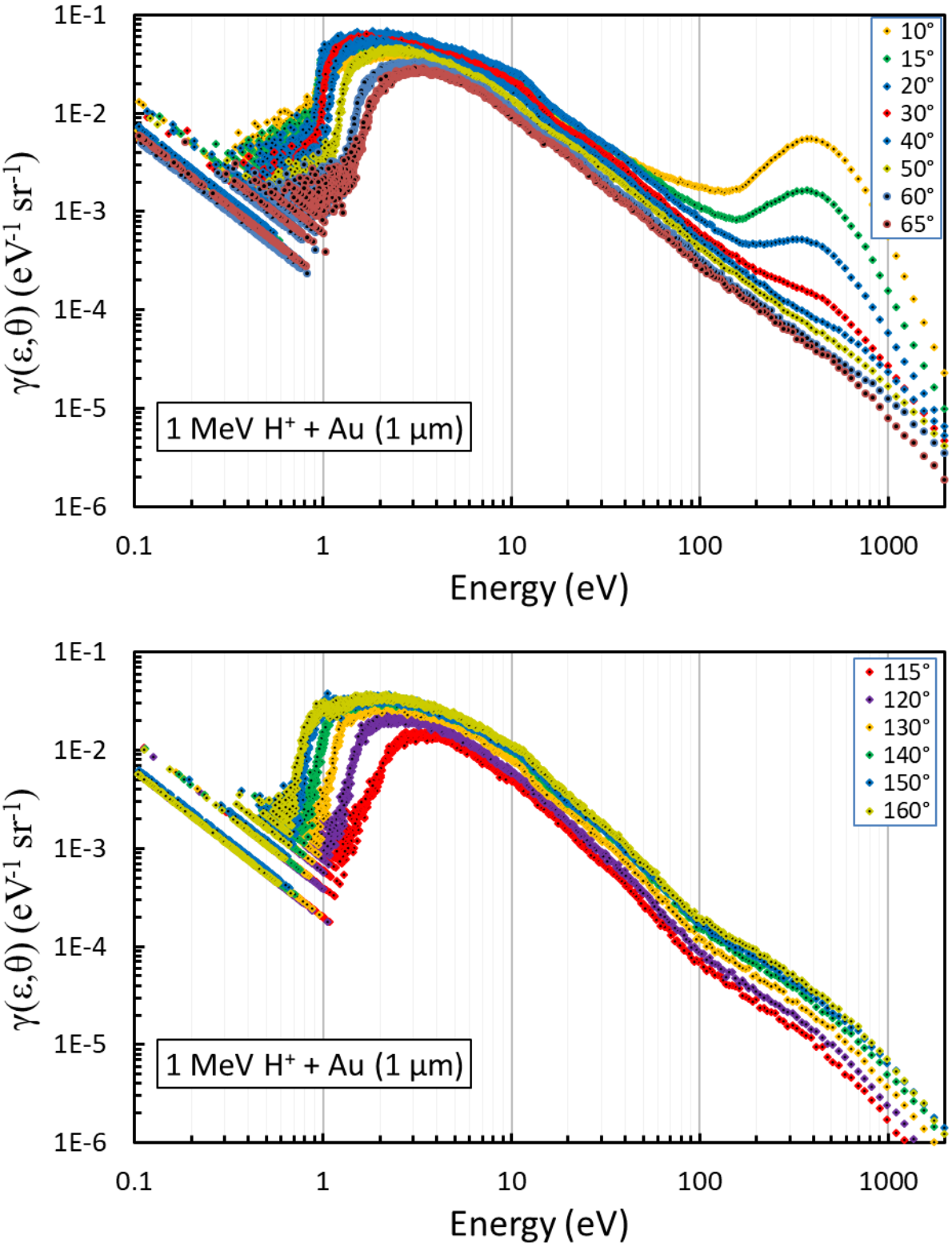

FIG. 4.4. Electron emission spectra from 1 MeV proton impact on 1 μm Au foil are shown in the forward (top) and backward (bottom) directions.

minimum height at 65°, approximately 55% lower than the maximum height at 30°. All angles show a low-energy cutoff in yield around ~1 eV. This value increases from roughly 0.9 eV at 10° to approximately 1.5 eV at 65°. The cutoff value was defined at the energy where the yield decreased to 10% of the maximum of the low-energy electron peak.

At electron energies above ~3 eV, the spectra at all forward angles follow the same general trend of decreasing yield. There is a shoulder present, where the yield is seen to dip slightly, at approximately 12.5 eV. The dip reaches a minimum at approximately 15-18 eV. Finally, there is a large, broad convoy peak centered at ~400 eV in angles of 30° or less. At 1 MeV initial proton energy, the location of the convoy electron peak is expected to be at 545 eV as calculated using equation 2.2. However, on the exit side of the foil, where the protons have slowed and decreased in energy to 0.87 MeV the expected convoy electron energy is 475 eV. The location of the convoy peak in the spectra shown in Fig. 4.4 is at a slightly lower energy, but this is expected for electron emission from a solid because many convoy electrons have undergone scattering between the depth in the solid where they were generated and the solid surface. The difference of ~70 eV corresponds to a 13% decrease in energy.

The backward electron emission spectra are shown in the lower graph of Fig. 4.4. The same features, excluding the convoy electron peak, are observed in the backward directions. All spectra exhibit a dominant low-energy electron peak. The low-energy peak location shifts from approximately 3.4 eV at 115° to 2.3 eV and 2.1 eV at 130° and 160°, respectively. Additionally, the height of the low-energy electron peak decreases by about 58% from a maximum at 160° to a minimum at 115°. The sharp decrease in electron yield at 115° suggests that the TOF detector might be near or within the shadow of the target holder assembly. The dip is present from roughly 12-19 eV, and a broad, subtle peak is present between approximately 100-1000 eV.

Increasing the proton projectile energy to 2 MeV resulted in the electron emission spectra seen in Fig. 4.5. The absolute doubly differential electron emission yields were normalized to total backward emission yield data from Benka *et al.* [8]. As with the electron emission spectra from 1 MeV proton impact on the Au target, the dominant peak of electron yield is in the low-energy portion of the spectra. The maximum yield for this low-energy peak is observed at 30° and located at approximately 1.9 eV. The location of the peak shifts to a higher energy of roughly 2.1 eV as the emission angle decreases to 10°. The height of the peak at 10° is about 15% lower than the maximum at 30°. For larger angles, the same holds true as the peak shifts to approximately 3.1 eV at 65° and decreases in height by about 54%.

The dip in electron emission yield is once again observed to occur from roughly 12-19 eV. The yields continue a downward trend at increasing energies. The convoy electron peaks are seen in the small angles of 10-20° and reach a maximum at approximately 750 eV. This location is once again lower than expected value for convoy electron energy of 1040 eV for 1.91 MeV proton energy after traversing the Au target. The energy difference of ~290 eV corresponds to a 28% shift due to electron energy loss during transport and emission from the solid target.

The backward electron emission yields, seen in the lower graph of Fig. 4.5 once again exhibit a dominant low-energy electron peak with a maximum height occurring at 160° at an energy of approximately 1.8 eV. This maximum peak decreases in height at smaller angles, by about 26% at 120°. The location of the low-energy electron peak increases in energy at smaller angles, to roughly 1.4 eV at 120°. The low-energy cutoff is between 0.7-0.8 eV for all backward angles.

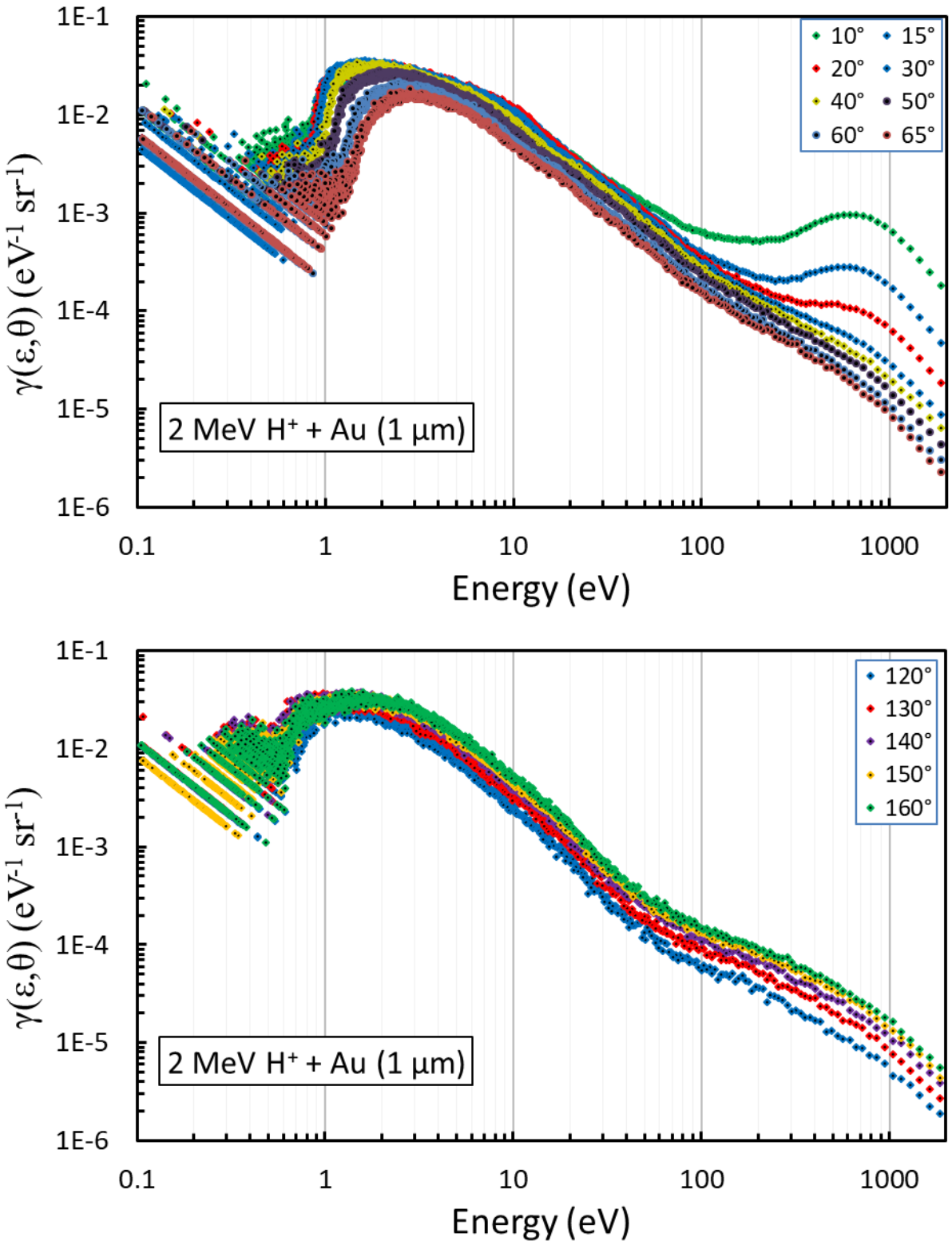

FIG. 4.5. Electron emission spectra from 2 MeV proton impact on 1 μm Au foil are shown in the forward (top) and backward (bottom) directions.

These measurements were the first to be made, before any other target/projectile combination was used, as a way of verifying the experimental setup by comparison to the results of McLawhorn [59]. With the renovation of the accelerator laboratory, the entire beamline and all components were removed and either reinstalled, replaced, or upgraded in some manner. The most significant change to the UHV target chamber and TOF electron analysis system was the development and commissioning of the new beam Pulser as discussed in chapter 3. Electron emission spectra from 2 MeV proton impact on Au are shown alongside data from McLawhorn [59] in Fig. 4.6. Overall shape and structure of the spectra show good agreement in the forward electron emission angles. The low-energy cutoff is ~0.1 eV lower than the previous data for both 20° and 60°, perhaps due to slight differences in TOF detector alignment or Helmholtz coil settings to minimize magnetic field contribution to slower electron trajectory. The backward spectra show greater differences in structure. Since both data sets were normalized in the same fashion, using total backward yield from Benka *et al.*, the disagreement in the structure for backward electron emission spectra from 2 MeV proton impact is not considered to affect the forward data set. The total backward yield of this work and that of McLawhorn are in agreement. The backward spectra were taken before the experimental technique was optimized, and were only used as a test run of the system. The agreement seen in the forward direction confirms that subsequent data sets were valid.

4 MeV is the highest energy that the 2 MV Pelletron accelerator can achieve for protons. Consequently, it is also the fastest atomic ion possible for the ECU Accelerator Laboratory, travelling at 2.75×10^7 m/s, or 9.2% of the speed of light. Electron emission spectra from 4 MeV proton impact on Au are shown in Fig. 4.7. The upper graph shows the forward direction of electron emission, with low-energy peaks occurring at approximately 2.1-2.3 eV for every

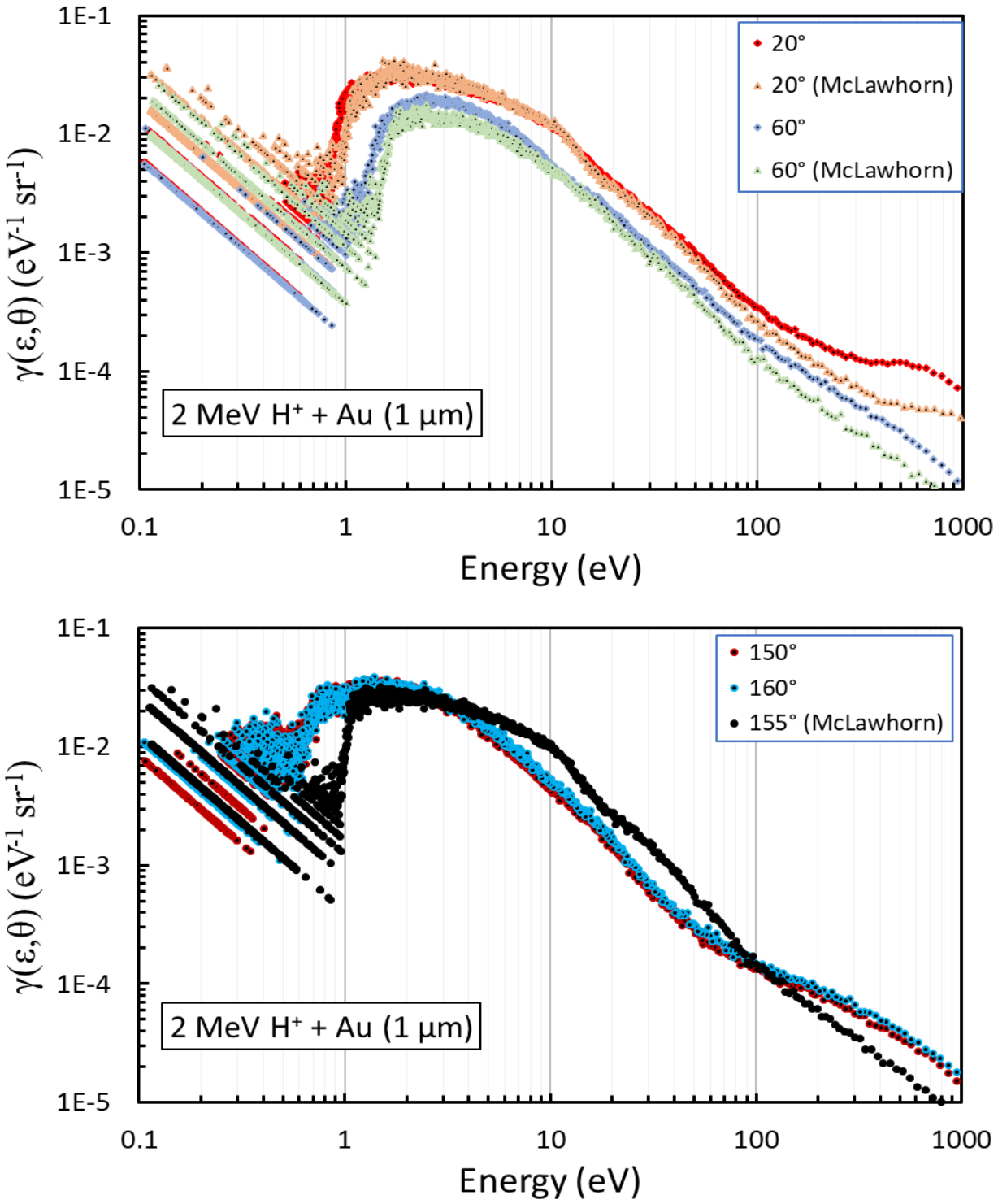

FIG. 4.6. Electron emission spectra at 20° and 60° are shown along with data from McLawhorn [59] in the upper graph. Comparison of spectra at backward angles of 150-160° can be seen in the lower graph. Yields in the forward direction differed by <10% overall and matched in shape. Less agreement can be seen in the backward direction spectra, except for the low-energy electron peak location.

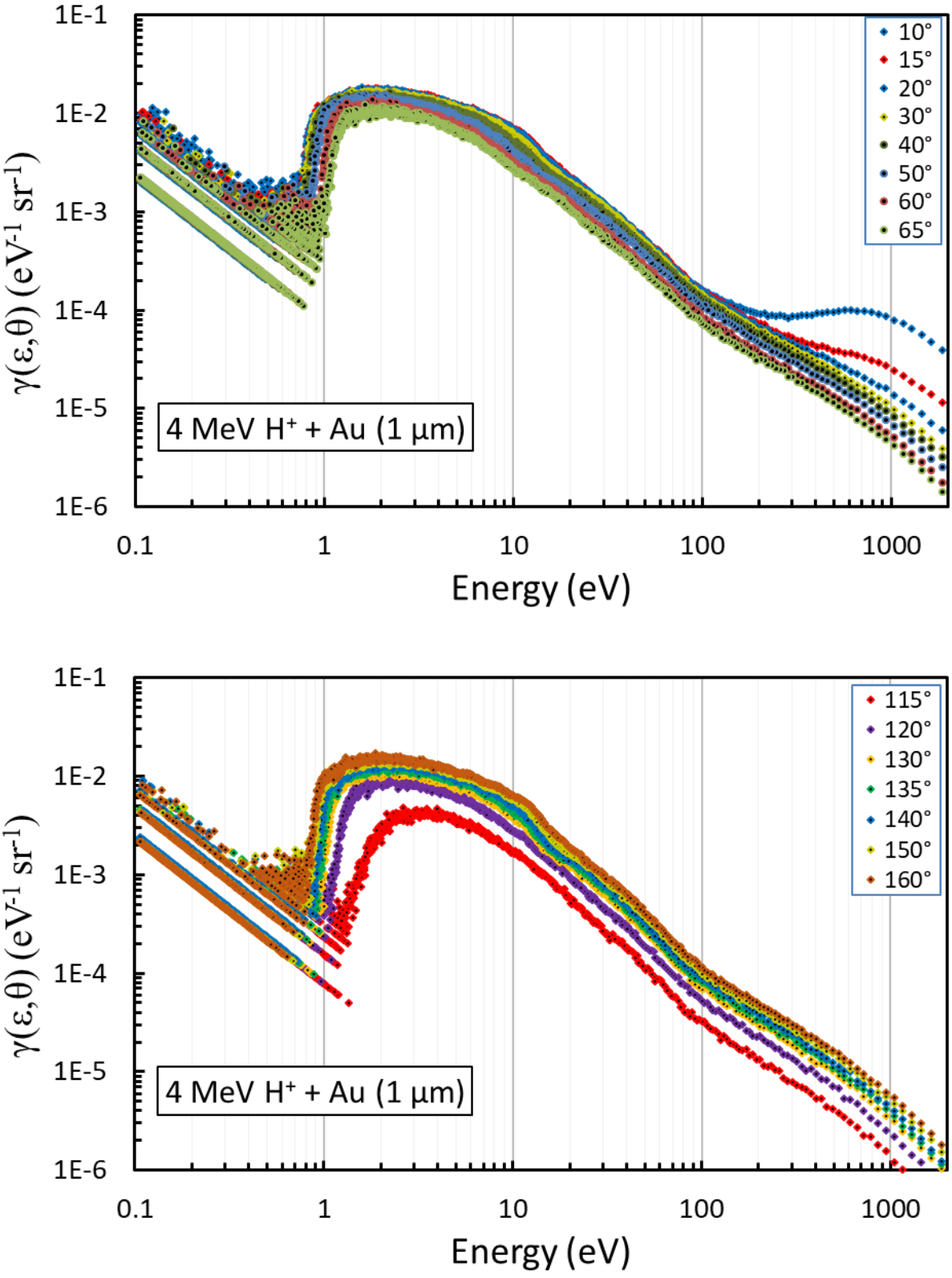

FIG. 4.7. Electron emission spectra from 4 MeV proton impact on 1 μm Au foil are shown in the forward (top) and backward (bottom) directions.

angle from 10-65°. The maximum low-energy electron peak occurs in the spectra for 20° emission. At increasing angles, the peak height decreases in magnitude. At 65° it is reduced by 41%. At small angles, the low-energy electron peak also decreases, losing 12% magnitude at 10° compared to 20°.

The convoy electron peak is once again seen at lower energy than expected for electrons travelling at the same speed as the proton projectiles. For 3.938 MeV protons, a convoy electron would have an energy of 2145 eV, but the convoy electron peak is observed at roughly 900 eV, or 58% lower. The dip is visible in the forward electron emission spectra for the energy range of 12-20 eV, but becomes indistinguishable at angles >40°. This pattern is also true for the backward emission angles, where the dip is not distinguishable at angles approaching 90°. It can be seen, however, at angles >130°.

The low-energy electron peaks in the backward directions are located between 3.3 eV at 115° and 2.1 eV at 160°. The heights of the peaks decrease at smaller angles, where the magnitude at 115° is 71% less than at 160°. This may indicate once again that 115° is slightly out of the range for the TOF detector to have a line-of-sight with the beam interaction spot on the target. The decrease in low-energy peak height at 120° is only 36% when compared to 160°.

4.3.2: Amorphous Solid Water Target

As with the Au target, electron emission spectra induced by 1, 2, and 4 MeV protons were measured. While many of the features are similar to those from Au targets, ASW targets exhibit some interesting features, particularly in the low-energy region of backward-emitted electrons. Before taking measurements, the exposure of the cryogenically cooled Au-foil substrate to the purified “freeze-thawed” DI water was studied. As mentioned earlier, the exposure of 1 L is considered to produce a monolayer of ASW film when the target is cooled to

35-50 K. There is some uncertainty in the measurement of the pressure with the Bayer Alpert gauge, which can be as much as 50% as stated by the manufacturer. This uncertainty in monolayer thickness of the ASW film was accounted for by taking electron emission measurements over a 0-500 L range and comparing the spectra in overall yield and shape.

The ASW buildup spectra can be seen in Fig. 4.8 for both 30° and 150°. The spectra all agree above 10 eV for exposures >70 L. Below 10 eV, the low-energy electron peak at both angles decreases in location by approximately 0.2 eV and increases in height by over 100% with an exposure of only 20 or 30 L as compared to bare Au. This change in the low-energy peak occurs at lower levels of exposure in the backward direction as compared to the forward direction. This increased rate of change is attributed to the location of the UHV leak valve, positioned at 135° with respect to the projectile beam. Therefore, even at 100 nTorr exposure pressure, there is still an enhanced interaction of the back of the target with the diffusing DI vapor cloud. However, in both directions the electron emission spectra are seen to converge at 100 L. At this amount of exposure, the rate of change in the low-energy peak location and height is minimal. For instance, between 70-150 L the low-energy peak cutoff agrees to within ±0.1 eV at both angles. The maximum is located within ±0.1 eV at both angles and at a height varying by 4% at 30° and 13% at 150°.

The shift at increasing exposure >150 L is attributed to target charging. ASW has insulating properties, and as the film thickness increases the distance from the surface of the ASW to the electrically grounded Au substrate increases. This allows charge to accumulate in the ASW film and effectively raises the surface barrier potential, limiting the emission of low-energy electrons. The height of the low-energy electron peak at 500 L is up to 50% lower than at 100 L. Also, the low-energy cutoff increases by approximately 0.5 eV over this exposure range.

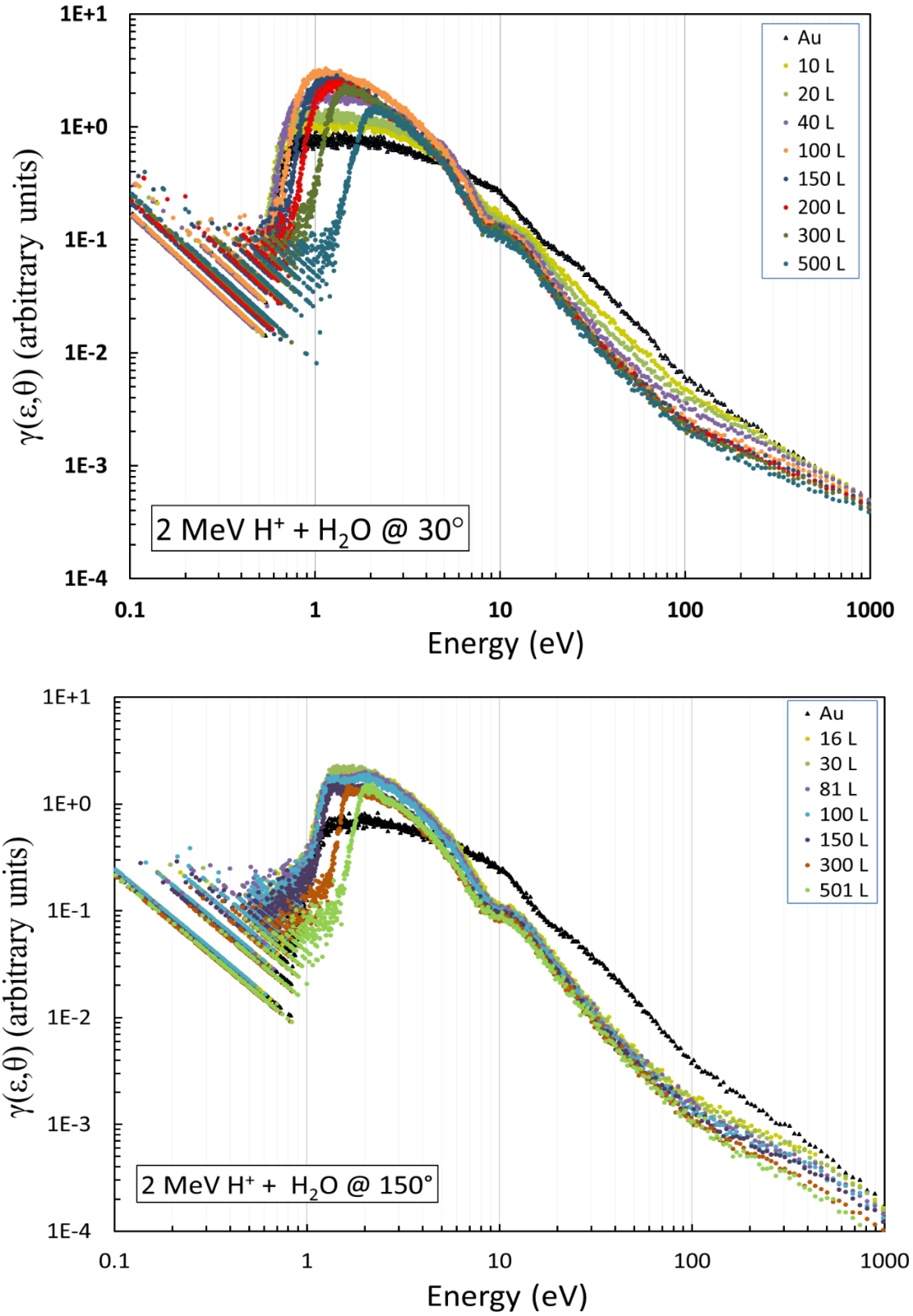

FIG. 4.8. Electron emission spectra at 30° (top) and 150° (bottom) of 2 MeV proton impact with Au target substrate with 0-500 L of ASW film.

Therefore, minimal differences in the electron emission spectra were seen between 70-150 L in both forward and backward directions, as compared to the drastic changes that occur in the first 10-30 L of exposure and at increasing exposure above 150 L. For these reasons, 100 L was chosen as an exposure which was assumed to produce a film of ASW that exceeds the range of electrons, but does not significantly affect the probability of escape due to target charging.

This value is different than what was observed by McLawhorn, who determined that 200 L was an ideal exposure [59]. The difference can be attributed to one or two factors. First, several years elapsed between the work of McLawhorn and the work presented here. The accuracy of ionization gauges is known to drift over time, and the error in pressure measurement may have propagated into the calculation of exposure. Therefore, it's possible that the thickness in both experiments was in fact the same. Second, the purification process of the DI water was improved in this experiment. The absorbed gasses, particularly N_2, were only measured in trace amounts for this work (<0.02%) as compared to a 3% partial pressure in the work by McLawhorn [59]. Impurities are known to affect the emission of electrons, and therefore the range of exposure where the spectra showed little deviation may have been shifted.

The electron emission spectra for 1-4 MeV proton impact on 100 L of ASW are shown in Figs. 4.9-4.11 for both forward and backward directions. These doubly differential secondary electron emission yields were normalized using the same factor determined for Au targets in the previous section. At 100 L exposure, the thickness of the ASW film was assumed to be 100 monolayers. Even if a 50% error in pressure measurement and calculation of exposure is present, the maximum expected thickness would be approximately 200 ML on both sides of the Au substrate. A total of 400 ML of ASW would not significantly affect the Rutherford scattering of the proton projectiles from the Au substrate, as the atomic number of Au is far higher than

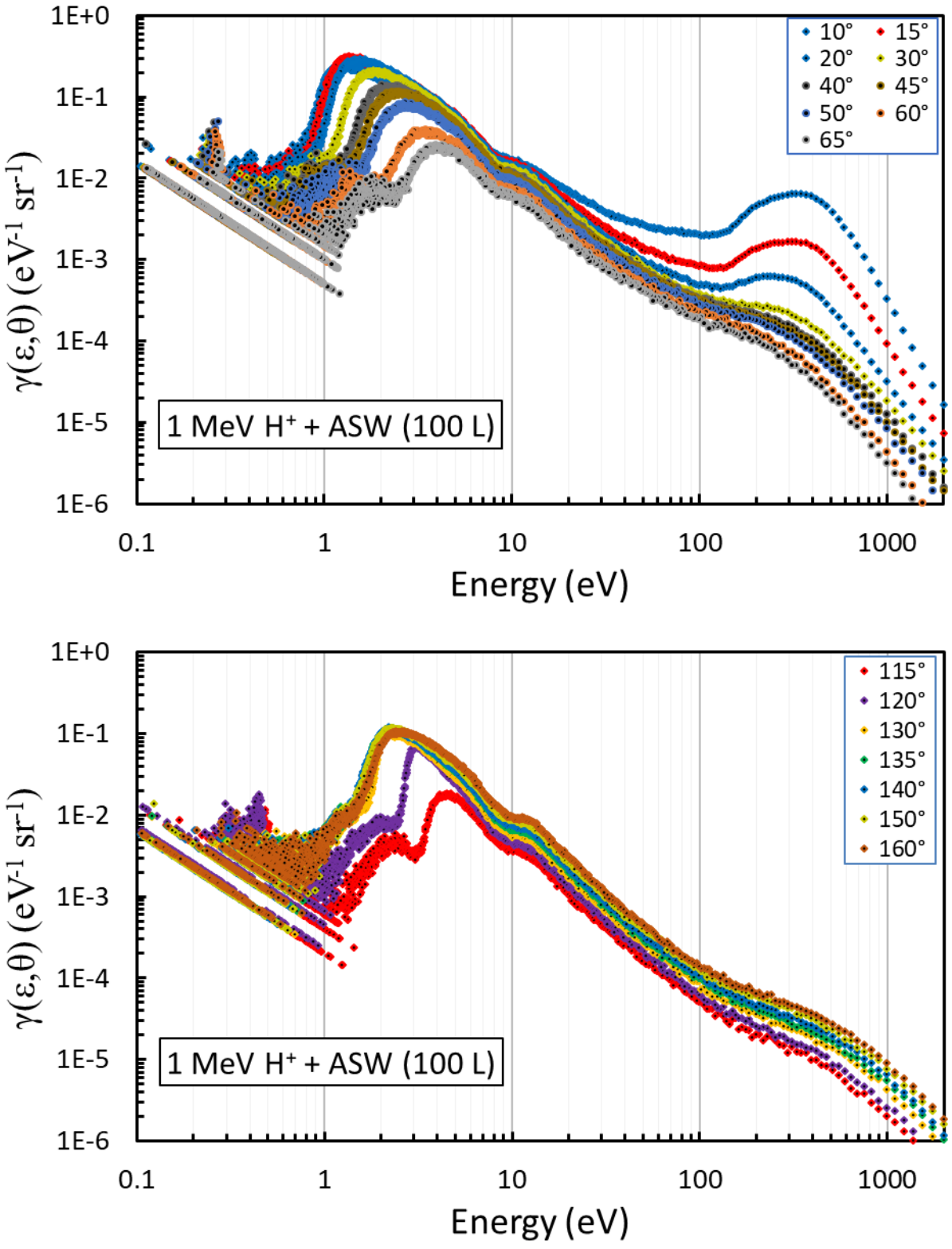

FIG. 4.9. Electron emission spectra from 1 MeV proton impact on 100 L of ASW deposited on a 1 μm Au-foil substrate are shown in forward (top) and backward (bottom) directions.

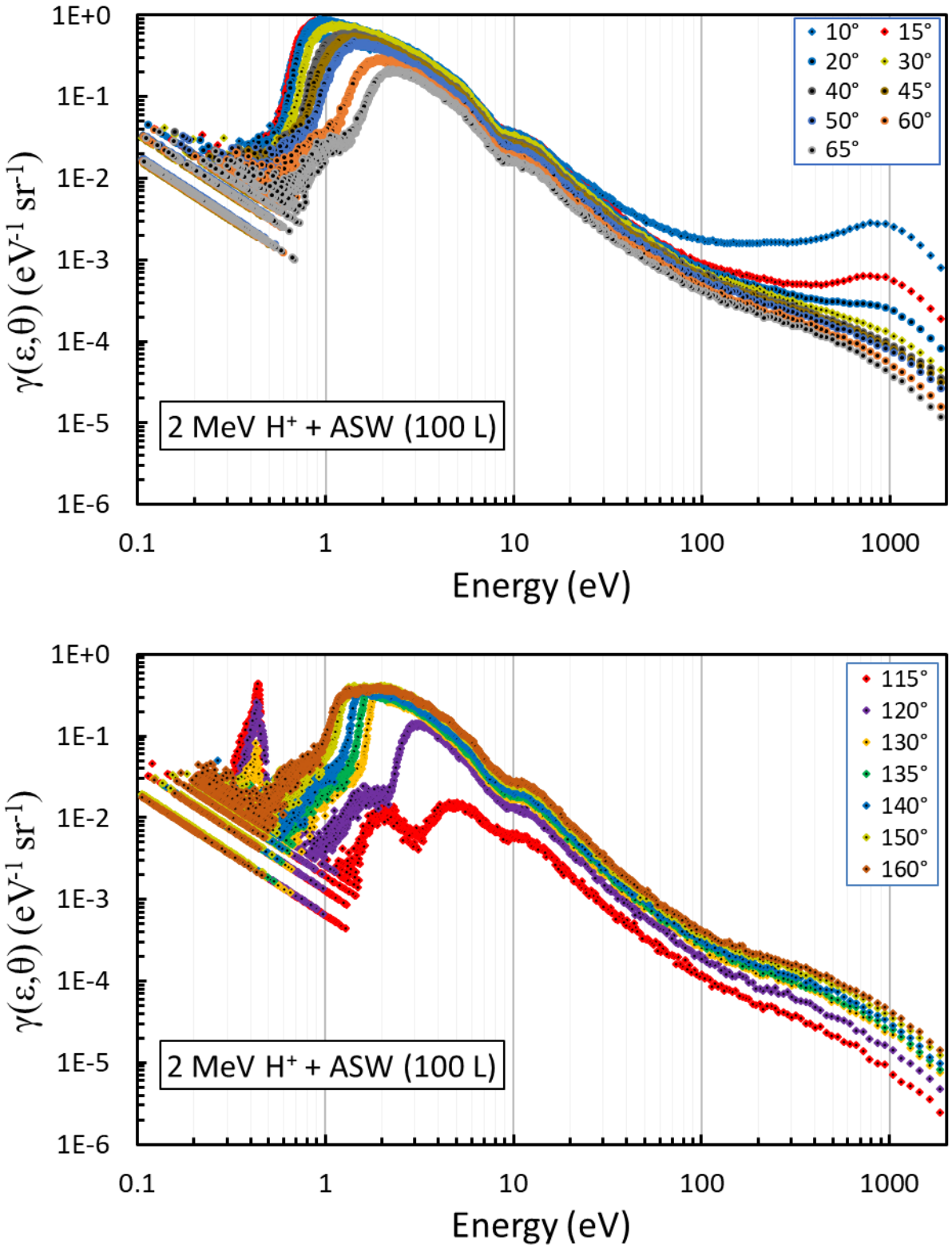

FIG. 4.10. Electron emission spectra from 2 MeV proton impact on 100 L of ASW deposited on a 1 μm Au-foil substrate are shown in forward (top) and backward (bottom) directions.

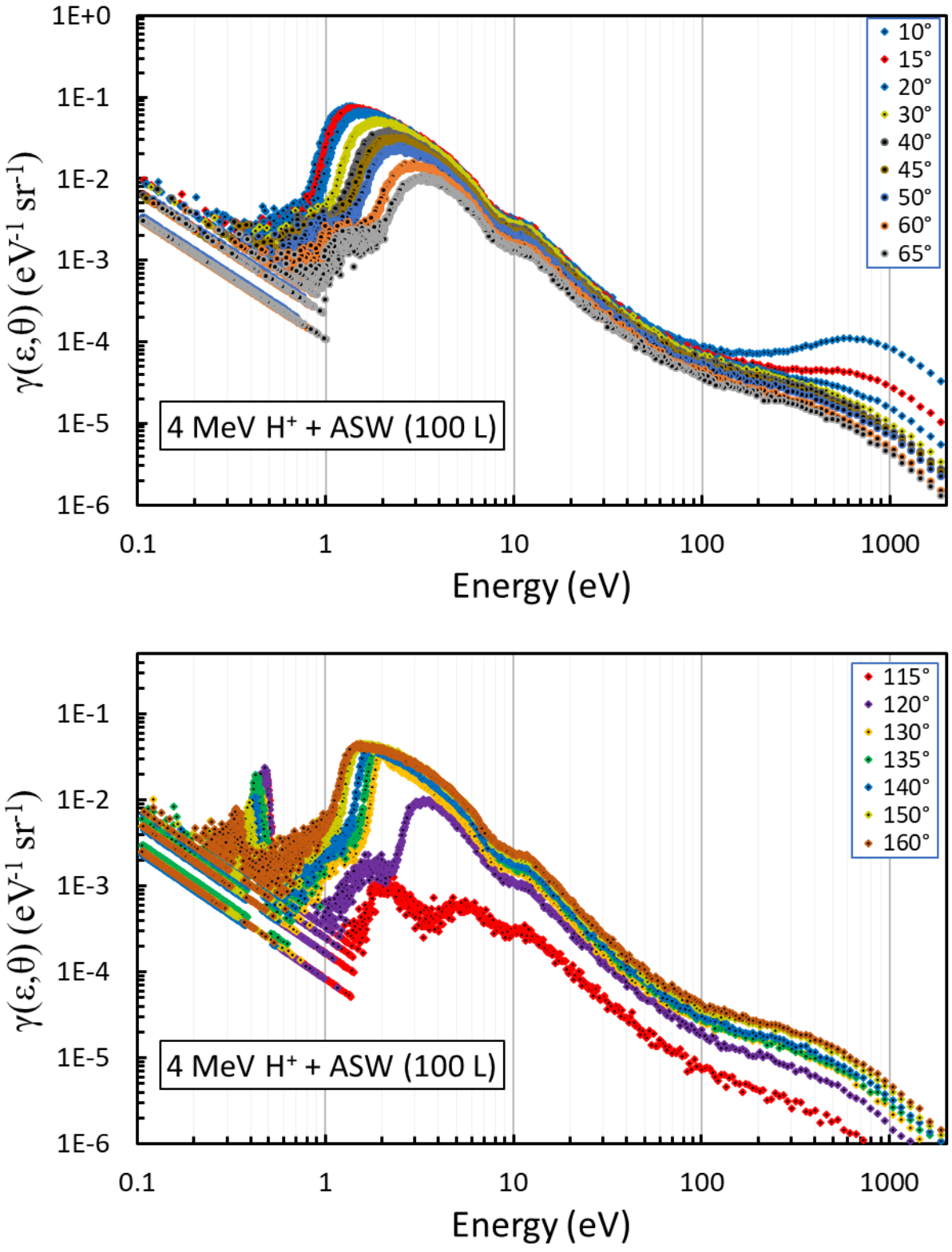

FIG. 4.11. Electron emission spectra from 4 MeV proton impact on 100 L of ASW deposited on a 1 μm Au-foil substrate are shown in forward (top) and backward (bottom) directions.

water and the thickness of 1 μm is significant compared to that of the water. An atomic radius for water is reported by Itikawa and Mason to be 0.096 nm [44]. Therefore, 400 ML would equate to approximately 77 nm of ASW.

The low-energy electron peak is located at energies between 0.9-4.0 eV and follows the same trend as with the Au target: the position of the peak shifts to higher energy as the emission angle becomes more perpendicular to the beam. Additionally, the height of the low-energy electron peak decreases at larger angles from the beam axis. Both of these trends are expected due to the process of electron escape from the surface of a solid as discussed in chapter 2, such as the probability of escape and the angles defined by the escape cone from equations 2.15 and 2.16.

At all proton energies, the low-energy electron emission peak is more pronounced in ASW than Au. The dip is no longer seen in the 12-20 eV range. There is, however, a broad yet fairly pronounced peak in the electron emission spectra at approximately in all proton energies at all electron emission angles spanning from approximately 9-19 eV. The maximum of this peak was found to occur at roughly 13 eV. This is most likely attributed to the autoionization of water as seen in electron projectile impact studies conducted by Wilson *et al.* [108]. They reported a peak located at approximately 11 eV. The difference of 2 eV is within the energy resolution of the TOF system of 20% at 10 eV. However, the value determined in this work is in close agreement with the theoretical work by Itikawa and Mason, who report an ionization energy for water of 12.6 eV [44]. Additionally, the autoionization peak does not shift in position as electron emission angle changes and is independent of projectile energy. Because the autoionization is related to the target material in this case, both of these features are expected.

An interesting feature in the backward emission spectra is the presence of another low-energy electron peak in the vicinity of 0.45 eV. Once again, this peak does not change location based on emission angle or proton energy. It was first assumed that this peak was an artifact of the background dosing technique due to the location of the UHV leak valve at 135° with respect to the beam, even though the pressure in the UHV chamber during ASW deposition was restricted to ≤100 nTorr and the vapor cloud was considered diffuse. It was theorized that during expansion of the water vapor as it was introduced into the chamber, freezing occurred at the inlet and produced jet streams of water vapor and therefore the ASW film was not uniform on the entrance side of the target. However, the 0.45 eV peak was also observed a day after ASW electron emission measurements were completed and the target had been sputter cleaned. In this case, the Au-foil substrate was exposed overnight to residual water vapor, in the 0.5-5 nTorr pressure range. Therefore, the 0.45 eV structure cannot be attributed to the background dosing technique. It's difficult to say what this peak is attributed to, since it is in the extreme low-energy region where normally only background counts are observed. However, it wasn't present in the Au target emission spectra, suggesting that it was an attribute of electron emission from ASW.

4.3.3: Proton Energy Dependence

Fig. 4.12 shows the dependence of the secondary electron spectra on proton energy for emission angles of 20° and 60°. The data from McLawhorn [59] is once again shown for comparison. These spectra were all taken from 1 μm Au-foil targets, and are expected to exhibit the same features, particularly in the low-energy region where surface conditions and other target parameters are the dominant factors. The secondary electron yield is known to scale with the stopping power, as discussed in chapter 2. As expected, the yield increases with decreasing

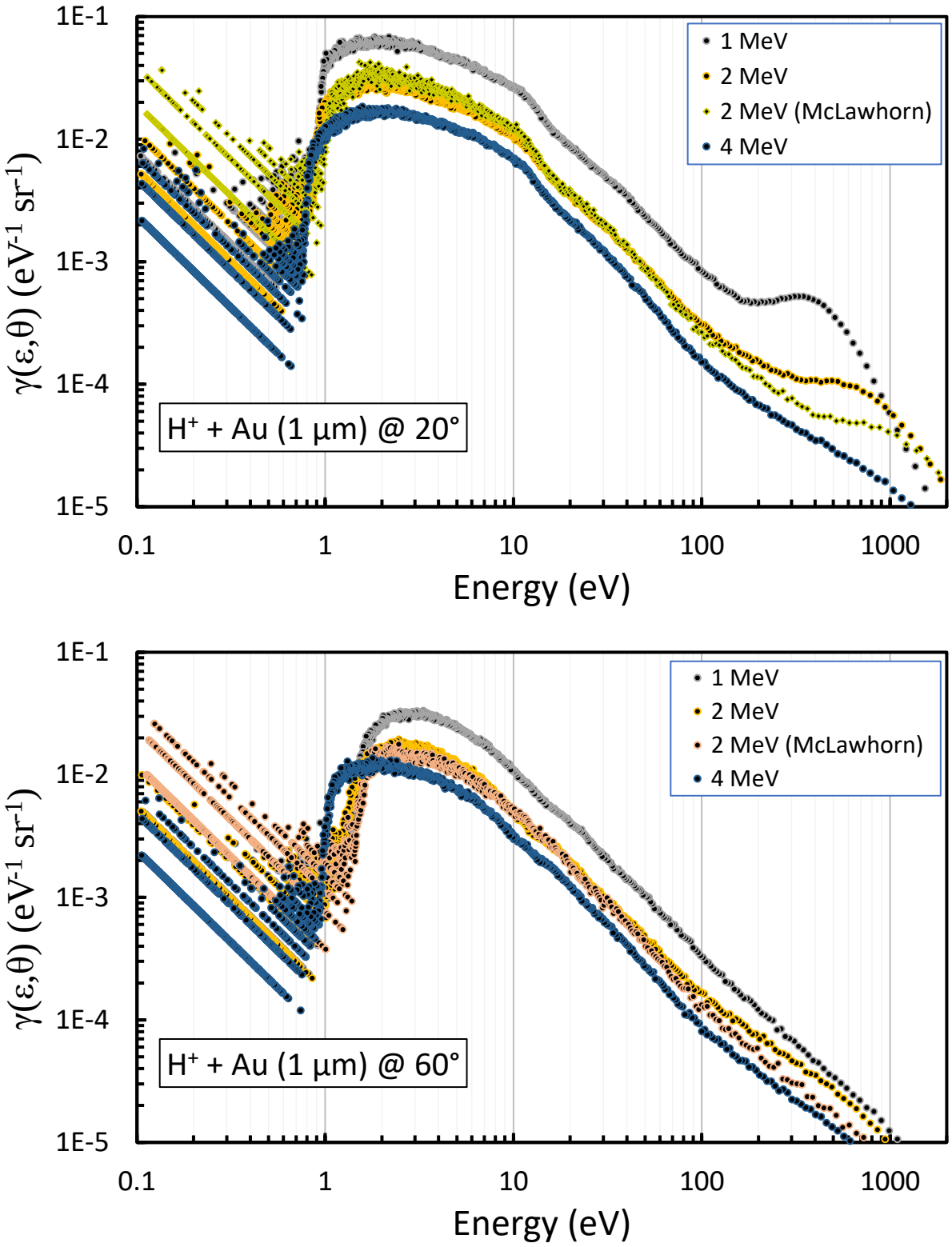

FIG. 4.12. Electron emission spectra from 20° (top) and 60° (bottom) are shown for 1, 2, and 4 MeV protons on Au. Also shown is the data from McLawhorn for 2 MeV protons on Au [59].

proton energy. This follows from the stopping power of protons in Au, as given by Ziegler *et al.* [114]. The stopping power of protons in Au increases by approximately 48% as the projectile energy decreases from 3.94 to 1.91 MeV, the energies of 4 and 2 MeV protons after traversing the 1 μm thickness of the Au-foil target. As the energy decreases from 1.91 to 0.087 MeV, another ~44% increase in stopping power is given in the literature.

The dip, as it's been referred to, seems to be independent of proton energy. This suggests that it can be attributed to properties of the Au target. It doesn't correspond to the Auger transition peaks observed by Rothard *et al.* [80] for various OVV, NVV, NNV transitions corresponding to approximately 40, 70, 140, and 270 eV. The cutoff of the low-energy electron peak shows a dependence on proton energy. This is more pronounced at larger angles, shifting from approximately 1.0 eV for 4 MeV protons to roughly 1.4 eV for 1 MeV protons at 60°. At 20°, the shift in the low-energy electron cutoff is only about 0.1 eV. This may be attributed to the probability of escape for electrons of a given angle, and the relationship of this probability to the escape cone. However, it could be attributed to the Au target surface.

The backward direction for electron emission shows a reverse trend in low-energy cutoff as it relates to proton energy dependence. This can be seen in Fig. 4.13 for electron emission at 160°. The location of the cutoff shifts from 0.7 to 0.9 eV as the proton energy is increased from 1 to 4 MeV. This is further evidence that the low-energy portion of electron emission spectra are extremely dependent on surface contamination and morphology of the target. However, above 1 eV the electron spectra follow the same trend. Due to the differences seen in low-energy cutoff in the forward and backward direction as they relate to projectile energy dependence, it might be prudent to set a lower limit of 1 eV for trustworthy results.

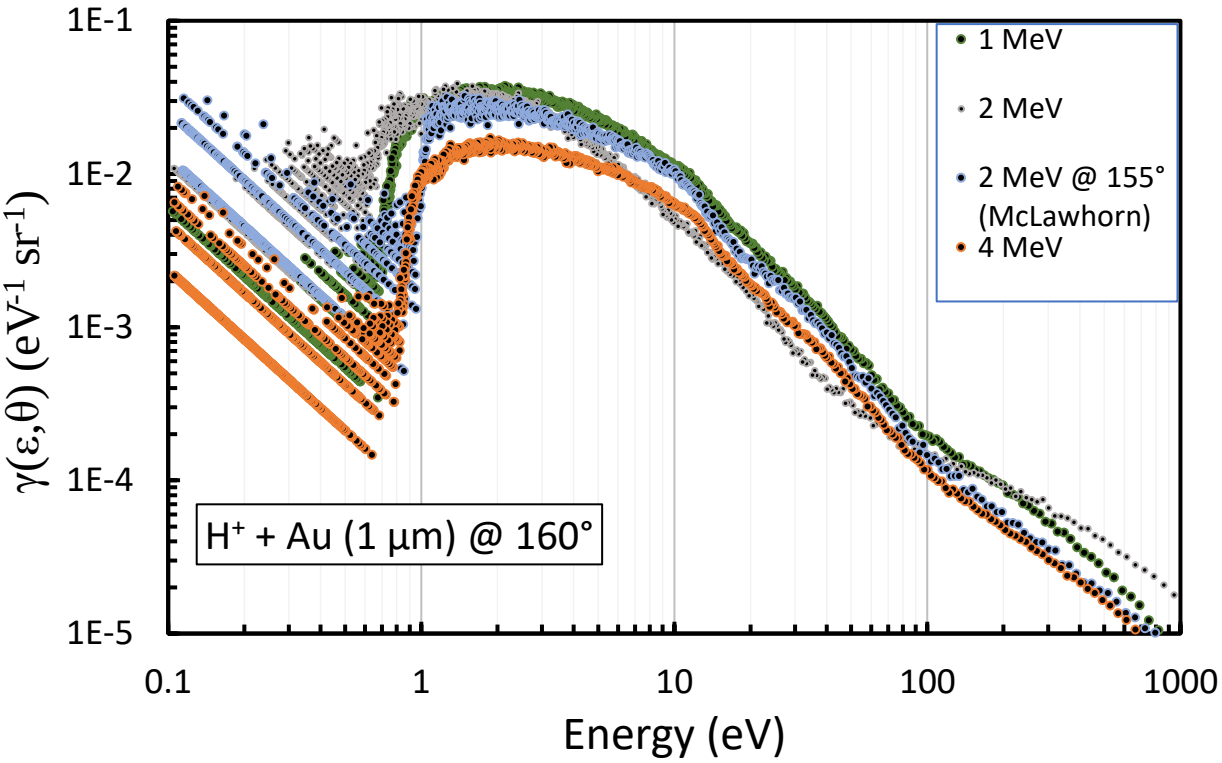

FIG. 4.13. Electron emission spectra are shown at 160° for 1, 2, and 4 MeV proton impact on Au, as well as data from McLawhorn [59] for 2 MeV protons at an emission angle of 155°.

Fig. 4.14 shows the projectile energy dependence of secondary electron emission from ASW targets. The energy scale was truncated to 100 eV to highlight the differences in the low-energy portion of the spectra. In the upper graph of electron emission at 10°, it can be seen that the overall yield in secondary electrons increases with decreasing proton energy. Once again, this is attributed to the increase of stopping power, in this case for protons in water. According to Ziegler *et al.*, the stopping power of protons in water increases by approximately 73% as the energy decreases from 4 to 2 MeV, and an additional increase of 76% for 1 MeV protons. The autoionization peak at approximately 13 eV shows no dependence on projectile energy, as discussed earlier. The cutoff of the low-energy electron peak deviates for 2 MeV protons as compared to the other proton energies. Possible explanations for this may be charging of the target or perhaps a faulty connection in the wire used to electrically ground the target. The general features of the electron emission spectra agree above ~2.5 eV for all proton energies.

The lower graph in Fig. 4.14 shows the emission spectra at 120°. This angle was chosen to illustrate the 0.45 eV electron peak, that seems to be independent of proton energy. At all proton energies, the peak is located between 0.4-0.5 eV. The height of the peak increases by approximately 85% as the proton energy is lowered from 4 to 2 MeV. However, this trend does not continue for 1 MeV proton-induced emission, where the height of this peak is roughly 47% lower than the 4 MeV peak.

4.3.4: Singly Differential and Total Electron Emission Yields

For proton impact on Au, the doubly differential yields $\gamma(\varepsilon, \theta)$ were integrated numerically over all electron energies to produce singly differential yields $\gamma(\theta)$. This was done for all proton energies. As described in chapter 2, a cosine dependence is expected for angular yields, as the escape of electrons from the surface of a solid requires sufficient velocity

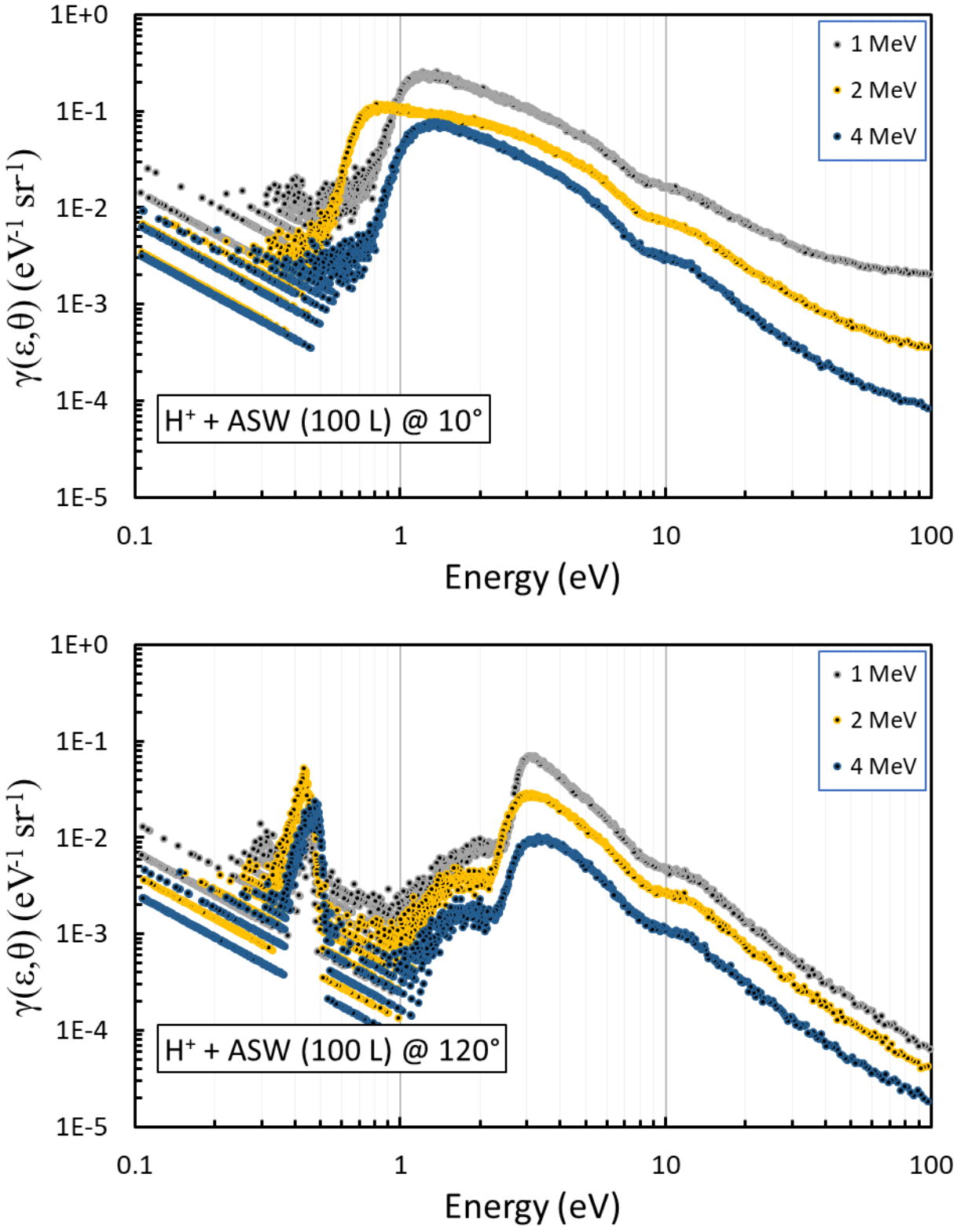

FIG. 4.14. Electron emission spectra from 10° (top) and 120° (bottom) due to proton impact on ASW. Data is shown for 1, 2, and 4 MeV proton energies.

perpendicular to the surface to overcome the surface barrier potential. The angular yields were calculated to determine if this relationship holds true, and to examine the trend of the spatial distribution of electron emission from the surface of a solid.

Fig. 4.15 shows the angular yields of proton-induced electron emission from Au for 1, 2, and 4 MeV beams. The upper graph shows the angular yield from all angles measured in the forward direction, i.e. 10-65°. They are plotted on a cos(θ) scale and fitted with least-squares-fit regression lines. Protons are readily scattered at small angles and are assumed to be present in the electron emission spectra. With the experimental setup used, there is no way to shield the TOF detector from the projectiles. This is possible in other setups employing energy analyzers where the electrostatic deflection of charged particles discriminates positive ions from negatively charged electrons. Therefore, as can be seen in the upper graph, the cosine relationship is not followed at small angles. This is particularly true for 1 MeV proton-induced yields, as expected due to the higher probability of projectile scattering at this energy. The linear trend is more closely followed at 2 MeV and even more so at 4 MeV, as expected.

This trend was used as justification for establishing a linear regression at limited angles, from 30-65° and 120-160°. When these angular yields are plotted as a function of cos(θ) as shown in the lower graph of Fig. 4.15, the linear regression all have an R^2 coefficient of determination ≥0.994. This includes the assumption that the electron yield at 90° is zero, which was confirmed in background spectra taken at this angle. The slope of the linear regression was used for the integration of angular yields to determine the total yields in both the forward and backward directions. The error bars shown in Fig. 4.15 reflect the combined uncertainty of the normalization process, the main component of which is the assumption of linearity.

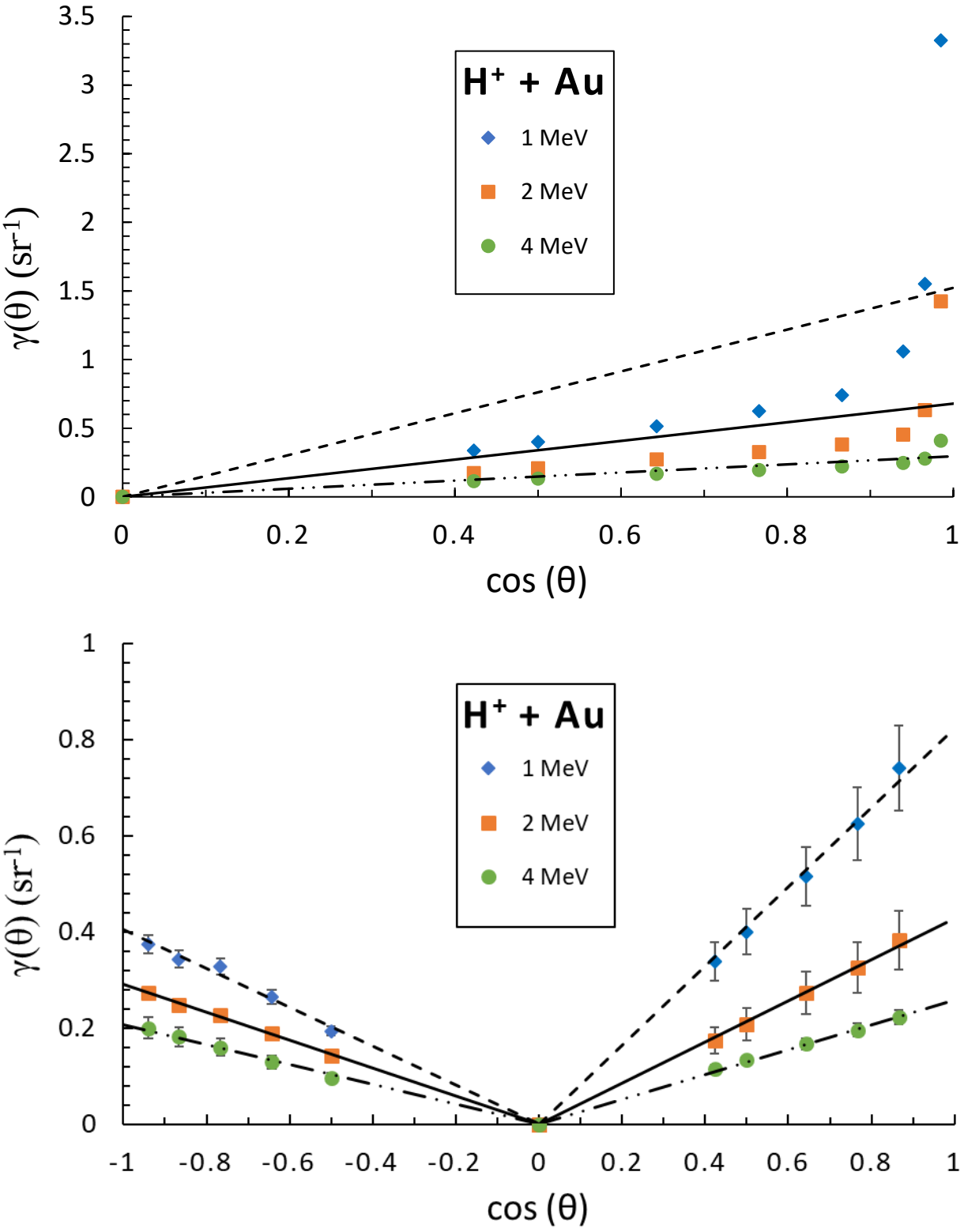

FIG. 4.15. The angular yields from 1, 2, and 4 MeV impact on Au are shown as a function of the cosine of all forward emission angles 10-65° (top) and angles between 30-160°, excluding 115° (bottom). Also shown are linear regressions for each proton energy.

The values for total yields are shown in Table 4.1. Here, the published values for total backward yield γ_B are from Benka *et al.* [8] and Koyama *et al.* [51], which were used in the normalization process. Total forward yield γ_F and total yield γ were dependent on the measured doubly differential electron emission yields presented in the previous sections. Electronic stopping power S_e values are from Ziegler *et al.* [114], and were used in equation 2.18 to determine the material parameter Λ of Au. This published value of material parameter from Rothard *et al.* [79] is 0.033 nm/eV. The material parameter given by 1 MeV protons agrees with this value, but the 2 and 4 MeV proton data produced values 24% lower. This cannot be attributed to the use of two independent sources for total backward yields required for the normalization process, as the total backward yields from 1 and 2 MeV protons on Au were from the same author and produced different values for material parameter.

Table 4.1. Total backward yields [8, 51], total forward yields, and total yields of secondary electron emission from Au at 1, 2, and 4 MeV proton impact. Material parameter is also shown, calculated from stopping power values [114] using equation 2.18.

Energy (MeV)	γ_B	γ_F	γ	S_e (eV/nm)	Λ (nm/eV)
4	0.65 ± 0.03	0.81 ± 0.04	1.46 ± 0.07	61.2	0.024
2	0.91 ± 0.03	1.34 ± 0.04	2.25 ± 0.07	89.1	0.025
1	1.27 ± 0.04	2.86 ± 0.09	4.13 ± 0.12	124	0.033

4.3.5: Comparison to Simulation

Figs. 4.16 and 4.17 show the electron emission spectra from 2 MeV proton impact on ASW along with the simulated electron emission spectra from MC track-structure code. Both experimental and simulated doubly differential yields were normalized, such that the value of yield represents ejected electrons per incident proton. The simulation included 220,000 proton

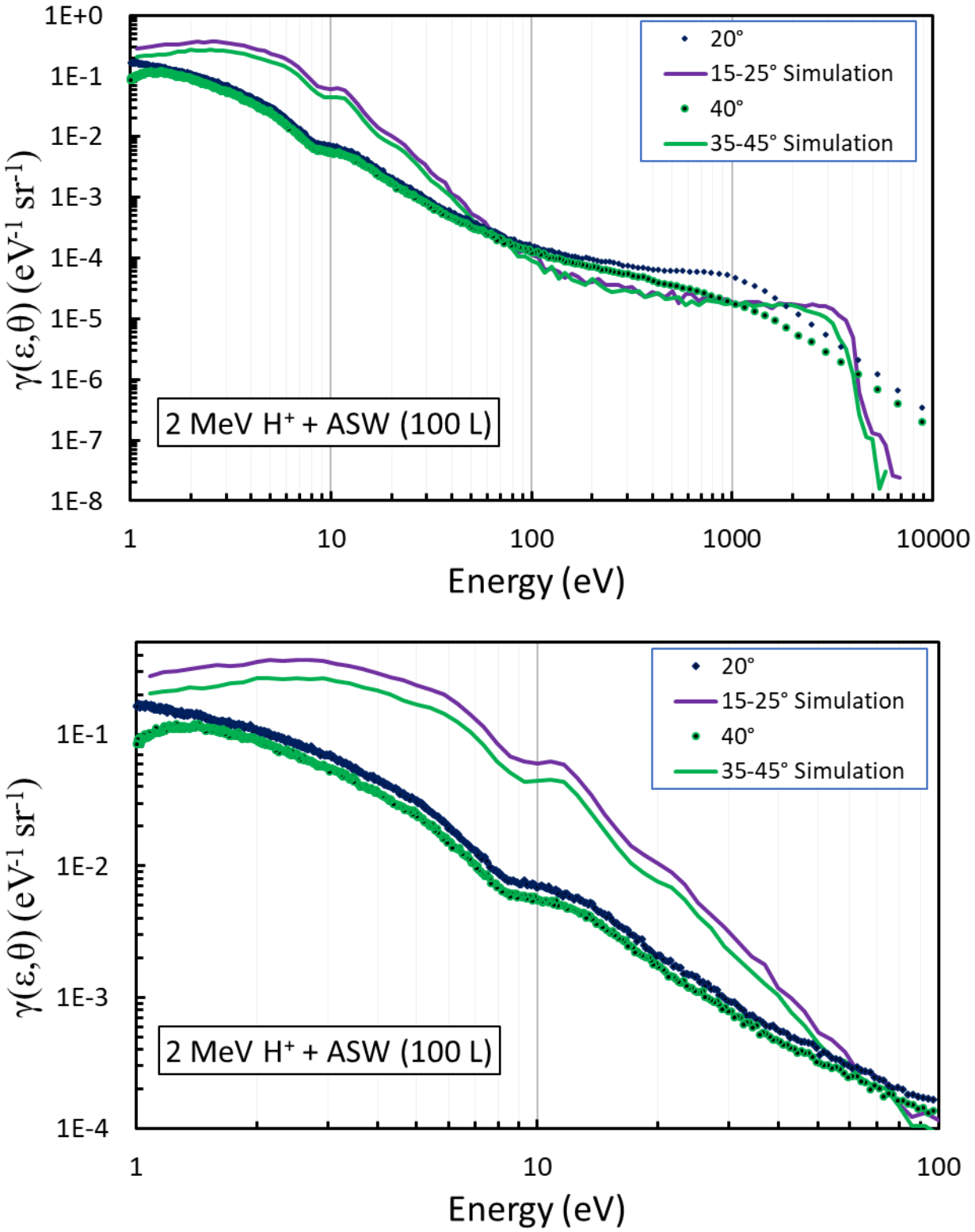

FIG. 4.16. Forward electron emission spectra from 2 MeV impact on 100 L of ASW from experiment and simulation. Both graphs depict the same data, but over different ranges of electron energy. The MC simulation employs water for the full thickness of the target [22].

projectiles and, using the PARTRAC code package, required ~2 weeks of computational time in the laboratory of M. Dingfelder [22]. The geometry of the simulation was comprised of 20 nm films of water on both entrance and exit sides of a 1 μm substrate of water, which was density scaled to mimic copper. Even though the experimental setup used Au foil as a substrate, the production, transport, and escape of electrons that were detected occurred within the ASW, because the thickness exceeded the range of secondary electrons. Therefore, the substrate material used in the simulation would only affect the transport of projectiles, predominately in the elastic scattering from the target media.

The spectra shown in Fig. 4.16 are from 20° and 40° electron emission angles as measured by the TOF detector, with the simulation accounting for electrons emitted over a range of angles, i.e. 15-25° and 35-45°. The upper graph shows the full energy range of the simulated electron yield, and the lower graph is shown with truncated axes. It can be seen that the autoionization peak of water is located at the same energy in both experiment and simulation, however the peak is much narrower in the simulation. The corresponding spectra follow the same general pattern of a low-energy electron peak, followed by a dip prior to the autoionization peak, then the peak itself, and finally a slow decrease leading up to a marked decline in the 1000-4000 eV range. While only 2 angles are shown, all forward emitted electron spectra in experiment and simulation differed by the same amount at any given energy. The experimental yield is approximately 50-85% lower than simulated yield from 1-70 eV for a given angle. Then, all angles showed matching yield at roughly ~70 eV followed by additional discrepancies on the order of one magnitude at higher energies.

The spectra shown in Fig. 4.17 for backward emitted electrons have the same similarities and differences between experimental and simulated results, except for a larger discrepancy in

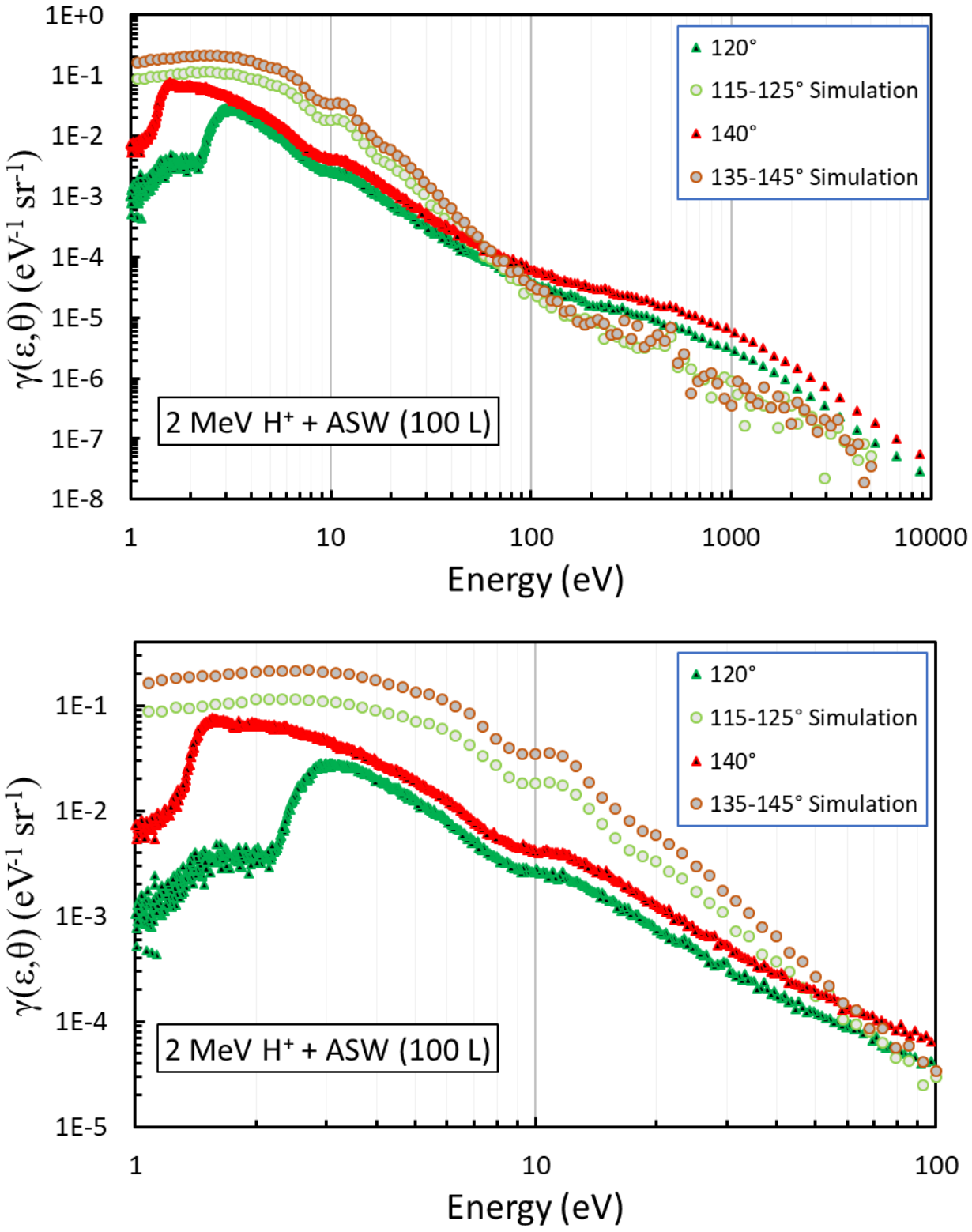

FIG. 4.17. Backward electron emission spectra from 2 MeV impact on 100 L of ASW from experiment and simulation. Both graphs depict the same data, but over different ranges of electron energy. The MC simulation employs water for the full thickness of the target [22].

the 1-3 eV range. The simulated yields are higher in the 1-70 eV range, where both sets of data display an autoionization peak at approximately 10-14 eV. Above 70 eV, the simulated yields are lower than the experimental yields, but follow a very similar slope.

4.4: C-Ion-Induced Electron Emission Spectra

The electron emission spectra from C-ion impact are shown in the following subsections. These spectra were not normalized to published yields of the same charge state, because such data was not available for Au targets. The electron emission spectra were normalized by numerical integration of doubly differential yields over electron energy and integration under a linear fit of angular yields to $\cos(\theta)$, as discussed in the previous section. For 6 MeV C^{2+} and C^{3+}, the total backward yield was normalized with published data by Benka *et al.* [8] for fully stripped C^{6+} projectiles. The total backward yields for these C ions on Au increases by only 1.3 % over an energy range of 4.8-8.0 MeV, according to the author, and an interpolated value was calculated for 6.0 MeV. However, the interaction cross sections for fully stripped ions are not expected to be the same as for dressed ions, as charge screening effects will reduce the stopping power of dressed ions in a material. Therefore, values reported for doubly differential electron yields in the following sections will be denoted as $\gamma^*(\varepsilon, \theta)$ and considered estimated yields and not absolute yields.

The same holds true for the results due to 2.4 MeV impact on Au and ASW. This energy was of particular interest due to its location in the Bragg peak. A similar charge state and energy was found in the literature, in an article published by Itoh *et al.* [45]. Electron emission spectra were normalized to the value of total backward yield given for 2.0 MeV C^+, from impact at an

angle of 37° from the perpendicular. In an effort to study the effects of projectile charge state on secondary electron emission, 6 MeV C^{3+} was also produced and used as a projectile with Au targets. These data will be compared to spectra from doubly-charged C ions of that energy.

4.4.1: Au Target

The relative secondary electron emission spectra for doubly-charged 2.4 MeV C ions on Au are shown in Fig. 4.18. In the forward electron emission direction shown in the upper graph, the low-energy electron peak slowly shifts higher in energy from approximately 0.9 to 1.9 eV and decreases in height by roughly 21% as the angle increases from 10-65°. The exit energy after traversing the Au foil for a C ion with initial energy of 2.4 MeV is approximately 0.391 MeV. The projectile loses about 84% of its energy due to the high stopping power in this region. The corresponding convoy electron energy is 17.9 eV. Convoy electron peaks can be seen at approximately 14-18 eV for the smaller emission angles. Additionally, in the forward direction there is a peak located in the 120-170 eV range. This may arise from a NNV Auger transition in Au observed at 140 eV as seen by Rothard *et al.* [80]. This peak is not seen in the backward emission angles, however.

Prior to the possible Auger peak is a very pronounced shoulder, occurring between 35 and 40 eV in the forward direction. This shoulder is also present in the backward direction, but does not occur until 50-60 eV. This feature may be projectile energy dependent, as the forward and backward C-ion energies are so different. In the backward direction, the low-energy electron peak increases in energy from approximately 1.0 to 2.4 eV as the emission angle decreases from 160 to 115°. The cutoff location follows the same trend, increasing from roughly 0.8 to 1.4 eV.

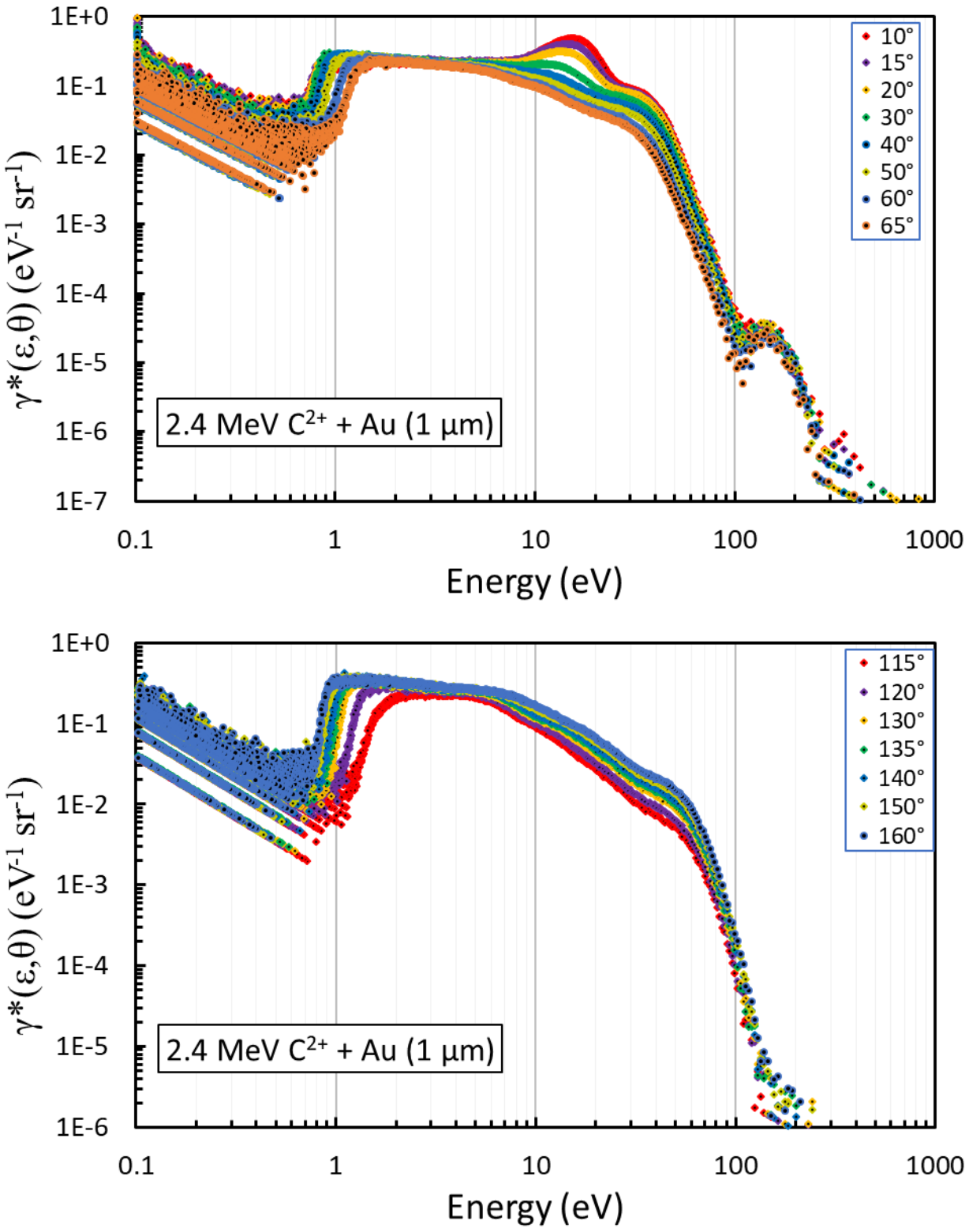

FIG. 4.18. Electron emission spectra from 2.4 MeV C^{2+} impact on Au are shown in the forward direction (upper graph) and backward direction (lower).

The electron emission spectra from doubly-charged 6 MeV C ions on Au are shown in Fig. 4.19. The same trends seen at the lower projectile energy, shift in low-energy electron peak location, cutoff energy, and pronounced shoulder, are once again prevalent in these spectra. The convoy-electron peak is seen in the upper graph of Fig. 4.19 at approximately 120-130 eV. This is exactly where it is expected for a slowed-down C ion of 2.73 MeV. The better agreement seen with C ions vs. protons may suggest that this peak is composed of many more scattered projectiles than convoy electrons, which are more susceptible to multiple scattering and energy loss as they escape from the solid.

The location of the shoulder continues to shift to higher energy with increasing projectile energy. This is a benefit of studying the electron emission from an intermediate energy projectile, where examination and comparison of the forward and backward spectra from projectiles that have lost energy loss in the target reveals projectile dependent features. The shoulder is located at 40, 55, 150, and 200 eV as C ion increases in energy from 0.39 to 6 MeV. The energy correlated to the shoulder appears to be independent of emission angle. This is not fully understood and needs further investigation.

The projectile energy dependence of electron emission spectra from C^{2+} impact on Au is shown in Fig. 4.20. The backward emitted electron spectra, shown in the lower graph, reveal approximately 75% increase in electron yield at 160° for 2.4 MeV (vs. 6 MeV) C ions in the electron energy range <8 eV. This increase in yield depends on emission angle, and as the TOF detector was rotated away from the beam axis the energy dependence on yield became negligible, i.e. it was not observed at 120°. However, for both backward emission angles shown in the lower graph of Fig. 4.20, the low-energy electron cutoff is roughly 0.1 eV lower for

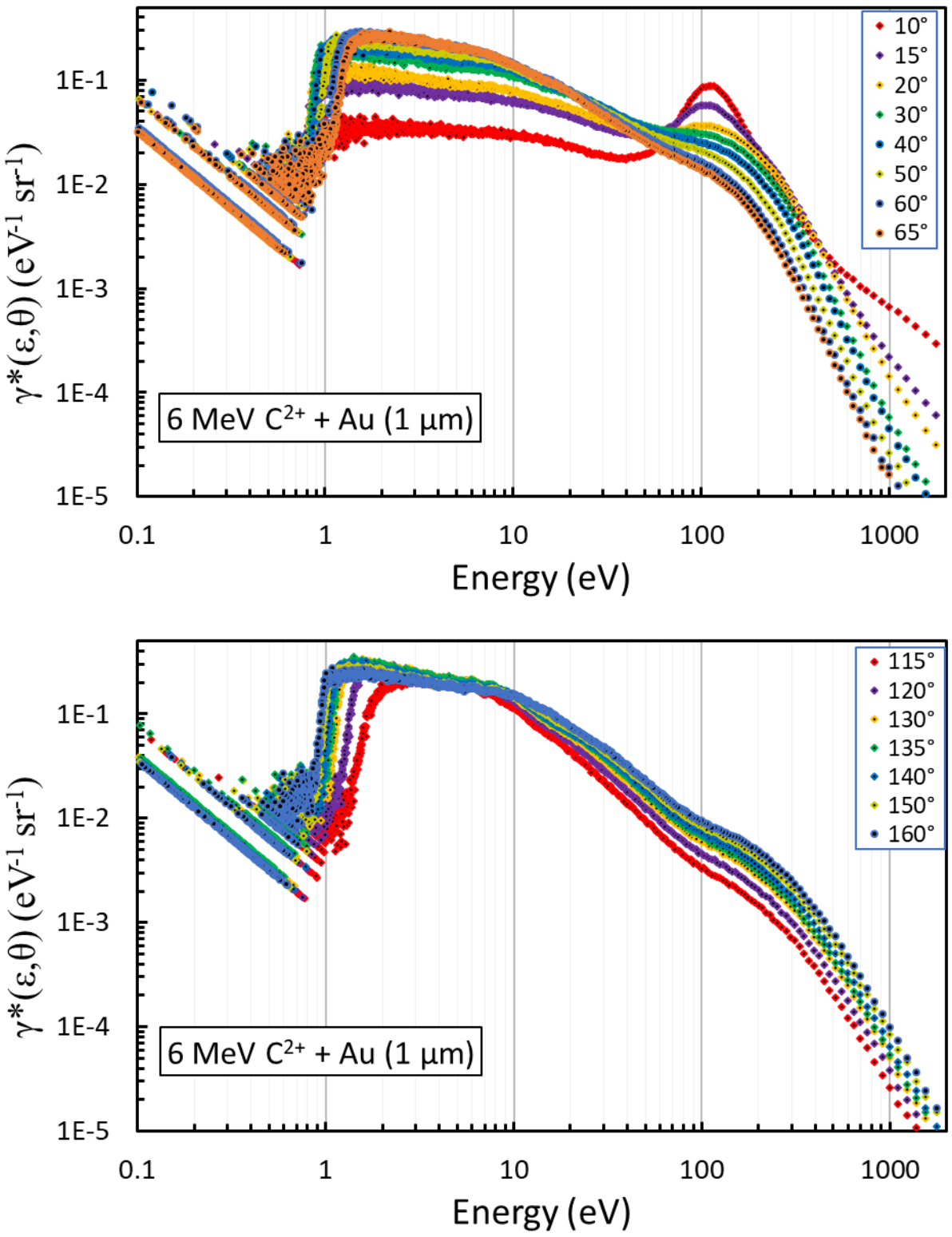

FIG. 4.19. Electron emission spectra from 6 MeV C^{2+} impact on Au are shown in the forward direction (upper graph) and backward direction (lower).

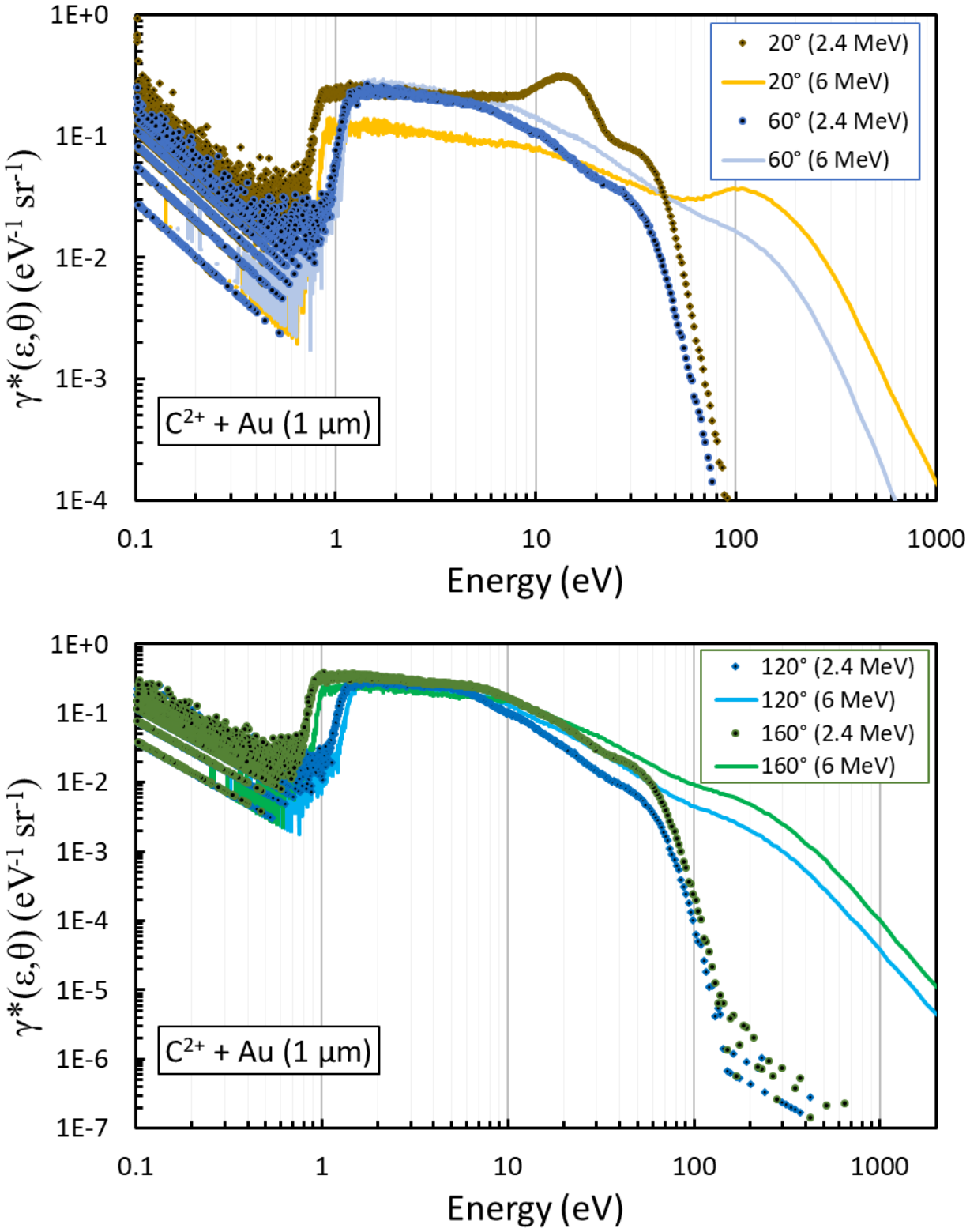

FIG. 4.20. Electron emission spectra at selected angles are shown for both 2.4 and 6 MeV C^{2+} projectiles incident on Au.

2.4 MeV C ions. The yield at higher electron energies show an inverse relationship, because 6 MeV C ions are more likely to produce faster electrons than 2.4 MeV C ions.

The forward emitted electron spectra for both C-ion energies, shown in the upper graph of Fig. 4.20, demonstrates the same features as seen in the backward emission angles. The low-energy electron yield is approximately 100% higher with 2.4 MeV C ions for angles near the beam axis (20°) and becomes equivalent for both C-ion energies as the angle approaches the perpendicular. The low-energy cutoff value is lower for 2.4 MeV C ions. The forward emitted electron spectra are produced by the slowed-down projectiles that have lost energy in traversing the Au foil. Because of this, conclusions on the projectile energy dependence of electron emission are not as firm, as energy straggling has occurred.

The charge-state dependence on secondary electron emission from Au can be seen in Fig. 4.21. Emission angles were selected to highlight the differences and similarities between the electron spectra of C^{2+} and C^{3+} projectiles with 6 MeV energy incident on Au. The low-energy cutoff does not change significantly, as expected. The location of the low-energy peak increases by 0.1 eV for most angles, but at 115° the shift is closer to 1.5 eV. Also, the height of the low-energy electron peak is increased by approximately 38-82% for C^{3+} at varying emission angles, except at 115° where the height is virtually unaffected. As with proton-induced electron spectra, the odd behavior at 115° emission angle may be attributed to the target holder assembly. The count rate in the TOF detector decreases rapidly as it is rotated beyond 115° and closer to 90°. For the most part, the electron emission spectra for both C^{2+} and C^{3+} mirror each other over all energies, with the higher-charged C^{3+} inducing slightly higher electron yields.

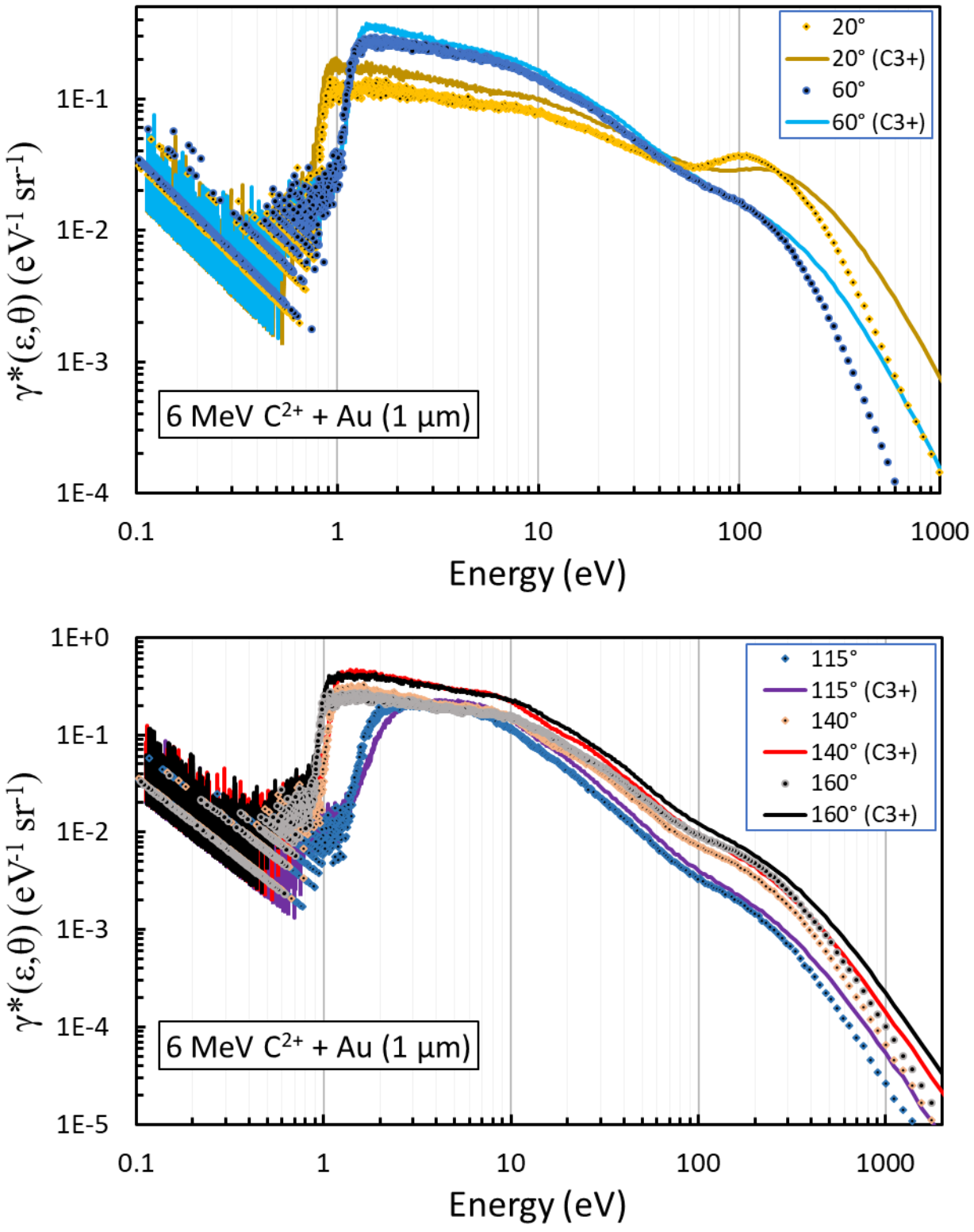

FIG. 4.21. Electron emission spectra at selected angles are shown for both C^{2+} and C^{3+} projectiles with 6 MeV energy, incident on Au.

4.4.2: ASW Target

For C-ion impact on ASW, the exposure of the Au foil to the DI water by the background dosing technique was again used. In this process, the study of buildup of ASW was repeated to determine if the choice of 100 L film thickness (~100 ML) was still valid. The results of this buildup test gave the same outcome as seen before with proton-induced electron emission from ASW, and it was determined that this thickness was ideal. At 100 L, the ASW film is thick enough to exceed the range of secondary electrons, but still thin enough to limit the effects of target charging.

The C-ion-induced secondary electron emission spectra from ASW are shown in Fig. 4.22 for 2.4 MeV C-ion impact and in Fig. 4.23 for 6 MeV C-ion impact. These spectra show the same features as observed by proton-induced electron emission from ASW, with the addition of the ~130 eV peak in the forward direction for 2.4 MeV C^{2+}. Due to the presence of this peak with the ASW target, the conclusion that it may be attributed to an Auger transition in Au may no longer be valid. Instead, it might be attributed to a C-ion projectile Auger transition. The early peak is once again present at approximately 0.4 eV for 6 MeV C ions, although it appears slightly shifted to 0.3 eV for 2.4 MeV C ions. Additionally, for 6 MeV C ions, the peak is even more dominant, matching the height of the 1-2 eV low-energy electron peak for some angles. The projectile energy dependence of electron emission spectra from ASW targets show similar trends as seen with Au targets.

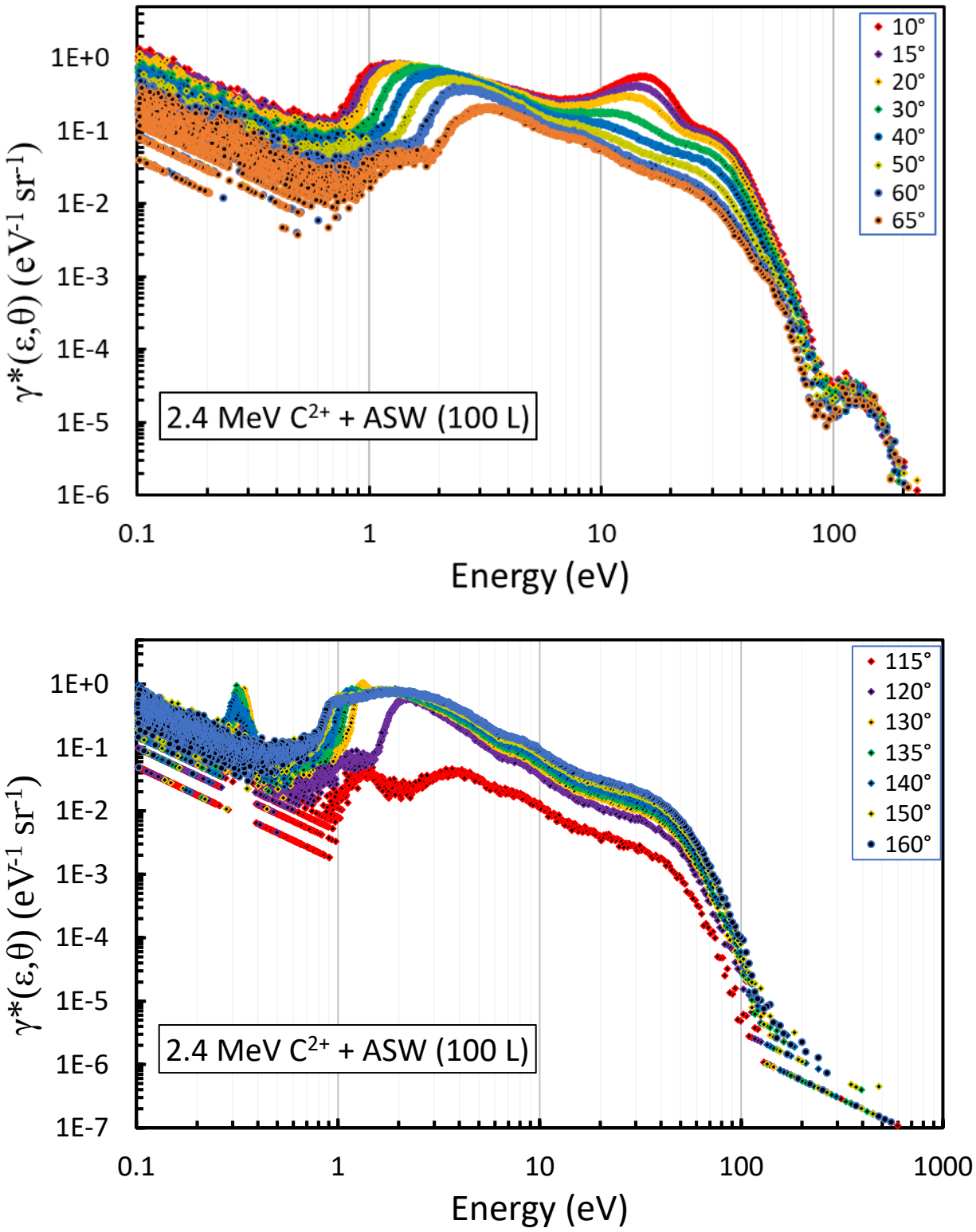

FIG. 4.22. Electron emission spectra from 2.4 MeV C^{2+} impact on 100 L of ASW are shown in the forward direction (upper graph) and backward direction (lower).

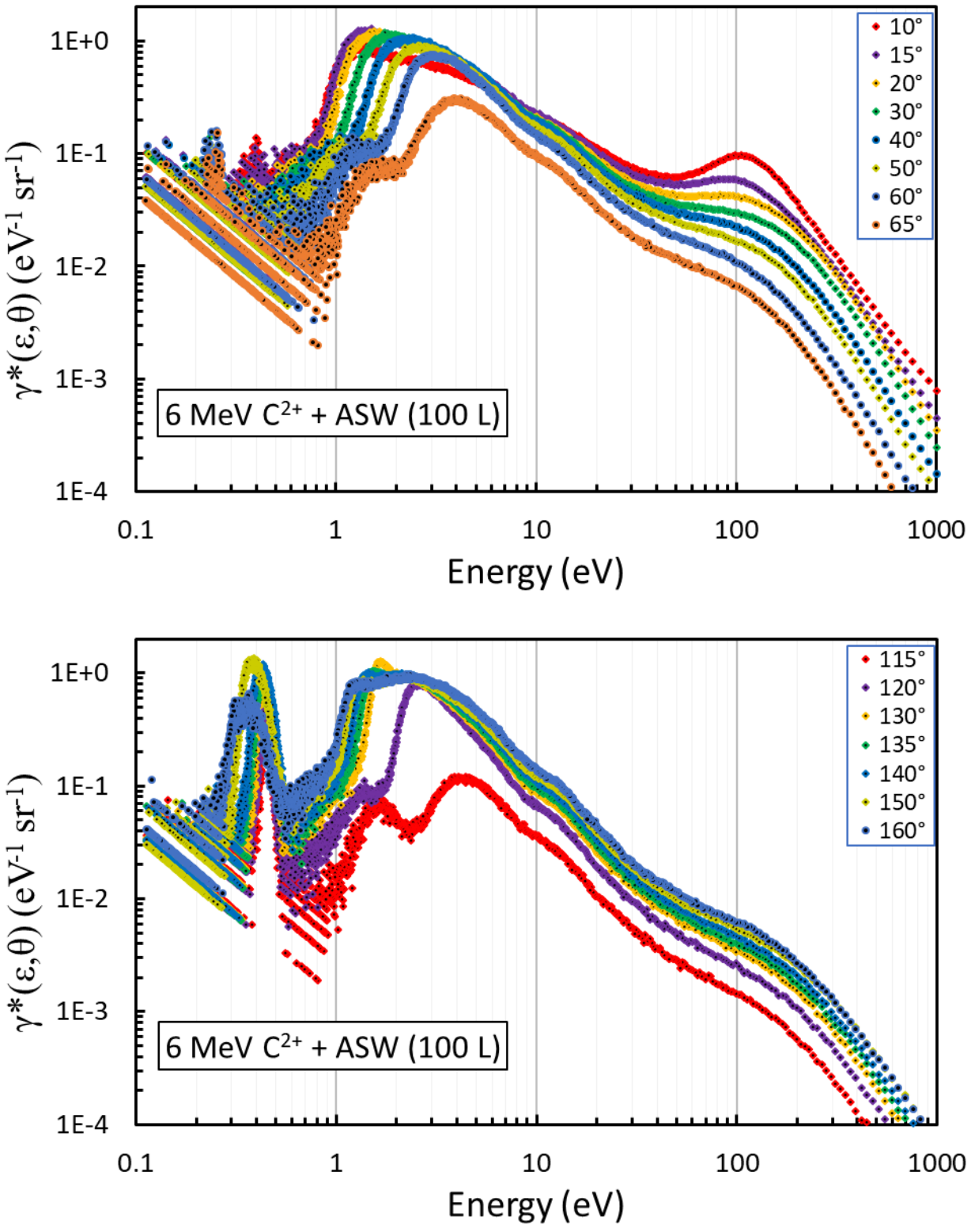

FIG. 4.23. Electron emission spectra from 6 MeV C^{2+} impact on 100 L of ASW are shown in the forward direction (upper graph) and backward direction (lower).

Chapter 5: Conclusions and Future Direction

The doubly differential electron emission spectra from proton and C-ion projectiles of various energies ranging from 0.2-4 MeV/u on Au and ASW targets were measured and compared to MC simulation electron yields. These measurements utilized the TOF energy analysis technique to focus on the low-energy ($\varepsilon<50$ eV) portion of the electron emission spectra, for emission angles θ between 10-160° relative to the projectile velocity. These spectra were analyzed to determine angular dependence, projectile energy dependence, and C-ion charge-state dependence of secondary electron emission from solid targets. The measurements performed were found to show dependencies of secondary electron emission consistent with comparable studies reported in the literature. The secondary electron yields can serve as a database for further MC simulations, to determine inconsistencies in the low-energy region of electron emission from solids. This will allow modification of ionization cross sections in the low-energy region, where assumptions and extrapolations are required in the theoretical description of charged-particle interaction with condensed-phase materials.

Considerations need to be taken for electron spectra at certain emission angles. For all projectile and target combinations, the doubly differential electron emission yields were measured from thin targets, allowing electron emission from both sides of the target to be studied, i.e. angles θ between 10-65° in the forward direction and 115-160° in the backward direction. Emission angles approaching 90° in both directions were limited by the experimental target holder assembly, and as such, 115° electron emission spectra were found to be inconsistent. This suggested that special consideration should be given to these measurements when interpreting angular dependence of secondary electron emission. Likewise, for small

forward angles, particularly ≤20°, the electron emission spectra require special consideration when drawing conclusions of angular or energy dependencies on electron yield. This is due to the unavoidable inclusion of scattered projectile counts in the TOF detector at these small angles, which can influence the shape of the electron spectra, especially for more readily-scattered slower projectiles.

Possible improvements to the experiment, regarding the angular limits just described, might entail a redesign of the target holder assembly. By narrowing the thickness of the copper target holder, a wider range of angles approaching 90° could be investigated. This may require extending the diameter of the opening and a larger segment of Au foil, for instance. A downside to this would be a further limitation on foil thickness, however, which would be disadvantageous for employing a thinner Au foil to accommodate lower energy projectiles without exceeding the range of these projectile ions. With a thinner target foil, less projectile scattering and energy loss would occur, allowing better comparisons between forward and backward emission of secondary electrons to be made.

Considerations also need to be taken for the extreme low and high energy ranges of secondary electron emission. Due to the nature of TOF electron energy analysis, as little as 2-5 ns uncertainty in the timing can produce an uncertainty in energy of 26-78% at 100 eV. Additionally, the presence of even subtle stray electric and magnetic fields in the vicinity of the target can alter the detection efficiency of very low-energy electrons. Surface contamination was also shown to greatly influence low-energy electron emission, leading to the conclusion that electron energies below approximately 1 eV could be affected. Therefore, the electron energy range in the TOF measurement technique where firm conclusions can be drawn is approximately 1-50 eV.

Possible improvements to extend the energy range of electrons include two additional Helmholtz coils and an electrostatic analyzer. The current configuration of Helmholtz coils was chosen to cancel the largest component of Earth's magnetic field, the vertical component. However, although the residual magnetic field at the target location in the UHV chamber was <1 μT, the horizontal components could be minimized even further to more closely establish a true field-free interaction region. This would extend the trusted energy range of electron detection below 1 eV. On the high-energy side, a UHV electrostatic analyzer has been recently calibrated and is ready to be incorporated into the target chamber. With the addition of this analyzer, the trusted energy range of electron detection can be extended to provide better resolution of high-energy electron emission structure, i.e. Auger peaks, convoy electron peaks, and BE peaks.

For proton impact on Au, the overall dependencies of secondary electron emission on electron energy and emission angle, as well as projectile energy, were as expected. In either backward or forward direction, the yield of electrons at all energies decreased as the emission angle approached 90°. This is due to the pathlength and energy loss of the secondary electrons with various trajectories as the travelled to the surface of the solid before being emitted. Likewise, the low-energy cutoff increased in electron energy as the emission angle approached 90°, due to the probability of escape and the escape cone for a given energy of electrons. The yield of electrons rapidly decreased for higher electron energies, as the likelihood of electrons being produced, i.e. the ionization cross section, is known to decrease for higher energy electrons. This trend is skewed by the energy loss of electrons during transport to the surface of the solid. The approximate decrease in electron yield from 1-1000 eV was 99.9%, or 3 orders of magnitude. The dependence of electron emission yields on proton energy also followed an expected trend. As proton energy was increased from 1-4 MeV, the yield of secondary electrons

decreased, over all energies and emission angles. This is due to the decreasing stopping power S of protons in Au, dropping by approximately 52% over this projectile energy range. The corresponding material parameter Λ for Au was calculated from the total electron yield and the stopping power to be between 0.024-0.033 nm/eV, a range that encompasses published values.

The trends seen in electron emission from Au by proton impact were also seen in ASW. This included angular dependence of low-energy yield and cutoff, as well as projectile energy dependence of yield. However, the overall shape of the electron emission spectra was significantly different for this target material. The low-energy electron peak was more pronounced, an order of magnitude higher than with Au. Additionally, an autoionization peak at approximately 13 eV was observed, in agreement with published values. Interestingly, there was evidence of an electron peak prior to the 1-3 eV low-energy peak, occurring at roughly 0.4 eV. This was not consistently observed, however, and might be attributed to charge buildup in the ASW film affecting some of the low-energy electrons' trajectory. This early peak was seen at all proton energies, mostly in backward angles approaching 90°. Further investigation is needed to confirm the validity of this electron peak.

Comparison of electron emission spectra from 2 MeV proton impact on ASW to MC simulated electron yields revealed fairly good agreement from approximately 50-5000 eV at all emission angles. The agreement was well within the energy uncertainty of the measured yields at these higher energies. Below 50 eV, where the measured electron yields are considered to be most accurate, the simulated yields were higher by up to an order of magnitude, particularly in the ~10 eV region. The location of the autoionization peak was nearly identical for both experimental and simulated electron yield spectra.

C ion impact on both Au and ASW generated electron emission spectra that followed the expected trends as seen with proton impact. Overall, the shape of the C-ion induced electron emission spectra showed a much wider low-energy electron peak than with proton projectiles. The low-energy portion of the spectra was fairly flat, more of a plateau than a peak, sometimes extending from approximately 1-50 eV before dropping one order of magnitude in yield. The decrease in yield at higher energies, however, was dramatic. For 2.4 MeV C ions, the high-energy drop-off in yield was roughly 4 orders of magnitude over the energy range 50-200 eV. For 6 MeV C ions, this drop-off was slower, with a decrease in yield from approximately 200-1000 eV encompassing 2-3 orders of magnitude. The charge-state dependence of 6 MeV C ions on electron emission yield was as expected, with an increase observed for C^{3+} at every angle.

Further investigation of the charge-state dependence of electron emission yields should be investigated. With the current accelerator configuration employing a gas stripper at the terminal, C^{+} and C^{4+} projectiles are possible. However, a maximum energy of 4 MeV would be attainable for C^{+}, so a lower energy would need to be used for a full comparison across all charge states. This would entail a large projectile energy loss for forward emitted electron yields. However, it would still be informative to explore the electron emission from both sides of Au and ASW targets.

A direct comparison of proton and C-ion induced electron emission from AU and ASW was not made. The general differences in the electron emission spectra were observed, but not for projectiles of matching velocities. It is not expected that the overall structure of the proton-induced electron spectra would change significantly at lower proton energies, but future studies could attempt to achieve 0.5 MeV protons to match the velocity of the 6 MeV C ions used in this research. Also, projectile ions other than protons and C ions could be studied in an attempt to

achieve a comprehensive database of electron emission from Au and ASW induced by fast charged particles.

For the determination of ASW film thickness, a quartz crystal microbalance should be installed in the UHV chamber. This device could be used to calibrate the exposure of the Au-foil substrate and directly relate the measurement in Langmuir to the mass and thickness of the ASW thin film. This would be useful not only for future research, but also to the work presented here, where the 100 L exposure of ASW could be retroactively converted to monolayers.

As the UHV target chamber is constantly upgraded and improved, more accurate measurements of secondary electron emission from condensed-phase biological targets can be made. The extended energy range and angular range, increased accuracy of film deposition thickness measurements, enhanced timing resolution, and further reduction of magnetic fields could all lead to more accurate results and better comparisons to MC simulated yields. As the experimental system is improved, a future direction for secondary electron emission research might involve studies of targets composed of DNA nucleobases and animal tissue. This, with the continued expansion of projectile species and energy, could produce a vast database to further the understanding of charged-particle interactions with matter.

REFERENCES

1. Alloni, D., A. Campa, W. Friedland, L. Mariotti, and A. Ottolenghi, *Track structure, radiation quality and initial radiobiological events: Considerations based on the PARTRAC code experience.* International Journal of Radiation Biology, 2012. **88**(1-2): p. 77-86.

2. Alvarado, F., S. Bari, R. Hoekstra, and T. Schlatholter, *Interactions of neutral and singly charged keV atomic particles with gas-phase adenine molecules.* Journal of Chemical Physics, 2007. **127**(3): p. 34301-34301.

3. Ashley, J.C., *Interaction of low-energy electrons with condensed matter: stopping powers and inelastic mean free paths from optical data.* Journal of Electron Spectroscopy and Related Phenomena, 1988. **46**(1): p. 199-214.

4. Baragiola, R., M. Shi, R. Vidal, and C. Dukes, *Fast proton-induced electron emission from rare-gas solids and electrostatic charging effects.* Physical Review B - Condensed Matter and Materials Physics, 1998. **58**(19): p. 13212-13218.

5. Baragiola, R.A., E.V. Alonso, J. Ferron, and A. Oliva-Florio, *Ion-induced electron emission from clean metals.* Surface Science, 1979. **90**(2): p. 240-255.

6. Baragiola, R.A., E.V. Alonso, and A. Florio, *Electron emission from clean metal surfaces induced by low-energy light ions.* Physical Review B, 1979. **19**(1): p. 121-129.

7. Benka, O., E. Steinbauer, and P. Bauer, *Kinetic electron emission yield induced by H+ and He2+ ions versus stopping power for Al, Cu, Ag and Au.* Nuclear Instruments and Methods in Physics Research Section B: Beam Interactions with Materials and Atoms, 1994. **90**(1-4): p. 64-66.

8. Benka, O., A. Schinner, T. Fink, and M. Pfaffenlehner, *Electron-emission yield of Al, Cu, and Au for the impact of swift bare light ions.* Physical Review A, 1995. **52**(5): p. 3959.

9. Benka, O., M. Pfaffenlehner, and A. Schinner, *Electron emission yield of Al, Cu and Au targets induced by fast hydrogen and helium ions.* Nuclear Instruments and Methods in Physics Research Section B: Beam Interactions with Materials and Atoms, 1996. **117**(4): p. 350-356.

10. Benka, O., J. Pürstinger, and A. Koyama, *Kinetic electron emission from Al, Cu, and Au surfaces exposed to oxygen.* Physical Review A - Atomic, Molecular, and Optical Physics, 1998. **58**(4): p. 2978-2984.

11. Brown, D.E., S.M. George, C. Huang, E.K.L. Wong, K.B. Rider, R.S. Smith, and B.D. Kay, *H2O condensation coefficient and refractive index for vapor-deposited ice from*

molecular beam and optical interference measurements. Journal of Physical Chemistry, 1996. **100**(12): p. 4988-4995.

12. Champion, C., A. L'Hoir, M.F. Politis, A. Chetioui, B. Fayard, and A. Touati, *Monte-Carlo simulation of ion track structure in water: ionization clusters and biological effectiveness.* Nuclear Instruments and Methods in Physics Research Section B: Beam Interactions with Materials and Atoms, 1998. **146**(1-4): p. 533-540.

13. Champion, C., *Multiple ionization of water by heavy ions: a Monte Carlo approach.* Nuclear Instruments and Methods in Physics Research Section B: Beam Interactions with Materials and Atoms, 2003. **205**: p. 671-676.

14. Charlton, D.E., H. Nikjoo, and J.L. Humm, *Calculation of initial yields of single- and double-strand breaks in cell nuclei from electrons, protons and alpha particles.* International Journal of Radiation Biology, 1989. **56**(1): p. 1-19.

15. Christou, C.I., *Electron Emission from Condensed Phase Targets by 2 MeV Proton Impact*, 2004, East Carolina University: Greenville, NC.

16. Clouvas, A., C. Potiriadis, H. Rothard, D. Hofmann, R. Wünsch, K.O. Groeneveld, A. Katsanos, and A.C. Xenoulis, *Role of projectile electrons in secondary electron emission from solid surfaces under fast-ion bombardment.* Physical Review B, 1997. **55**(18): p. 12086.

17. Cobut, V., Y. Frongillo, J.P. Patau, T. Goulet, M.J. Fraser, and J.P. Jay-Gerin, *Monte Carlo simulation of fast electron and proton tracks in liquid water-I. Physical and physicochemical aspects.* Radiation Physics and Chemistry, 1998. **51**(3): p. 229-244.

18. Da Silveira, E.F. and J.M.F. Jeronymo, *Secondary electron emission from the entrance and exit surfaces of thin aluminium foils under fast light ion bombardment.* Nuclear Instruments and Methods in Physics Research Section B: Beam Interactions with Materials and Atoms, 1987. **24**: p. 534-537.

19. Dingfelder, M., D. Hantke, M. Inokuti, and H.G. Paretzke, *Electron inelastic-scattering cross sections in liquid water.* Radiation Physics and Chemistry, 1999. **53**(1): p. 1-18.

20. Dingfelder, M., A. Travia, R.A. McLawhorn, J.L. Shinpaugh, and L.H. Toburen, *Electron emission from foils and biological materials after proton impact.* Radiation Physics and Chemistry, 2008. **77**(10-12): p. 1213-1217.

21. Dingfelder, M. and A. Travia, *Cross Sections for Track Structure Codes: Volume Versus Surface Transport.* Radiation Protection Dosimetry, 2015. **166**(1-4): p. 10-14.

22. Dingfelder, M., *(private communication)*, 2018.

23. Drexler, C.G. and R.D. DuBois, *Energy- and angle-differential yields of electron emission from thin carbon foils after fast proton impact.* Physical Review A - Atomic, Molecular, and Optical Physics, 1996. **53**(3): p. 1630-1637.

24. DuBois, R.D. and C.T. Drexler, *Differential Electron Emission from Solids and Frozen Gases*, in *Proceedings of the 17th Werner Brandt Workshop on the Penetration of Charged particles in Matter*, R. Baragiola, Editor 1997, University of Virginia: Charlottsville, VA. p. 95-104.

25. Durante, M., R. Orecchia, and J.S. Loeffler, *Charged-particle therapy in cancer: clinical uses and future perspectives.* Clinical Oncology, 2017. **14**: p. 483-495.

26. Ebner, D.K. and T. Kamada, *The Emerging Role of Carbon-Ion Radiotherapy.* Frontiers in Oncology, 2016. **6**(JUN).

27. Ferrón, J., E.V. Alonso, R.A. Baragiola, and A. Oliva-Florio, *Ion-electron emission: The effect of oxidation.* Surface Science, 1982. **120**(2): p. 427-434.

28. Ferry, J.A., *Recent developments in electrostatic accelerator technology at NEC.* Nuclear Instruments and Methods in Physics Research Section A: Accelerators, Spectrometers, Detectors and Associated Equipment, 1993. **328**(1-2): p. 28-33.

29. Fraser, G.W., *The electron detection efficiency of microchannel plates.* Nuclear Instruments and Methods in Physics Research, 1983. **206**(3): p. 445-449.

30. Friedland, W., P. Jacob, P. Bernhardt, H.G. Paretzke, and M. Dingfelder, *Simulation of DNA Damage after Proton Irradiation.* Radiation Research, 2003. **159**(3): p. 401-410.

31. Friedland, W., M. Dingfelder, P. Jacob, and H.G. Paretzke, *Calculated DNA double-strand break and fragmentation yields after irradiation with He ions.* Radiation Physics and Chemistry, 2005. **72**(2-3): p. 279-286.

32. Friedland, W., M. Dingfelder, P. Kundrát, and P. Jacob, *Track structures, DNA targets and radiation effects in the biophysical Monte Carlo simulation code PARTRAC.* Mutation Research/Fundamental and Molecular Mechanisms of Mutagenesis, 2011. **711**(1-2): p. 28-40.

33. Friedland, W., E. Schmitt, P. Kundrát, M. Dingfelder, G. Baiocco, S. Barbieri, and A. Ottolenghi, *Comprehensive track-structure based evaluation of DNA damage by light ions from radiotherapy-relevant energies down to stopping.* Scientific Reports, 2017. **7**.

34. Frischkorn, H.J., K.O. Groeneveld, D. Hofmann, P. Koschar, R. Latz, and J. Schader, *Ion induced electron ejection from solids.* Nuclear Instruments and Methods in Physics Research, 1983. **214**(1): p. 123-128.

35. Goodhead, D.T., *The initial physical damage produced by ionizing radiations.* International Journal of Radiation Biology, 1989. **56**(5): p. 623-634.

36. Goodhead, D.T., *Initial events in the cellular effects of ionizing radiations: clustered damage in DNA.* International Journal of Radiation Biology, 1994. **65**(1): p. 7-17.

37. Hamm, R.N., J.E. Turner, R.H. Ritchie, and H.A. Wright, *Calculation of heavy-ion tracks in liquid water.* Radiation Research, 1985. **104**(2s): p. 20-26.

38. Hasselkamp, D., K.G. Lang, A. Scharmann, and N. Stiller, *Ion induced electron emission from metal surfaces.* Nuclear Instruments and Methods, 1981. **180**(2-3): p. 349-356.

39. Hasselkamp, D., S. Hippler, and A. Scharmann, *Ion-induced secondary electron spectra from clean metal surfaces.* Nuclear Instruments and Methods in Physics Research Section B: Beam Interactions with Materials and Atoms, 1986. **18**(1-6): p. 561-565.

40. Hasselkamp, D., *Particle Induced Electron Emission II*1992, Berlin: Springer-Verlag.

41. Hespeels, F., A.C. Heuskin, E. Scifoni, M. Kraemer, and S. Lucas, *Backscattered electron emission after proton impact on carbon and gold films: Experiments and simulations.* Nuclear Instruments & Methods, 2017. **4**: p. 8-17.

42. ICRU, *Stopping Powers and Ranges for Protons and Alpha Particles*, 1993, International Commission on Radiation and Measurements: Bethesda, MD.

43. ICRU, *Secondary Electron Spectra from Charged Particle Interactions*, 1995, International Commission on Radiation and Measurements: Bethesda, MD.

44. Itikawa, Y. and N. Mason, *Cross Sections for Electron Collisions with Water Molecules.* Journal of Physical and Chemical Reference Data, 2005. **34**(1): p. 1-22.

45. Itoh, A., T. Majima, F. Obata, Y. Hamamoto, and A. Yogo, *Secondary electron emission from Au by medium energy atomic and molecular ions.* Nuclear Instruments and Methods in Physics Research, Section B: Beam Interactions with Materials and Atoms, 2002. **193**(1-4): p. 626-631.

46. Khan, F.Z., *The Physics of Radiation THerapy*. 5th ed2014, Philadelphia: Wolters Kluwer.

47. Kimmel, G.A., K.P. Stevenson, Z. Dohnálek, R.S. Smith, and B.D. Kay, *Control of amorphous solid water morphology using molecular beams. I. Experimental results.* Journal of Chemical Physics, 2001. **114**(12): p. 5284-5294.

48. Kimmel, G.A., N.G. Petrik, Z. Dohnálek, and B.D. Kay, *Layer-by-layer growth of thin amorphous solid water films on Pt(111) and Pd(111).* Journal of Chemical Physics, 2006. **125**(4).

49. Kobayashi, K., N. Usami, E. Porcel, S. Lacombe, and C. Le Sech, *Enhancement of radiation effect by heavy elements.* Mutation Research, 2010. **704**(1-3): p. 123-131.

50. Koschar, P., K. Kroneberger, A. Clouvas, M. Burkhard, W. Meckbach, O. Heil, J. Kemmler, H. Rothard, K.O. Groeneveld, R. Schramm, and H.D. Betz, *Secondary-electron yield as a probe of preequilibrium stopping power of heavy ions colliding with solids.* Physical Review A, 1989. **40**(7): p. 3632-3636.

51. Koyama, A., T. Shikata, and H. Sakairi, *Secondary electron emission from al, cu, ag and au metal targets under proton bombardment.* Japanese Journal of Applied Physics, 1981. **20**(1): p. 65-70.

52. Krämer, M. and G. Kraft, *Calculations of heavy-ion track structure.* Radiation and Environmental Biophysics, 1994. **33**(2): p. 91-109.

53. Lacombe, S., *Particle therapy and nanomedicine: state of art and research perspectives.* Cancer Nanotechnology, 2017. **8**(9): p. 1-17.

54. Laster, B.H., W.C. Thomlinson, and R.G. Fairchild, *Photon activation of iododeoxyuridine: Biological efficacy of Auger electrons.* Radiation Research, 1993. **133**(2): p. 219-224.

55. Laverne, J.A. and A. Mozumder, *Penetration of low-energy electrons in water.* Radiation Research, 1983. **96**(2): p. 219-234.

56. Liamsuwan, T. and H. Nikjoo, *Cross sections for bare and dressed carbon ions in water and neon.* Physics in Medicine and Biology, 2013. **58**(3): p. 641-672.

57. Long, K.A., H.G. Paretzke, F. MüllerPlathe, and G.H.F. Diercksen, *Calculation of double differential cross sections for the interaction of electrons with a water molecule, clusters of water molecules, and liquid water.* The Journal of Chemical Physics, 1989. **91**: p. 1569.

58. Masel, R.I., *Principles of Adsorption and Reaction on Solid Surfaces*1996, New York: Wiley.

59. McLawhorn, R.A., *Electron Emission from Condensed Phase Targets Induced by Fast Protons*, in *Department of Physics*2008, East Carolina University: Greenville, NC.

60. Meckback, W., G. Braunstein, and N. Arista, *Secondary-electron emission in the backward and forward directions from thin carbon foils traversed by 25-250 keV proton beams.* Journal of Physics B, 1975. **8**: p. 344-349.

61. Middleton, R., *A versatile high intensity negative ion source.* Nuclear Instruments and Methods in Physics Research, 1983. **214**(2-3): p. 139-150.

62. Middleton, R., *A versatile high intensity negative ion source.* Nuclear Instruments and Methods in Physics Research, 1984. **220**(1): p. 105-106.

63. Middleton, R., *A Negative-Ion Cookbook*, 1989, University of Pennsylvania: Philadelphia.

64. Mohamad, O., S. Yamada, and M. Durante, *Clinical Indications for Carbon Ion Radiotherapy.* Clinical Oncology, 2018. **30**(5): p. 317-329.

65. Mozumder, A. and Y. Hatano, *Charged Particle and Photon Interactions with Matter: Chemical, Physicochemical, and Biological Consequences with Applications*2003: Taylor & Francis.

66. Nikjoo, H. and D.T. Goodhead, *Track structure analysis illustrating the prominent role of low-energy electrons in radiobiological effects of low-LET radiations.* Physics in Medicine and Biology, 1991. **36**: p. 229.

67. Nikjoo, H., P. O'Neill, M. Terrissol, and D.T. Goodhead, *Modelling of radiation-induced DNA damage: the early physical and chemical event.* International Journal of Radiation Biology, 1994. **66**(5): p. 453-457.

68. Nikjoo, H., M. Terrissol, R.N. Hamm, J.E. Turner, S. Uehara, H.G. Paretzke, and D.T. Goodhead, *Comparison of energy deposition in small cylindrical volumes by electrons generated by Monte Carlo track structure codes for gaseous and liquid water.* Radiation Protection Dosimetry, 1994. **52**(1-4): p. 165.

69. Nikjoo, H., S. Uehara, D. Emfietzoglou, and F.A. Cucinotta, *Track-structure codes in radiation research.* Radiation Measurements, 2006. **41**(9-10): p. 1052-1074.

70. Norton, G., *New developments in design and applications for Pelletron accelerators.* Pramana, 2002. **59**(5): p. 745-751.

71. Ogawa, H., S. Amano, K. Ishii, and T. Kaneko, *Forward-backward correlated secondary electron emission depending on the emergence angle of 1 MeV/u light ions.* Nuclear Instruments and Methods in Physics Research, Section B: Beam Interactions with Materials and Atoms, 2015. **354**: p. 96-99.

72. Ohno, T., *Particle radiotherapy with carbon ion beams.* EPMA Journal, 2013. **4**(1): p. 9.

73. Paretzke, H.G., J.E. Turner, R.N. Hamm, H.A. Wright, and R.H. Ritchie, *Calculated yields and fluctuations for electron degradation in liquid water and water vapor.* The Journal of Chemical Physics, 1986. **84**: p. 3182.

74. Paretzke, H.G., J.E. Turner, R.N. Hamm, R.H. Ritchie, and H.A. Wright, *Spatial Distributions of Inelastic Events Produced by Electrons in Gaseous and Liquid Water.* Radiation Research, 1991. **127**(2): p. 121-129.

75. Peukert, D., I. Kempson, M. Douglass, and E. Bezak, *Metallic nanoparticle radiosensitisation of ion radiotherapy: A review.* Physica Medica, 2018. **47**: p. 121-128.

76. Pimblott, S.M., J.A. LaVerne, and A. Mozumder, *Monte Carlo simulation of range and energy deposition by electrons in gaseous and liquid water.* Journal of Physical Chemistry, 1996. **100**(20): p. 8595-8606.

77. Poole, P.H., U. Essmann, F. Sciortino, and H.E. Stanley, *Phase diagram for amorphous solid water.* Physical Review E, 1993. **48**(6): p. 4605.

78. Rosler, M. and W. Brauer, *Particle Induced Electron Emission I*1991, Berlin: Springer-Verlag.

79. Rothard, H., K. Kroneberger, A. Clouvas, E. Veje, P. Lorenzen, N. Keller, J. Kemmler, W. Meckbach, and K.O. Groeneveld, *Secondary-electron yields from thin foils: A possible probe for the electronic stopping power of heavy ions.* Physical Review A, 1990. **41**(5): p. 2521-2535.

80. Rothard, H., K. Kroneberger, M. Schosnig, P. Lorenzen, E. Veje, N. Keller, R. Maier, J. Kemmler, C. Biedermann, A. Albert, O. Heil, and K.O. Groeneveld, *Secondary-electron velocity spectra and angular distributions from ions penetrating thin solids.* Nuclear Inst. and Methods in Physics Research, B, 1990. **48**(1-4): p. 616-620.

81. Rothard, H., G. Lanzanò, B. Gervais, E. De Filippo, M. Caron, and M. Beuve. *Swift heavy ion induced electron emission from solids*. in *Journal of Physics: Conference Series*. 2015.

82. Sato, Y., A. Higashi, and D. Ohsawa, *Projectile charge dependence of electron emission from foils.* Physical Review A, 2000. **61**(5): p. 052901.

83. Schlaff, C.D., A. Krauze, A. Belard, J.J. O'Connell, and K.A. Camphausen, *Bringing the heavy: Carbon ion therapy in the radiobiological and clinical context.* Radiation Oncology, 2014. **9**(1).

84. Schou, J., *Secondary electron emission from solids by electron and proton bombardment.* Scanning Microscopy, 1988. **2**(2): p. 607-632.

85. Scifoni, E., E. Surdutovich, and A.V. Solov'yov, *Spectra of secondary electrons generated in water by energetic ions.* Physical Review E, 2010. **81**(2).

86. Seltzer, S.M., D.T. Bartlett, D.T. Burns, G. Dietze, H.G. Menzel, H.G. Paretzke, and A. Wambersie, *Fundamental Quantities and Units for Ionizing Radiation.* Journal of the ICRU, 2011. **11**(1): p. 1-41.

87. Shinpaugh, J.L., L.H. Toburen, and E.L.B. Justiniano, *Fluorine Auger-electron production in collisions of H^{+} and Li^{2+} with fluorocarbon targets.* Physical Review A, 1999. **60**(6): p. R4213.

88. Shinpaugh, J.L., R.A. McLawhorn, S.L. McLawhorn, K.D. Carnes, M. Dingfelder, A. Travia, and L.H. Toburen, *Electron Emission from Condensed Phase Material Induced by Fast Protons.* Radiation Protection Dosimetry, 2011. **143**(2-4): p. 135-138.

89. Sigmund, P., *Stopping of Heavy Ions: a Theoretical Approach*2004, Berlin: Springer.

90. Stevenson, K.P., G.A. Kimmel, Z. Dohnálek, R.S. Smith, and B.D. Kay, *Controlling the Morphology of Amorphous Solid Water.* Science, 1999. **283**(5407): p. 1505-1507.

91. Surdutovich, E., O.I. Obolensky, E. Scifoni, I. Pshenichnov, I. Mishustin, A.V. Solov'Yov, and W. Greiner, *Ion-induced electron production in tissue-like media and DNA damage mechanisms.* The European Physical Journal D - Atomic, Molecular, Optical and Plasma Physics, 2009. **51**(1): p. 63-71.

92. Suszcynsky, D. and J. Borovsky, *Secondary-electron emission from metals impacted by high-velocity particles: molecular-effect deviations from a single-particle picture.* Nuclear Instruments & Methods B, 1991. **53**(3): p. 255-266.

93. Tabet, J., S. Eden, S. Feil, H. Abdoul-Carime, B. Farizon, M. Farizon, S. Ouaskit, and T.D. Märk, *Absolute total and partial cross sections for ionization of nucleobases by proton impact in the Bragg peak velocity range.* Physical Review A, 2010. **82**(2): p. 022703.

94. Toburen, L.H. and W.E. Wilson, *Time-of-flight measurements of low-energy electron energy distributions from ion-atom collisions.* Review of Scientific Instruments, 1975. **46**(7): p. 851-854.

95. Toburen, L.H., S.L. McLawhorn, R.A. McLawhorn, N.L. Evans, E.L.B. Justiniano, J.L. Shinpaugh, D.R. Schultz, and C.O. Reinhold, *Charge transfer and ionisation by intermediate-energy heavy ions.* Radiation Protection Dosimetry, 2006. **122**(1-4): p. 22-25.

96. Toburen, L.H., S.L. McLawhorn, R.A. McLawhorn, K.D. Carnes, M. Dingfelder, and J.L. Shinpaugh, *Electron Emission from Amorphous Solid Water Induced by Passage of Energetic Protons and Fluorine Ions.* Radiation Research, 2010. **174**(1): p. 107-118.

97. Turner, J.E., H.G. Paretzke, R.N. Hamm, H.A. Wright, and R.H. Ritchie, *Comparative Study of Electron Energy Deposition and Yields in Water in the Liquid and Vapor Phases.* Radiation Research, 1982. **92**(1): p. 47-60.

98. Turner, J.E., J.L. Magee, H.A. Wright, A. Chatterjee, R.N. Hamm, and R.H. Ritchie, *Physical and Chemical Development of Electron Tracks in Liquid Water.* Radiation Research, 1983. **96**(3): p. 437-449.

99. Uehara, S., H. Nikjoo, and D.T. Goodhead, *Cross-sections for water vapour for the Monte Carlo electron track structure code from 10 eV to the MeV region.* Physics in Medicine and Biology, 1993. **38**: p. 1841.

100. Uehara, S., L.H. Toburen, W.E. Wilson, D.T. Goodhead, and H. Nikjoo, *Calculations of electronic stopping cross sections for low-energy protons in water.* Radiation Physics and Chemistry, 2000. **59**(1): p. 1-11.

101. Usami, N., K. Kobayashi, Y. Furusawa, H. Frohlich, L. S., and C. Le Sech, *Irradiation of DNA loaded with platinum containing molecules by fast atomic ions C(6+) and Fe(26+).* International Journal of Radiation Biology, 2009. **83**(9): p. 569-576.

102. Van de Graaff, R.J., *Tandem Electrostatic Accelerators.* Nuclear Instruments & Methods, 1960. **8**.

103. Verkhovtsev, A., E. Surdutovich, and A.V. Solov'yov, *Multiscale approach predictions for biological outcomes in ion-beam cancer therapy.* Scientific Reports, 2016. **6**: p. 27654.

104. Ward, J.F., *Some Biochemical Consequences of the Spatial Distribution of Ionizing Radiation-Produced Free Radicals.* Radiation Research, 1981. **86**(2): p. 185-195.

105. Ward, J.F., *The complexity of DNA damage: relevance to biological consequences.* International Journal of Radiation Biology, 1994. **66**(5): p. 427-432.

106. Ward, J.F., *Radiation Mutagenesis: the Initial DNA Lesions Responsible.* Radiation Research, 1995. **142**(3): p. 362-368.

107. webpage. *Particle Therapy Co-Operative Group*. 5/28/2018]; Available from: https://www.ptcog.ch/.

108. Wilson, C.D., C.A. Dukes, and R.A. Baragiola, *Search for the plasmon in condensed water*. Physical Review B - Condensed Matter and Materials Physics, 2001. **63**(12).

109. Wilson, W.E. and H. Nikjoo, *A Monte Carlo code for positive ion track simulation.* Radiation and Environmental Biophysics, 1999. **38**(2): p. 97-104.

110. Wiza, J.L., *Microchannel plate detectors.* Nuclear Instruments and Methods, 1979. **162**(1-3): p. 587-601.

111. Zeitlin, C., *Physical interactions of charged particles for radiotherapy and space applications.* Health Physics, 2012. **103**(5): p. 540-546.

112. Ziegler, J.F., *Stopping of energetic light ions in elemental matter*. Journal of Applied Physics, 1999. **85**(3): p. 1249-1272.

113. Ziegler, J.F., M.D. Ziegler, and J.P. Biersack, *SRIM - The stopping and range of ions in matter (2010).* Nuclear Instruments and Methods in Physics Research, Section B: Beam Interactions with Materials and Atoms, 2010. **268**(11-12): p. 1818-1823.

114. Ziegler, J.F., M.D. Ziegler, and J.P. Biersack. *SRIM 2013*. 2013; Available from: www.srim.org.